2012

Development Of Thermal Management Schemes For High Heat Flux Applications Using Two-Phase Spray Cooling Techniques

Richard Opoku
North Carolina Agricultural and Technical State University

Recommended Citation

Opoku, Richard, "Development Of Thermal Management Schemes For High Heat Flux Applications Using Two-Phase Spray Cooling Techniques" (2012). *Dissertations*. 17.
https://digital.library.ncat.edu/dissertations/17

DEVELOPMENT OF THERMAL MANAGEMENT SCHEMES FOR HIGH HEAT FLUX APPLICATIONS USING TWO-PHASE SPRAY COOLING TECHNIQUES

by

Richard Opoku

A dissertation submitted to the graduate faculty
in partial fulfillment of the requirements for the degree of
DOCTOR OF PHILOSOPHY

Department: Mechanical Engineering
Major: Mechanical Engineering
Major Professor: Dr. John Kizito

North Carolina A&T State University
Greensboro, North Carolina
2012

ABSTRACT

Opoku, Richard. DEVELOPMENT OF THERMAL MANAGEMENT SCHEMES FOR HIGH HEAT FLUX APPLICATIONS USING TWO-PHASE SPRAY COOLING TECHNIQUES. (**Major Professor: John Kizito**), North Carolina Agricultural and Technical State University.

Energy conversion devices produce large heat loads during operation and therefore efficient thermal management schemes for their optimal operation are needed. The goal of this work is to develop thermal management methods for high heat flux applications using two-phase spray cooling techniques. Specifically, thermal management method is developed to achieve higher heat fluxes in the range of 100-1000 W/cm^2. Based on the knowledge gaps identified in the literature, the specific objectives developed were to determine the effect of the test surface area scalability on critical heat flux (CHF), to determine the effect of surface modification of the test substrate on heat transfer performance, to determine the heat flux regimes in a spray cooling experiment and to determine the effect of liquid film thickness on heat transfer performance in spray cooling applications.

A two-phase spray cooling thermal loop equipped with a high speed video imaging and data acquisition system was used to obtain the experimental data presented in this research work. The experimental result showed that modification of a smooth surface increased the heat transfer performance. A heat flux gain of about 130% and heat transfer coefficient enhancement of 8500 W/m^2-K were achieved with a modified surface over a smooth surface. It was determined that the modification of the surface in the form of wicking grooves increased the fluid wettability and spread on the surface of the test substrate.

A phenomenon was observed at incipience of critical heat flux in spray cooling experiment akin to vapor film formation in nucleate pool boiling. Formation of a single bubble covering the whole heated surface was observed. It was identified that the single bubble covering the surface of the test substrate at critical heat flux decreased the surface-to-fluid wettability due to the vapor core inside the single bubble. In addition, Novec 7000 (1-methoxyheptafluoropropane), a new working fluid, was identified as a prospect for cooling applications. Lower excess temperatures were obtained with Novec 7000 fluid when compared to water.

School of Graduate Studies
North Carolina Agricultural and Technical State University

This is to certify that the Doctoral Dissertation of

Richard Opoku

has met the dissertation requirements of
North Carolina Agricultural and Technical State University

Greensboro, North Carolina
2012

Approved by:

Dr. John Kizito Major Professor	Dr. Mannur Sundaresan Committee Member
Dr. Vinayak Kabadi Committee Member	Dr. Sun Yi Committee Member
Dr. Samuel Owusu-Ofori Department Chairperson	Dr. Sanjiv Sarin Associate Vice Chancellor for Research and Dean of Graduate Studies

DEDICATION

I dedicate this Doctoral Dissertation to my wife, Rita Mensah, for her continual support and prayers that have made this work successful and also to my family for their love and support that held me high during the course of this work.

BIOGRAPHICAL SKETCH

Richard Opoku was born on March 18, 1983, in Kumasi, Ghana. He received a Bachelor of Science degree in Mechanical Engineering from Kwame Nkrumah University of Science and Technology (KNUST), Ghana, in 2007 with First Class Honors. He served as a Teaching Assistant in same university in 2007/2008 academic year.

Richard Opoku is a member of the American Society of Mechanical Engineers (ASME) and American Institute of Aeronautics and Astronautics (AIAA). He is also a member of The Energy Centre, Kwame Nkrumah University of Science and Technology (TEC–KNUST). He has received a number of awards and recognitions including: Dr. Kennedy 4.0 GPA holder (2009, 2010, 2011 and 2012) at NCATSU; Outstanding International Student for 2009/2010 academic year at NCATSU. Richard Opoku is a candidate for the Ph.D. degree in Mechanical Engineering.

ACKNOWLEDGMENT

I am very grateful to Almighty God for His strength, gifts of knowledge and perseverance that have made this Doctoral Dissertation possible. It is also with much appreciation and gratitude that I thank my academic advisor, Dr J. P Kizito, for his insights and directions in making this research successful. I also thank my doctoral committee members: Dr. Kabadi, Dr. Sundaresan and Dr. Sun Yi for their efforts and time toward this dissertation.

I offer my regards and blessings to my colleagues and all those who supported me in any respect towards the completion of this work. This research was funded by the Department of Defense through Wright-Patterson Air Force Research Laboratory Dayton, Ohio via a sub contract from United Technologies Corporation FA8650-08-D2806-Task Order 0004.

TABLE OF CONTENTS

LIST OF FIGURES

FIGURE **PAGE**

LIST OF TABLES

TABLE **PAGE**

LIST OF SYMBOLS

T_s	Substrate surface temperature, [^oC]
T_l	Temperature of fluid (liquid), [^oC]
T_g	Temperature of vapor (gas), [^oC]
u	Velocity in x-direction, [m/s]
v	Velocity in y-direction, [m/s]
w	Velocity in z-direction, [m/s]
F_x	Force in x-direction, [Newton]
F_y	Force in y-direction, [Newton]
F_z	Force in z-direction, [Newton]
P	Pressure, [Pascal]
Lc	Characteristic length scale, [m]
D	Diameter of fluid droplet, [m]
r	Aspect ratio
i	Index of fluid phase during phase change
θ	Angle of inclination, [degrees]
t	Time, [seconds]
V_∞	Upstream velocity, [m/s]
V_n	Velocity of receding fluid during phase change, [m/s]
ñ	Unit vector
ρ	Density, [kg/m^3]
ρ_l	Density of liquid, [kg/m^3]

ρ_v	Density of vapor, [kg/m^3]
ρ_r	Liquid to vapor density ratio
e	Specific internal energy of fluid, [J/kg]
k	Thermal conductivity, [W/m-K]
C_p	Specific heat capacity, [J/kg-K]
μ	Dynamic viscosity, [N-s/m^2]
υ	Kinematic viscosity, [m^2/s]
σ	Surface tension, [N/m]
β	Volumetric thermal expansion coefficient, [K^{-1}]
g	Acceleration due to gravity, [m/s^2]
h_{fg}	Latent heat of vaporization, [J/kg]
$\dot{q}$	Heat flux, [W/m^2]
Q	Heat energy, [J]
CHF	Critical Heat Flux, [W/m^2]
Pr	Prandtl number
Pe	Peclet number
Bo	Bond number
We	Weber number
Nu	Nusselt number
Re	Reynolds number
Fr	Froude number
Ja	Jacob number

PFV	Photron FastCam Viewer
f	Subscript for (fluid) liquid phase
vap	Subscript for vapor phase

CHAPTER 1

INTRODUCTION

The overall goal of the present research work is to develop thermal management methods with high heat flux removal capabilities. Specifically, a two-phase spray cooling technique is applied for high heat flux removal applications. High heat loads dissipation equipment such as general energy conversion devices and process plants, advanced on-board flight systems for space exploration, laser systems, and general heat exchange technology produce heat fluxes in excess of 100 W/cm^2. The performance of such systems depends on their thermal constraints, among other conditions and factors. Traditional cooling techniques (natural or forced convection and pool boiling heat transfer) are insufficient for removal of such high heat fluxes especially for large surface areas. Therefore, there is an urgent need for the development of efficient thermal management techniques for the deployment of high heat flux removal capacity.

Investigations by other researchers have shown that spray cooling can efficiently be used as a thermal management scheme for high heat flux applications (Silk, Golliher, & Selvam, 2007; Visaria & Mudawar, 2007). Higher heat removal capabilities of spray cooling over jet impingement, air cooling and pool boiling is additionally coupled with temperature uniformity of the heated surface during the cooling process. The higher heat fluxes obtained with spray cooling is reported in the literature to be associated with the phase change process which occurs during spray cooling.

Successful applications of spray cooling in some thermal loops and in the space shuttle's flash evaporator system (FES) has expedited experimental determination of test conditions and spray characteristics that provide optimum heat flux removal capability as well as heat transfer coefficient enhancement techniques. The complexity of spray cooling process together with the many parameters that control the mechanism has led to the difficulty of developing theoretical and analytical equations to describe the process. Existing equations describing heat flux with spray cooling mechanism have been empirically obtained with specific data from individual researchers. Thus, the application of existing empirical correlations to different experimental data is limited. Most of the empirical correlations have also been fitted from narrow controlling parameters that affect spray cooling heat transfer. Widespread of spray cooling in industrial application is therefore limited due to poor understanding of the underlying mechanisms and the key parameters that influence cooling performance (Kim, 2007; Silk, Golliher, & Selvam, 2008).

Previous research work in spray cooling by other researchers have focused on the effect of: droplet diameter, volumetric flux, nozzle orifice-to-heated surface distance, working fluid conditions, sub-cooling, surface enhancement, single to multi-nozzle arrays and spray inclination on the CHF and heat transfer performance (Bostanci, Rini, Kizito, & Chow, 2009; Panão & Moreira, 2009; Pautsch & Shedd, 2005; Visaria & Mudawar, 2008a, 2008b).

From the literature as will be presented later in Chapter 2, research investigations on liquid film on the heated surface and how it affects CHF and heat transfer performance in spray cooling is insufficient (Silk, et al., 2008; Wang, Liu, Xu, & Chen, 2010). In addition, little is known about the heat transfer regimes in spray cooling experiment. In the present research work, experiments have been developed to ensure thin liquid film evaporation on a heated substrate with two-phase spray cooling technique. Surface enhancement and/or modifications of the test substrate have been deployed to obtain the optimal test surface conditions in maximizing critical heat flux and overall heat transfer coefficient for the thermal management technique. Both water and 3M engineering fluid, Novec 7000, were used as the working fluids in the present research work. The next section presents the specific objectives based on the above information presented.

1.1 Specific Objectives

Upon thorough literature review of spray cooling techniques and based on the knowledge gaps identified, the following specific objectives have been developed:

1. To determine the effect of test surface area scalability on Critical Heat Flux (CHF).

   Test substrates with different surface area sizes would be designed and heat flux experiments would be carried on them. The same test conditions would be maintained for these different surfaces to determine the effect of surface area scalability on critical heat flux during spray cooling experimentation.

2. To determine the effect of surface modifications of test substrate on heat transfer performance.

The surface of the test substrate would be modified in the form of grooves. Unidirectional and multi-directional grooves would be designed on the test surface to determine the effect of surface modifications on heat flux. In addition, tapered grooves at different half-corner angles would be analyzed to determine their wicking phenomenon and their effects on heat flux and the overall heat transfer performance.

3. To determine heat flux regimes in a spray cooling experiment.

A high speed video camera and image processing system would be used to visually observe the fluid-surface interactions upon fluid spray impingement on the heated surface in a spray cooling experiment. Bubble generation, departure and rupture would also be observed using the high speed video camera. In addition, the surface temperature of the substrate would be monitored with K-type thermocouples and data acquisition system to determine the heat flux regimes during a two-phase spray cooling experiment.

4. To determine the effect of liquid film thickness on heat transfer performance in spray cooling applications.

Analysis would be performed on different liquid film thicknesses on the surface of the test substrate to determine how they affect the heat transfer performance.

1.2 Research Rationale and Benefits

The need to develop efficient cooling methods for high heat flux removal applications has become very necessary due to increasingly high heat loads generated by modern plant and/or process systems. Heavy duty electronic systems, power-producing devices, missile systems and laser systems produce heat flux in excess of 100 W/cm^2. Existing cooling methods can barely meet this high heat flux load. The performance of such systems is inherently dependent on how efficiently they can be kept under certain thermal conditions. Thus, metallurgical thermal constraint of such systems is limiting their performance upgrade due to existing insufficient cooling methods to meet the high heat flux removal in excess of 100 W/cm^2.

With the present work of developing efficient cooling methods of high heat flux removal capabilities in range of 100-1000 W/cm^2, however, there will be a great opportunity for system performance upgrade (measured in terms of high heat flux gains, enhanced heat transfer coefficient, low touch temperature and improved system reliability). The developed cooling methods will also allow advanced fabrication techniques using laser technology.

1.3 Organization of Dissertation

The present dissertation has been organized in five chapters. Chapter 1 presents the goal, the need, the formulation of the specific objectives, and the rationale of the research work. Chapter 2 is a thorough literature review on thermal management techniques in general with specific emphasis on spray cooling and the current prominent research works that have helped to advance understanding in spray cooling. Outstanding findings from previous researchers have been considered for the present work and new designs have been developed to enhance the performance of the thermal loop system that has been built for the present research work.

The methods and materials used to carry out the present research work are presented in Chapter 3. The theory behind the problem statement is presented. The description of analytical and numerical techniques used to solve the problem on hand is also presented. Based on the analytical methods, parameters were developed to obtain a test matrix to carry out the experiments. The results and discussions are presented in Chapter 4. Comprehensive conclusions and recommendations based on the results are presented in Chapter 5.

CHAPTER 2

LITERATURE REVIEW

2.1 Scope of Spray Cooling Techniques

Spray cooling as a thermal management method has thoroughly been reviewed from the literature. Experimental and analytical works which have been carried out by researchers in order to understand the principles and mechanism associated with spray cooling heat transfer are reported. In addition, the specific parametric studies by previous researchers are also reported. Numerical techniques that have been conducted to give insights to spray cooling heat transfer have also been reviewed and reported in this chapter. Discussed below are the current research works which have been carried out on spray cooling heat transfer.

Silk and Bracken (2010) investigated spray cooling heat flux enhancement techniques with surface modifications using POCO HTC foam on the heated surface. Their study investigated the effect of POCO HTC foam on spray cooling heat flux. In their experiment, the copper blocks used in the heat flux performance study had a cross-sectional area of 2.0 cm^2. The POCO HTC foam pieces were attached to the copper blocks using two different bonding techniques: (1) S-Bond (R) soldering and (2) high thermal conductivity epoxy as the thermal interface material. For the purpose of baseline comparison, they obtained measurements for a heater block with a flat surface. A 2 x 2 nozzle spray array was used with PF-5060 as the working fluid. Thermal performance data was obtained under nominally degassed conditions with chamber pressure of about

41.4 kPa. From their investigation, the highest heat flux achieved was 133 W/cm^2 using the graphite POCO HTC foam with a nozzle-to-foam distance of 17 mm.

Schwarzkopf, Crowe, Dutta and Li (2009) developed a model to predict the two phase flow pressure characteristics in mesochannels under various heat flux and liquid atomization conditions for spray cooling technique. In their study, they realized that although spray cooling has much higher heat removal ability over pool boiling and jet impingement techniques, this performance improvement was typically associated with small (less than ≤1.5 cm x 1.5 cm) heat acquisition areas (Rini, Chen, & Chow, 2002). They indicated that when cooling large areas with high heat loads, spray cooling performance usually decreases due to: (i) difficulties in managing the flow of multiple atomizers and (ii) the increased spray distance needed to provide adequate fluid coverage. Schwarzkopf et al. therefore designed a mesochannel technique to eliminate these drawbacks associated with large surface areas with multi-nozzle spray cooling.

In their system, liquid was atomized and the high velocity droplets pump the surrounding vapor to create an initial quality at the onset of the channel. The purpose of the initial quality was to promote annular flow throughout the length of the channel, resulting in increased heat transfer. Two-phase heat transfer coefficients in the annular regime were reported to be higher than those in the liquid, bubbly or slug regimes (Chen, 1966; Schwartzkopf, 2005). Thus Schwarzkopf's method (to create an initial quality), is proposed to obtain a thin film of liquid along the wall, promoting annular flow at the beginning of the channel and thereby increasing the heat transfer coefficient throughout the channel relative to traditional flow boiling practices. Schwarzkopf's model was also to understand the pressure drops in the mesochannel to predict the heat transfer performance of such systems. Figure 2.1 shows the experimental setup for their design.

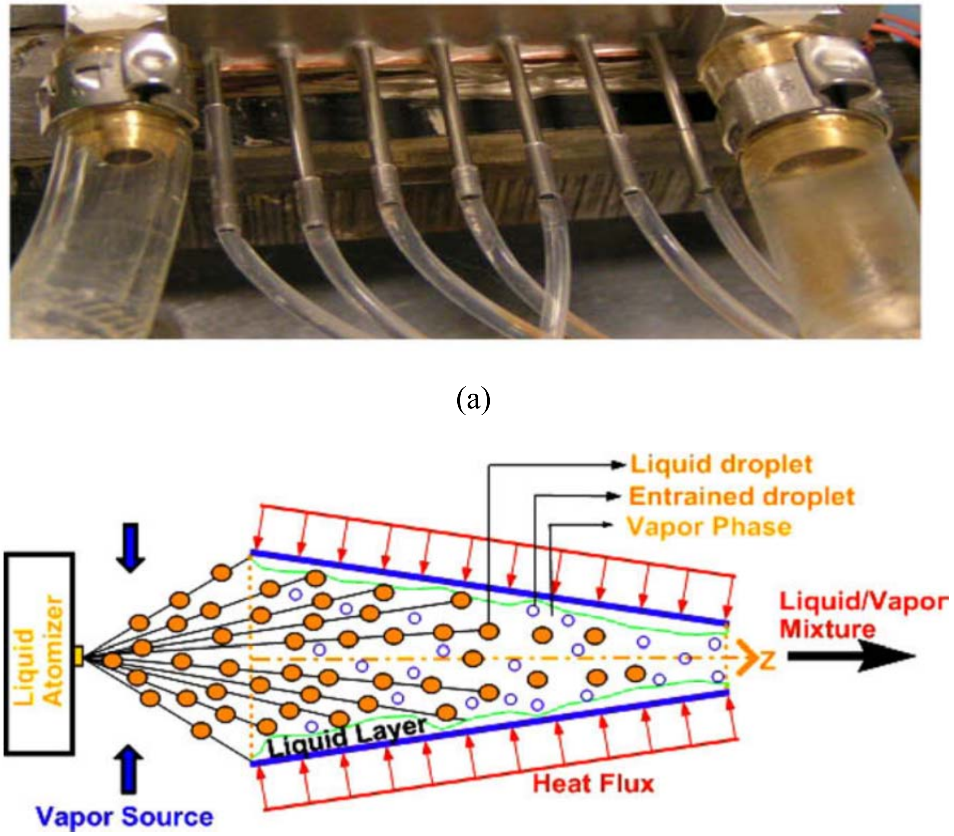

(a)

(b)

Figure 2.1. Spray cooling in a mesochannel: (a) pictorial and (b) schematic drawing (Schwartzkopf, Crowe, Dutta, & Li, 2009)

In their study, one-dimensional numerical model was developed for two-phase flow in a converging mesochannel with phase change due to the heat acquisition from an external source and an initial quality supplied by an atomization process. The predictions of the pseudo one-dimensional numerical model showed a qualitative agreement with the experimental measurement of the pressure distribution in the mesochannel. The entrainment droplets was found to have a negligible effects on the overall momentum transport, but their contribution decreased the mass flow rate of the liquid layer which could lead to dry-out conditions. The liquid film thickness at the heated surface was also found to be dictated by the droplet and vapor momentum, thus controlling heat transfer performance.

Panão and Moreira (2009) investigated the use of intermittent spray cooling as a new technological concept to remove heat fluxes with good performance for meeting the challenges of transient heat dissipation requirements and introduce the potential use of advanced control techniques in the development of thermal management systems. The physics involved in heat transfer processes associated with intermittent spray cooling was also studied. In their experiment, they found out that ‘‘duty cycle”, defined as the percentage of the cyclic time during which the cooling liquid is injected, is the main parameter enabling a more accurate control of the cooling process. The experiments reported evidence that small duty cycles promote heat removal by phase-change. With larger duty cycles, the effect of reducing the time lag between consecutive injections leads to a greater interaction between cycles, eventually leading to the formation of a thin liquid film.

Panão and Moreira indicated that as the duty cycle evolves toward the continuous spray condition, the cooling system’s thermal response improves, but phase-change is mitigated, affecting the system’s performance. Intermittent spray cooling was also compared with continuous spray cooling experiments and liquid savings of 10–90% for the same energetic efficiencies was reported. They also observed that the changes in the system's efficiency as duty cycle approaches the continuous spray working condition (duty cycle = 100%) could be attributed to a switching between heat transfer mechanisms, i.e. from one based on phase-change to another based on thin film boiling. Furthermore, the comparison between the dielectric fluid (HFE-7100) and acetone also suggested that a higher latent heat of evaporation is important to keep the destruction of exergy minimal and maintain the quality of the cooling potential.

The effects of different micro structured surfaces on spray cooling performance was investigated by Sodtke and Stephan (2007). The micro structures consisted of micro pyramids with different heights and widths. They observed significant heat transfer performance due to the surface structures especially at low coolant fluxes. Additionally, high spatial resolution temperature measurements on a smooth heater surface using thermochromic liquid crystals were obtained. Their measurements indicated high local temperature gradients for a regime where the coolant film on the heater was ruptured. Their experimental work included the effects of coolant mass flux on the heat transfer in the low surface temperature regime at low system pressures. In addition, Sodtke and Stephan investigated the influence of the coolant behavior on the heat transfer performance by observing the heater surface with a high-speed infrared camera and performing high resolution temperature measurements on a thin spray cooled foil heater. Figure 2.2 below shows their experimental setup for the investigations on the micro-structured surfaces.

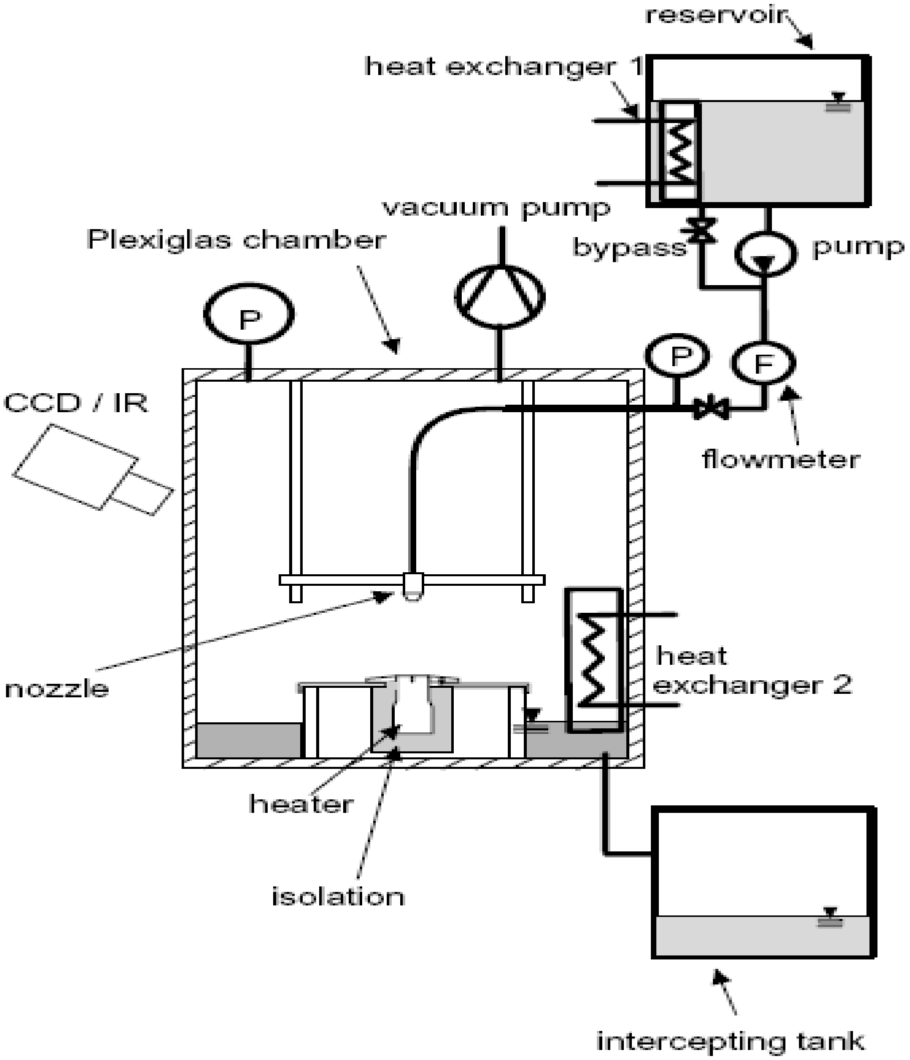

Figure 2.2. Setup for spray cooling on micro-structured surface (Sodtke & Stephan, 2007)

In their experiment, the heat transfer performance of the micro-structures was compared with a smooth surface with surface roughness, Ra < 0.3 μm. The dimensions of the micro-structures used are presented in Table 2.1 below. Constant mass flow rate of 16 kg/h was kept with droplet diameter of 40 -60 μm.

Table 2.1. Height and width for micro-structures on heated surface (Sodtke & Stephan, 2007)

Structure	Height (µm)	Width (µm)
Surface 1	75	150
Surface 2	150	300
Surface 3	225	450

Sodtke and Stephan concluded that spray cooling on micro structured surfaces could lead to significantly improved cooling performances compared to smooth surfaces at the same wall superheat. The authors believe this effect is due to an increased length of the three phase contact line that forms on the structures which leads to a very efficient thin film evaporation. Using an infrared camera, they could show that for a smooth surface the dissipated heat flux increases with increasing contact line length, which occurs on a smooth surface when the coolant film covering the surface at low surface superheats ruptures. Additionally, the temperature distribution shows stronger temperature gradients when the coolant film ruptures.

Effects of spray inclination on two-phase spray cooling and critical heat flux using PF-5052 liquid on a 1.0 x 1.0 cm^2 surface was studied by Visaria and Mudawar (2008b). In their study, they observed that inclination angle had no noticeable effect on the single-phase or two-phase regions of the boiling curve. They found out that maximum critical heat flux (CHF) was always achieved with the spray impinging normal to the test surface, thus, increasing angle of inclination away from the normal decreased CHF appreciably. Maximum CHF of 202 W/cm^2 was observed with 0° spray inclination at highest volumetric flow rate of 1.70 x 10^{-5} m^3/s. Video analysis taken during their experiment showed that inclined sprays produced lateral liquid film flow towards the farthest downstream region of the test surface. They concluded that the liquid film provided partial resistance to dry-out despite the weak volumetric spray flux in the downstream region.

Kulenovic, Mertz, and Groll (2002) deployed visualization and digital image processing techniques to determine the bubble generation frequency, bubble departure diameter and bubble upward flow velocity in boiling experiment with hydrocarbon propane as the working fluid. Bubble departure diameters (0.75-1.2 mm) and maximum bubble upward velocity of 100 mm/s were reported. In their work, they also reported increasing heat transfer coefficient in the range of 0.6-11 W/m^2K with reduced system pressure and increasing heat fluxes.

Yen, Shoji, Takemura, Suzuki, and Kasagi (2006) experimentally determined the local heat transfer coefficient in a convective boiling experiment in transparent single microchannels with similar hydraulic diameters but different shaped cross-section. Circular and square microchannels made of pyrex glass were tested. In addition, they visually observed semi-periodic variations in the flow patterns in both the square and circular microchannels due to the confined space limited to the bubble growth in the radial direction. They reported that higher heat transfer coefficients were recorded for the square microchannels than the circular microchannels because of enhanced nucleation sites at the corners of the square section microchannels.

In a flow boiling experiment, Kharangate, Mudawar, and Hasan (2011) investigated the influence of an inlet vapor void on interfacial behavior of the entry working fluid at heat fluxes up to CHF as well as during the CHF transient. Using a high-speed video imaging techniques, they observed that prior to CHF, a fairly continuous wavy vapor layer begins to develop between the liquid layer covering the heated wall and the heated wall itself, resulting in a complex four-layer flow consisting of the liquid layer covering the insulated walls, the central vapor core, the now separated liquid layer adjacent to the heated wall, and the newly formed wavy vapor layer along the heated wall. They reported that CHF increases monotonically with increases in mass velocity, inlet quality and outlet quality.

Visaria and Mudawar (2008a) studied the effect of subcooling on two-phase spray cooling and CHF. Experiments were performed with dielectric working fluid, FC-77 (with boiling point of 97 ^{o}C at one atmosphere pressure) using three full-cone spray nozzles to assess the influence of subcooling on spray performance and critical heat flux (CHF) from a 1.0 x 1.0 cm^2 test surface. In their study, they found out that increasing the subcooling delayed the onset of boiling but decreased the slope of the nucleate boiling region of the spray boiling curve. The enhancement in CHF was relatively mild at low subcooling and more appreciable at high subcooling. CHF was enhanced by about a 100% when subcooling was increased from 22 ^{o}C to 70 ^{o}C, reaching values as high as 349 W/cm^2.

The FC-77 data generated by Visaria and Mudawar (2008a) in their experiment were combined with prior spray CHF data by (Visaria & Mudawar, 2007) from several studies into a broad CHF database encompassing different nozzles, fluids, flow rates, spray orientations, and subcooling. The entire CHF database was used to modify the effect of subcooling in a previous CHF correlation that was developed for relatively low subcooling. The modified correlation showed excellent predictive capability. Their experimental setup was similar to the previous study (Visaria & Mudawar, 2007). From their investigations, the following conclusions were made:

1. Increasing subcooling enhances CHF. This enhancement is relatively weak at low subcooling but becomes more pronounced for subcooling in excess temperature of 40 ^{o}C.
2. High subcooling is an effective means for dissipating high-heat fluxes. Their present study yielded CHF values as high as 349 W/cm^2 and showed that CHF could be improved by as much as 100% for the same fluid, nozzle, flow rate and orientation when subcooling was increased from 22 to 70 ^{o}C.
3. Aside from increased subcooling, CHF could be increased by increasing volumetric flux and/or decreasing droplet diameter.
4. Subcooling had no appreciable effect on evaporation efficiency. Efficiency is greater for low volumetric fluxes and nozzles that produce smaller droplets.

Empirical correlation in predicting spray cooling performance in critical heat flux applications has been developed by Visaria and Mudawar (2007). Spray cooling database was developed with: water, FC-72, FC-77, FC-87 and PF-5052 for different nozzles, flow rates, subcooling and surface orientation. Figure 2.3 below shows their experimental setup for the heater assembly with fluid spray on the surface of the test substrate.

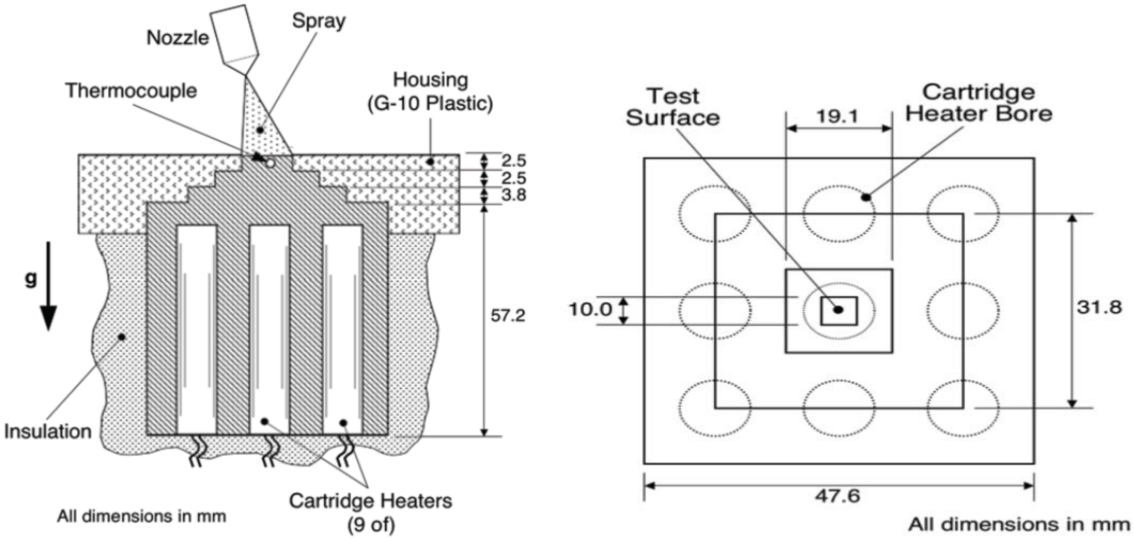

(a) (b)

Figure 2.3. Heater specimen: (a) sectional view and (b) top view (Visaria & Mudawar, 2007)

In their study, they found out that the complexity of spray cooling is coupled with many varying cooling parameters that affect CHF. The parameters were identified to include in addition to the thermophysical properties of the coolant and heated surface: nozzle type, droplet size and volumetric flux (flow rate per unit area) and the spatial distribution for both, spray angle, orifice-to-surface distance, fluid subcooling, (Rybicki & Mudawar, 2006). They indicated that there were also additional practical concerns in implementing spray cooling, such as corrosion and erosion of the intricate interior of spray nozzles, single-point failure as a result of nozzle clogging, and lack of repeatability of droplet hydrodynamics and heat transfer performance for seemingly identical nozzles (Hall & Mudawar, 1995).

In Visaria et al. experimental setup, normal upward-facing PF-5052 sprays, normal and inclined downward-facing PF-5052 sprays, and normal downward-facing FC-77 sprays were studied. The same test heater and two-phase flow loop were used in all three studies; however, different spray chambers and spray nozzle positioning hardware were required to accommodate the different spray orientations. From the series of experiments conducted with FC-72, FC-77, FC-87, water and PF-5052 as the working fluids at different subcoolings, the following conclusions were made:

1. CHF for a normal spray is initiated along the outer periphery of the impact area corresponding to weakest volumetric flux. CHF for a normal spray is maximized when the orifice-to-surface distance is such that the spray impact area just inscribes the square surface of the heating dissipating device. The impact area of an inclined spray is an ellipse and CHF is maximized with an orifice-to-surface distance that just inscribes the major axis within the square surface. While the farthest downstream endpoint of the major axis receives the least volumetric flux from direct liquid impact, liquid flow rate in this region is increased by a liquid film that flows along the surface towards the same endpoint. This film causes the least volumetric flux to commence at the endpoints of the minor axis and CHF commences at these two points.
2. CHF is dictated by the location and magnitude of weakest volumetric flux, and overlap may not influence CHF for several overlap patterns. However, by

increasing the mean volumetric flux, overlap can have appreciable influence on the nucleate boiling region.

Sehmbey, Chow, Pais, and Mahefkey (1995) conducted experimental investigations on spray cooling and the parameters that affect the heat transfer processes associated with spray cooling. Sehmbey et al. found out that other than the properties of the working fluid, the heater surface conditions and droplet velocity are the main parameters which affect the heat transfer performance of the spray cooling. They concluded that the heat transfer is maximized for test surfaces of roughness (Ra <0.1 μm).

Yang, Pais, and Chow (1993) investigated the effect of air and steam as secondary gas in spray cooling heat transfer. In their study the secondary gas was used to atomize the liquid working fluid. Yang et al. concluded that increasing the secondary gas (air) proportion with all flow rates increased the CHF to an optimum value beyond which further increase in air flow did not affect the CHF. The air quality in the working fluid flow rate to achieve the optimum CHF was not reported. In Yang et al.'s experiment, 12.4-17.3 μm droplet diameters, 25.6-57.3 m/s droplet velocity and 85 -235 μm film thickness were also observed.

Pais, Chow, and Mahefkey (1992) studied the effect of surface enhancement (roughness) on heat transfer mechanism of spray cooling. Surface roughness of 0.3, 14 and 22 μm on 1.0 cm^2 copper surface using air-atomizing nozzle at nozzle height of 23 mm was used with de-ionized water as the working fluid. Spray droplet diameter ranged between 7-28 μm with liquid and air flow rates of 0.1-1.0 L/h and 0.1-0.4 L/h respectively. They observed that the surface with the 0.3 μm surface roughness had the maximum CHF of 1250 W/cm^2. The peak CHF was attributed to enhanced nucleate boiling and early bubble departure from the heated surface.

Most research works in spray cooling have been concentrated on identifying the cooling parameters that affect the heat transfer performance. The heat transfer performance is measured in terms of heat transfer coefficient and critical heat flux. A summary of recent research works in identifying the cooling parameters and their effect on heat transfer performance is presented in Table 2.2 below. The experimental test conditions and working fluids which were used by the researchers are also reported.

Table 2.2. Cooling parameters and their effect on CHF in spray cooling

Author	Experimental work & Research findings
Estes & Mudawar (1995)	They found out that boiling or heat flux curve was maximized with low volumetric flux due to pronounced evaporation efficiency. The CHF was also found to increase with smaller fluid droplet diameters. They identified that the Sauter mean diameter (SMD) of the droplet depended on the nozzle orifice diameter, fluid conditions, Weber and Reynolds numbers. FC-72, FC-77, FC-87, water and PF-5052 fluids were used for this study.
Mudawar & Estes (1996)	Sub-cooling of working fluid increased the CHF monotonically. The CHF was also maximized at a volumetric flux with optimum nozzle to heated surface distance on a 12.7 mm x 12.7 mm surface.
Rini, Chen, & Chow (2002)	Heat flux data comparisons were made for pool boiling and spray cooling. They observed that heat flux increased by 50% with spray cooling over pool boiling. The increase in CHF was attributed to formation of more nucleation points due to puncturing of the liquid film and vapor entrainment onto the heater surface.

Table 2.2 (continued)

Horacek, Kiger, & Kim (2005)	The effect of gas concentrations in the liquid working fluid on CHF was studied. They observed that the presence of non-condensable gases (NCG) shifted the saturation temperature of the liquid and increased the subcooling of the liquid being sprayed onto the heated surface. The heat flux was enhanced with subcooling.
Schwartzkopf et al, (2004)	The effect of spray angle on heat flux was studied. It was observed that CHF (~63 W/cm^2) was achieved with spray angle between 0^o and 40^o at 1.4 cm nozzle to heater surface distance with PF-5060 as the working fluid and at pressure of 101 kPa.
Lin, Ponnappan, Yerkes, & Hager (2004)	In 2004, Lin et al. investigated the effect of heated surface area size on spray cooling and heat transfer performance. The heat transfer performance was measured in terms of CHF. From their investigations they demonstrated that heat flux reductions as high as 30% results due to surface area scale-ups from less than 2.0 cm^2 to 3.0 cm^2. The heat flux reduction was due to stagnation zones with low bulk fluid momentum flux when multi-nozzles are used.
Selvam, Balda, Paneer, & Bhaskara (2005); Selvam, Paneer, Lin, & Ponnappan (2006); Paneer, Selvam, Sarkar, & Ponnappan (2005)	The effect of droplet impact on growing vapor bubble in a 44.17 μm film thickness was simulated. The working fluid droplet size and velocity were 30 μm and 2.55 m/s respectively. They found out from the direct numerical simulation that droplet impingement during bubble nucleation increased mixing of the thin liquid film which increased the heat flux. Subsequent direct numerical simulation study also showed that increasing the droplet velocity increased Nusselt number (Nu) to a certain level beyond which the Nu number remains constant. The simulations also showed that the maximum heat flux increased linearly with thermal conductivity; (Paneer Selvam, Sarkar, & Ponnappan, 2006). The effect of density and latent heat of evaporation on the heat flux was found to be negligible. However, they explained that the latent heat of evaporation affected the process since lower latent heat of evaporation increased the rate of evaporation of the fluid from the heated surface.

In the work of Silk, Kim, and Kiger (2006), porous channels were used to mitigate the heat flux reduction that occurred due to surface area scale-up. From their investigation, they observed that the porous channels reduced the stagnation zones which occurred due to the use of multi-nozzles. The porous channel structures provided about 75% increase in CHF (140 W/cm^2) relative to the normal flat surface case of CHF (~ 80 W/cm^2).

Kim (2007) conducted a review on the state of the art of spray cooling and the heat transfer mechanisms associated with it. In his paper, it was reviewed that high heat transfer mechanism observed in spray cooling was due to the efficiency by which liquid molecules escape into the vapor/ambient from the surface of a thin liquid film. Pais, Tilton, Chow, and Mahefkey (1989) reported that a thin liquid layer forms on the heated surface through which heat is conducted. Because the top of the film is assumed to be at the saturation temperature, thinner films result in higher heat transfer. Large heat transfer at small superheats requires the existence of an ultrathin liquid film on the surface. For example, a 1.4 µm thick layer of water is required to transfer 1000 W/cm^2 of heat at a superheat of 20 ^{0}C. Their analytical model suggested that the optimum heat transfer would occur by using the smallest possible droplets and the highest percentage of surface saturation to obtain the thinnest liquid film. They also suggested that the impact velocity should be carefully chosen such that the maximum droplet spread is achieved without droplet rebound from the surface.

Kizito, Gordon, and Tryggvason (2005) studied droplet impingement dynamics on a heated surface during spray cooling. In particular, numerical and modeling tools were used to determine characteristic non-dimensional parametric dependence in the design of efficient and effective spray cooling processes for practical fluids and working conditions. Specific non-dimensional parameters studied after normalizing the conservation equations were: Reynolds number (Re), Weber number (We), Peclet number (Pe), density, thermal conductivity, aspect and viscosity ratios. In their direct numerical study, they observed that at a higher impact velocity, 3.15 m/s, (thus Re = 1436, and We = 559 for the test conditions investigated), the droplet forms splashed products. The splashed droplet products decreased the heat transfer due to reduced interaction between the fluid and the heated surface. It was also observed that at constant Weber number with increasing viscosity, the Reynolds number was reduced. This caused the droplet to deform into a disc-like shape thereby increasing the surface area of the fluid in contact with the heated substrate and hence increasing the heat transfer.

Yang, Chow, and Pais (1996) conducted a study on the effect of secondary gas in spray cooling. In their investigation, they used an air-atomized nozzle to spray distilled water over an area approximately 12 mm in diameter. The heater surface was constructed of copper with an exposed area of 11 x 11 mm^2. Water flow rates up to 3 liter/h were used. The droplet diameters and velocities ranged from 10–18 μm and 25–58 m/s, respectively. Heat flux of about 820 W/cm^2 was achieved at a flow rate of 2 liter/h and an air pressure of 446 kPa. They suggested that the observed high heat transfer was due to the generation of many nucleation sites within the liquid film that form when the individual liquid droplets strike the liquid surface. When these droplets penetrate into the liquid film, the entrained gases are released and form nucleation sites from which bubbles can grow. The droplets can also puncture the rapidly growing bubbles, increasing the bubble frequency and the heat transfer. They identified that although the number of nucleation sites is proportional to the droplet flux (the liquid flow rate), the heat transfer is not proportional to liquid flow rate since the liquid film thickness also increases.

Wang and Liu (2010) experimentally studied the effects of spray inclination on spray cooling performance in non-boiling regime. From their experimental results, they concluded that film evaporation was very important to heat transfer in non-boiling regime of spray cooling. They observed that as the test surface temperature increased, film evaporation increased as well, and heat transfer performance was enhanced. They identified an inflexion point in the heat transfer curves when the water temperature reached 85-90°C. They reported that after the inflexion point, the heat flux as well as the heat transfer coefficient and the cooling efficiencies increased quickly due to boiling. It was also observed from their study, the development of a stagnation zone at the center of the heated surface resulting from the impingement flow. They found out that heat transfer performance could be increased by increasing the inclination angle which strengthened the effect of washing and reduced the area of stagnation zone.

Stodke and Stephan (2005) investigated spray cooling heat transfer and CHF with microstructured and microporous surfaces using water and a full-cone spray atomizer (60^{o} cone angle, impact velocity approximately 11 m/s, mean droplet diameter, $d_{32} \sim 100$ μm). Pyramidal microgrooves 75 μm high with 150 μm pitch were manufactured onto a 20 mm diameter copper cylinder. The micro-pyramids had the same height and base length as the microgrooves. They observed that both micro-structured surfaces increased the wetted area by √2. The porous layer was 100 μm thick and was created using a mixture of MEK, epoxy, and aluminum powder with an average size of 35 μm.

From Stodke and Stephan's findings, they indicated that a small increase in heat transfer was observed for both micro-structured surfaces at a standoff distance of 25 mm (highest mass flux); very large increases were observed when the standoff distance was increased. A maximum heat flux of 97 W/cm^2 was observed at a standoff distance of 35 mm for the micro-pyramid surface compared with 30 W/cm^2 on the flat surface at a superheat of 12 ^{o}C, which was much larger than the surface area enhancement. Significant degradation in critical heat flux for the micro-porous surface (3.2 W/cm^2) was observed compared with the uncoated surface due to the poor thermal conductivity of the epoxy binder. This was in contrast to the results obtained by Kim et al. (2004) who found out that the heat transfer from micro-porous coated surface increased by 50% relative to the uncoated surface.

Lin and Ponnappan (2003) studied the heat transfer characteristics of spray cooling in closed loops. In their experiment, eight miniature nozzles in a multi-nozzle plate were used to generate a spray array targeting on a 1 x 2 cm^2 cooling surface. FC-87, FC-72, methanol and water were used as the working fluids. Thermal performance data for the multi-nozzle spray cooling in the confined and closed system were obtained at various operating temperatures, nozzle pressure drops (from 0.69 to 3.10 bars) and heat fluxes. It was observed that spray cooling could reach the critical heat fluxes up to 90 W/cm^2 with fluorocarbon fluids and 490 W/cm^2 with methanol. For water, the critical heat flux was observed to be higher than 500 W/cm^2. Air as secondary fluid in atomizing the working fluid was also established. The air atomization technique introduced in the spray cooling system with FC-72 fluid was observed to have a significant influence on heat transfer characteristics of the spray over the cooling surface. The experimental setup for their closed-loop spray cooling investigation is shown in Figure 2.4 below.

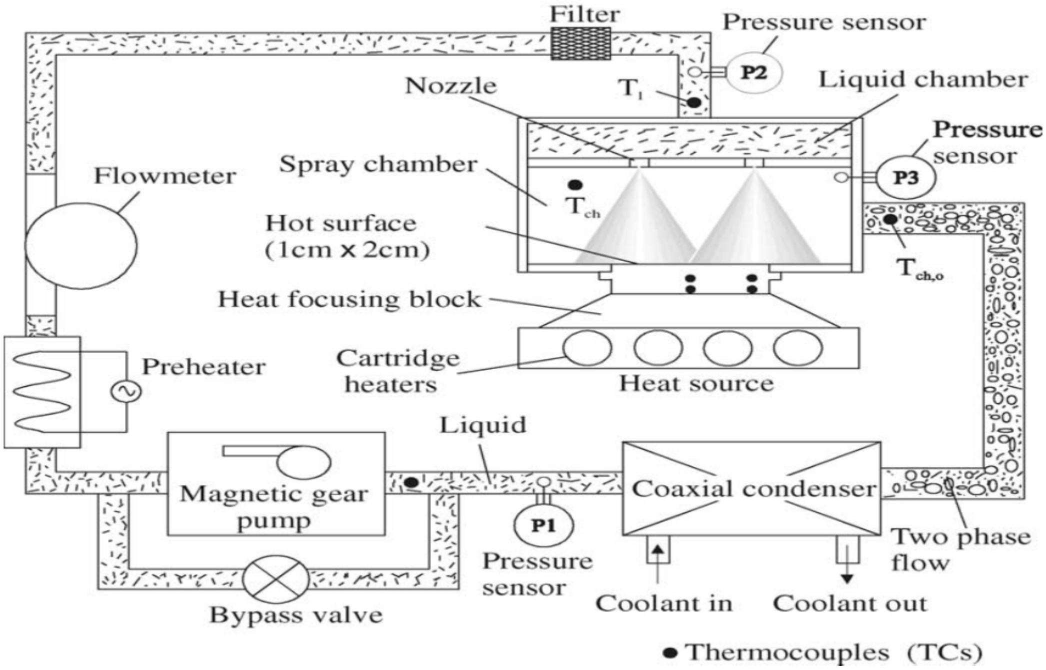

Figure 2.4. Setup for a closed loop spray cooling (Lin & Ponnappan, 2003)

From their investigation, they reported that non-condensable gas adversely affects the overall heat transfer of the closed loop spray cooling system at heat fluxes lower than CHF because of a higher thermal resistance to the condensation heat transfer. They indicated that the system with pure FC-72 had a better thermal performance of the spray over the surface at heat fluxes less than 70 W/cm^2. However, at heat fluxes greater than

70 W/cm^2, the system containing FC-72 and air showed a better thermal performance over the surface. Nucleate boiling heat transfer, convection heat transfer and evaporation from the surface of the liquid film were observed to be the main heat transfer processes associated with the closed-loop spray cooling. From the experiment, they realized that interaction between the spray cone and surrounding fluid was stronger in the case of multi-nozzle spray cooling than in the case of single nozzle spray cooling. At various operating temperatures, nozzle pressure drops (from 0.69 to 3.10 bar) and for a given surface superheat, the heat flux increased with the volumetric flux. They concluded that pressure drop of 1.72 bars or lower are not optimum for the maximum heat removal.

In the work of Zhang, Ting, and Jiao (2008), liquid film flow down a heated and/or cooled vertical plate was experimentally investigated using an infra-red imaging camera. They observed that for a heated plate, the flowing liquid film contracted reducing the wetted surface area; whilst for a cooled plate, the liquid film extended thereby increasing the wetted surface area. The contraction and/or extension of the flowing liquid film on the heated and/or cooled surface were attributed to lateral Marangoni effect due to a heating temperature difference and the liquid flow rate.

2.2 Summary of Reviewed Work

Review of current literature on spray cooling mechanism as a thermal control method has indicated a tremendous advancement in developing methods to meet demands of high heat loads management. Many parameters have been reported to dictate heat transfer performance and Critical Heat Flux (CHF) in pray cooling. Table 2.3 presents some specific critical heat fluxes that have been obtained by some researchers.

Table 2.3. Critical heat flux (CHF) measurements by selected researchers

Author	Parametric study	CHF [W/cm^2]
Visaria & Mudawar. (2008)	Subcooling on spray cooling & CHF	349
Pais et al (1992)	Enhanced surface on spray cooling and CHF. Maximum CHF was achieved with 0.3 µm surface roughness	1250
Yang et al (1996)	Air atomization in spray on CHF	820
Stodke & Stephan (2005)	Microstructure effect on CHF in spray cooling	97
Lin et al (2004)	Heat transfer characteristics of spray cooling in a closed loop	490
Pautsch & Shedd (2005)	Spray impingement cooling with single- and multiple-nozzle arrays	77.8
Silk & Bracken (2010)	Surface enhancement using POCO HTC foam on the heated surface	133
Visaria et al. (2008b)	Spray inclination on CHF	202
Silk et al. (2007)	Enhanced surfaces: Porous surface to mitigate heat flux reduction due to surface area scale-ups	140

Summarized below are details of the major techniques and contributions that have been made by other researchers in spray cooling heat transfer schemes. The parametric studies of the research works are reported. Optimal test conditions from the literature have also been considered for the present experimental works.

Critical heat flux (CHF) with spray cooling heat transfer on modified surfaces have been identified to be higher than on smooth surfaces for same operating conditions:

(Silk & Bracken, 2010; Sodtke & Stephan, 2007; Bostanci et al., 2009). It is reported that the micro-structured surfaces increase the three phase contact line and the number of nucleation sites which increase heat transfer performance on the test substrate. However, the optimal design and the criteria limits of such modified surfaces and how they enhance heat transfer and critical heat flux in spray cooling has not been reported. Thus, information on the exact coupling and driving mechanism between modified surfaces and critical heat flux (CHF) in spray cooling is lacking.

Also, most spray cooling heat transfer experiments have been conducted on small test surface areas (usually < 3cm^2), (Schwartzkopf, et al., 2009). It is indicated that spray cooling is not that efficient for large surface areas due to fluid management issues (Lin, et al., 2004). The relation between test surface areas and critical heat flux in spray cooling heat transfer is therefore yet to be determined.

The working fluid droplet diameter and volumetric flux are also reported to influence the heat transfer performance in spray cooling heat transfer (Visaria & Mudawar, 2007; Selvam, et al. 2005; Kim, 2007; Estes & Mudawar, 1995). Review indicates that these two parameters dictate the level of liquid film on the heated substrate. Liquid film evaporation on the test surface increases heat transfer performance (Kim, 2007). Experimental investigation by Toda (1972 & 1973) reported heat flux as a function of the wall superheat and thin liquid film thickness that forms on the test surface. They observed that for a critical thin liquid film thickness on the test surface, direct liquid evaporation into the vapor phase ensues without bubble generation. However, for film thickness beyond the critical film thickness, nucleate boiling was prominent and heat flux was reduced due to vapor patches on the test surface which decreased the wetted surface area. In a spray cooling experiment of Yang, Pais, and Chow (1993 & 1996), film thickness measurement of 85-235 μm was reported. It was reported that the film thickness augmented the heat transfer mechanism; however, the heat flux magnitudes were not reported in the paper. Model simulation of fluid droplet impact on vapor bubble growth and bursting in a thin liquid film of thickness 44.17 μm has been investigated (Selvam, Lin & Ponnappan, 2006; Selvam, Bhaskara, Balda, Barlow & Elshabini, 2005; Selvam, Lin & Ponnappan, 2005). Their study showed that droplet impingement during bubble nucleation increased mixing of the thin liquid film on the heater surface which also increased the heat flux.

Experimental work on film thickness measurements using high speed camera equipped with a long distance microscope was carried out by Martinez-Galvan, Ramos, and Anton (2011). In their investigation, they found out that there exists a relation between the variation in the average Nusselt number and the film thickness along the spray cooling boiling curve. They indicated that the heat transfer regimes along that curve are related not only with a variation in the average Nusselt number but also with changes in the film thickness.

Gong, Ma, and Dinh (2010) deployed micro-conductive probes and confocal optical sensors to measure the instantaneous film thickness in an isothermal flow over a silicon wafer to obtain the film thickness profile and the interfacial wave characteristics. The dynamic thickness of an evaporating film on a horizontal silicon wafer surface was recorded using the optical sensor in their experiment. Their results indicated that a critical film thickness (84 μm) initiated film instability on the silicon wafer at heat flux of about 56 kW/m^2 (5.6 W/cm^2). Bhattacharya, Samanta, and Chakraborty (2009) estimated the heat transfer involved in spray evaporative cooling from single droplet studies viewpoint with the notion that a spray is equivalent to a multi-droplet array of liquid at low spray flux density. They developed an analytical expression of droplet evaporation time from fundamental heat transfer perspective to estimate strip cooling rate. Their analytical model developed predicts that it is possible to achieve an anomalously high strip cooling rate of Ultra Fast Cooling in a 4 mm thick steel strip by spray evaporative cooling provided the fluid droplet size is reduced to 70 μm. They also observed that smaller droplets were capable of providing the increased cooling load of Ultra Fast Cooling for thicker steel strips.

Adiabatic and diabatic film thickness measurement was conducted by Pautsch and Shedd (2006) in a spray cooling experiment using FC-72 as the working fluid. In their experiment, they observed that regions of the test die that exhibited the poorest heat transfer performance had the thickest liquid film. The reduced heat transfer performance was attributed to vapor patches in the thick liquid film.

Heat transfer enhancement has also been reported when secondary gas (or vapor) is used in the atomization of the working fluid (Yang, et al., 1993). The main purpose of using a secondary gas is to produce very fine (small) fluid droplets at the nozzle tip upon impingement on the test substrate. It had been observed, however, that after a certain proportion of the secondary gas, heat transfer and critical heat flux decrease with increasing secondary gas in the atomization process. Information on optimal proportions of the secondary gas to enhance the heat transfer performance is also lacking in literature.

2.3 Challenges of Spray Cooling Heat Transfer

Many parameters have been reported by other researchers to control critical heat flux and heat transfer performance in spray cooling techniques. The literature has indicated that the challenges in spray cooling applications are attributed to fluid management issues and experimental test conditions. The following paragraphs present some of the difficulties which have been reported in literature with spray cooling mechanism.

In spray cooling mechanism, the prevailing pressure and fluid conditions at the orifice of the nozzle and in the heater chamber dictate the hydrodynamics of the fluid droplets as they impinge on the heated surface. To obtain even fluid distribution on the impact surface for negligible temperature gradients during spray cooling, uniform fluid droplets must be established. Current research work has indicated that it is very difficult to obtain uniform and repeatable fluid spray (Hall and Mudawar, 1995). The lack of repeatability of droplet hydrodynamic could be due to pressure fluctuations in the heating chamber during phase change as more fluid vapor is formed. Single point nozzle clogging can also lead to conditional fluctuations at the nozzle orifice which cause uneven droplet spray.

Visaria and Mudawar (2007 and 2008a) found out that CHF is initiated at points of weakest volumetric flux. Fluid droplets splashing and rebound lead to dry-outs at such critical points. Thus in order to prevent surface dry-out, an optimum volumetric flux must be maintained to ensure liquid film on the heated surface. In view of this, a film thickness must always be ensured on the impact/heated surface.

At the onset of spray cooling, high surface superheats can lead to droplet skidding on the heated surface due to Leidenfrost effects. Droplet skidding on the heated surface delays liquid evaporation. Delay in liquid evaporation decreases the heat transfer performance in spray cooling applications. To prevent this undesirable phenomenon, low surface superheats have been suggested by other researchers to be ensured at the onset of spray cooling.

Spray cooling methods are deployed in industrial equipment and processes where control and/or removal of high heat loads are desired. Examples of industrial equipment and processes where spray cooling has been applied include laser systems, metallurgy, and energy conversion devices. Based on the knowledge gaps which were identified in the literature, the specific objectives for this research work were developed. The specific objectives and the tasks as presented in Chapter 1 have been addressed by developing the necessary methods and materials to meet the overall goal of this research work. The methods and materials which were developed to achieve the specific objectives are presented in Chapter 3 below.

CHAPTER 3

MATERIALS AND METHODS

3.1 Problem Description

The present work develops thermal control methods for high heat flux removal applications. Specifically, a thermal management scheme is developed for higher heat fluxes in the range of 100-1000 W/cm^2. To achieve higher heat fluxes in this magnitude, a two-phase thermal loop has been constructed for the present study. Figure 3.1 shows a schematic of the problem formulation of spray impingement on the heated surface.

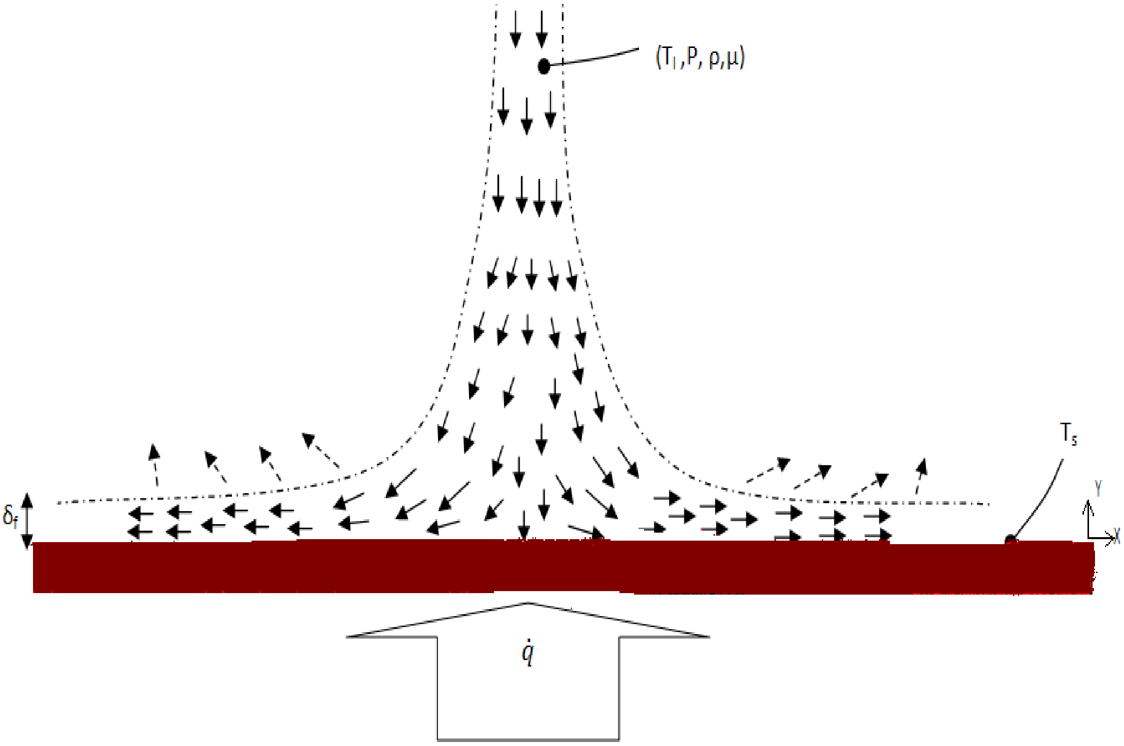

Figure 3.1. Spray impingement on a heated surface subjected to heat flux $\dot{q}$.

In Figure 3.1, the test substrate is heated at the bottom with heat flux ($\dot{q}$). As the substrate is heated, fluid spray at temperature T_l is impinged on the heated test surface at temperature T_s. The fluid spray conditions (pressure, volumetric flux, and flow rate) and the substrate surface conditions are measured a priori to fluid spray impingement. On the heated test surface, a liquid film develops. As the liquid film on the heated surface reaches its boiling point, phase change occurs. The vapor that is formed due to the phase change of the liquid fluid leaves the test surface and is replaced by new liquid fluid. The development of liquid film thickness, δ_f, on the heated surface and its effect on heat flux and overall heat transfer mechanism at various test conditions is determined. Analytical methods and bench test have also been conducted to give insight to the heat transfer mechanism associated with the spray cooling technique, with more emphasis on liquid film development on the heated surface, test surface enhancement and/or modification techniques and the area size of the test substrate. The analytical considerations for the present work are presented in the following section.

3.1.1 The Conservative Laws

The present problem is described with the fluid transport properties in the form of equations using the three conservative laws. The three conservative laws (mass, momentum and energy) applied to the physical problem are presented below in the form of differential equations. Equations 3.1, 3.2 and 3.3 present the physical laws which describe the conservation of mass, momentum and energy respectively for a 3-D formulation. The differential equations are presented in the conservative form.

Conservation of Mass:

$$\frac{\partial \rho}{\partial t}+\frac{\partial(\rho u)}{\partial x}+\frac{\partial(\rho v)}{\partial y}+\frac{\partial(\rho w)}{\partial z}=0 \tag{3.1}$$

Momentum equation in x-direction:

$$\begin{aligned}\frac{\partial(\rho u)}{\partial t}+\frac{\partial(\rho u^2)}{\partial x}+\frac{\partial(\rho uv)}{\partial y}+\frac{\partial(\rho uw)}{\partial z}&=-\frac{\partial P}{\partial x}+\frac{\partial}{\partial \mathrm{x}}\left(\lambda\nabla\bullet\overline{\mathrm{V}}+2\mu\frac{\partial u}{\partial \mathrm{x}}\right)+\\&\frac{\partial}{\partial y}\left[\mu\left(\frac{\partial v}{\partial \mathrm{x}}+\frac{\partial u}{\partial y}\right)\right]+\frac{\partial}{\partial \mathrm{z}}\left[\mu\left(\frac{\partial u}{\partial z}+\frac{\partial w}{\partial x}\right)\right]+\rho f_x\end{aligned} \tag{3.2a}$$

Momentum equation in y-direction:

$$\begin{aligned}\frac{\partial(\rho v)}{\partial t}+\frac{\partial(\rho uv)}{\partial x}+\frac{\partial(\rho v^2)}{\partial y}+\frac{\partial(\rho vw)}{\partial z}&=-\frac{\partial P}{\partial y}+\frac{\partial}{\partial x}\left[\mu\left(\frac{\partial v}{\partial \mathrm{x}}+\frac{\partial u}{\partial y}\right)\right]+\\&\frac{\partial}{\partial y}\left(\lambda\nabla\bullet\overline{\mathrm{V}}+2\mu\frac{\partial v}{\partial \mathrm{y}}\right)+\frac{\partial}{\partial \mathrm{z}}\left[\mu\left(\frac{\partial w}{\partial y}+\frac{\partial v}{\partial \mathrm{z}}\right)\right]+\rho f_y\end{aligned} \tag{3.2b}$$

Momentum equation in z-direction:

$$\begin{aligned}\frac{\partial(\rho w)}{\partial t}+\frac{\partial(\rho uw)}{\partial x}+\frac{\partial(\rho vw)}{\partial y}+\frac{\partial(\rho ww)}{\partial z}&=-\frac{\partial P}{\partial \mathrm{z}}+\frac{\partial}{\partial x}\left[\mu\left(\frac{\partial u}{\partial \mathrm{z}}+\frac{\partial w}{\partial x}\right)\right]+\\&\frac{\partial}{\partial y}\left[\mu\left(\frac{\partial w}{\partial y}+\frac{\partial v}{\partial \mathrm{z}}\right)\right]+\frac{\partial}{\partial \mathrm{z}}\left(\lambda\nabla\bullet\overline{\mathrm{V}}+2\mu\frac{\partial w}{\partial \mathrm{z}}\right)+\rho f_z\end{aligned} \tag{3.2c}$$

Conservation of Energy:

$$\begin{aligned}\frac{\partial(\rho e)}{\partial t}+\nabla\bullet\left(\rho e\,\overline{\mathrm{V}}\right)&=\rho\,\dot{q}+\frac{\partial}{\partial x}\left(k\frac{\partial T}{\partial x}\right)+\frac{\partial}{\partial y}\left(k\frac{\partial T}{\partial y}\right)+\frac{\partial}{\partial z}\left(k\frac{\partial T}{\partial z}\right)-\\&p\left(\frac{\partial u}{\partial x}+\frac{\partial v}{\partial y}+\frac{\partial w}{\partial z}\right)+\lambda\left(\frac{\partial u}{\partial x}+\frac{\partial v}{\partial y}+\frac{\partial w}{\partial z}\right)^2+\\&\mu\left[2\left(\frac{\partial u}{\partial x}\right)^2+2\left(\frac{\partial v}{\partial \mathrm{y}}\right)^2+2\left(\frac{\partial w}{\partial \mathrm{z}}\right)^2+\left(\frac{\partial u}{\partial y}+\frac{\partial v}{\partial x}\right)^2+\left(\frac{\partial u}{\partial z}+\frac{\partial w}{\partial x}\right)^2+\left(\frac{\partial v}{\partial z}+\frac{\partial w}{\partial y}\right)^2\right]\end{aligned} \tag{3.3}$$

3.1.2 Phase Change Equations

The complete conservation laws have been applied to a 3-D system describing the liquid and/or gas fluid transport properties. The internal energy of the energy Equation 3.3 has been split into the sensible and latent components for phase change heat transfer. The simplified complete phase change equations for a 3-D system are presented in this section. Equations 3.4, 3.5 and 3.6 below present the phase change equations of conservation of mass, momentum and energy respectively for the underlying problem with subscript (i) indicating the phase of the fluid.

Continuity Equation:

$$\frac{\partial \rho_i}{\partial t}+\frac{\partial(\rho_i u)}{\partial x}+\frac{\partial(\rho_i v)}{\partial y}+\frac{\partial(\rho_i w)}{\partial z}=0 \tag{3.4}$$

X-momentum Equation:

$$\frac{\partial(\rho_i u)}{\partial t}+\frac{\partial(\rho_i uu)}{\partial x}+\frac{\partial(\rho_i uv)}{\partial y}+\frac{\partial(\rho_i uw)}{\partial z}=-\frac{\partial P}{\partial x}+ \left[\frac{\partial}{\partial x}\left(\mu_i\frac{\partial u}{\partial x}\right)+\frac{\partial}{\partial y}\left(\mu_i\frac{\partial u}{\partial y}\right)+\frac{\partial}{\partial z}\left(\mu_i\frac{\partial u}{\partial z}\right)\right] \tag{3.5a}$$

Y-momentum Equation:

$$\frac{\partial(\rho_i v)}{\partial t}+\frac{\partial(\rho_i uv)}{\partial x}+\frac{\partial(\rho_i vv)}{\partial y}+\frac{\partial(\rho_i vw)}{\partial z}=-\frac{\partial P}{\partial y}+ \left[\frac{\partial}{\partial x}\left(\mu_i\frac{\partial v}{\partial x}\right)+\frac{\partial}{\partial y}\left(\mu_i\frac{\partial v}{\partial y}\right)+\frac{\partial}{\partial z}\left(\mu_i\frac{\partial v}{\partial z}\right)\right]-g\left(\rho_i-\rho_{ref}\right) \tag{3.5b}$$

Z-momentum Equation:

$$\frac{\partial(\rho_i w)}{\partial t}+\frac{\partial(\rho_i\, uw)}{\partial x}+\frac{\partial(\rho_i\, vw)}{\partial y}+\frac{\partial(\rho_i\, ww)}{\partial z}=-\frac{\partial P}{\partial z}+ \left[\frac{\partial}{\partial x}\left(\mu_i\frac{\partial w}{\partial x}\right)+\frac{\partial}{\partial y}\left(\mu_i\frac{\partial w}{\partial y}\right)+\frac{\partial}{\partial z}\left(\mu_i\frac{\partial w}{\partial z}\right)\right] \tag{3.5c}$$

Energy Equation:

$$\frac{\partial(\rho_i Cp_i T)}{\partial t}+\frac{\partial(\rho_i u\, Cp_i T)}{\partial x}+\frac{\partial(\rho_i\, v Cp_i T)}{\partial y}+\frac{\partial(\rho_i\, w Cp_i T)}{\partial z}= \left[\frac{\partial}{\partial x}\left(k_i\frac{\partial T}{\partial x}\right)+\frac{\partial}{\partial y}\left(k_i\frac{\partial T}{\partial y}\right)+\frac{\partial}{\partial z}\left(k_i\frac{\partial T}{\partial z}\right)\right]- h_{fg}\left[\left(\frac{\partial(\rho_i f)}{\partial t}\right)+\left(\frac{\partial(\rho_i u\, f)}{\partial x}\right)+\left(\frac{\partial(\rho_i v\, f)}{\partial y}\right)+\left(\frac{\partial(\rho_i w\, f)}{\partial z}\right)\right] \tag{3.6}$$

3.1.3 Boundary and Initial Conditions

The boundary and initial conditions to the present problem that describe the transport phenomenon are presented as Equations 3.7-3.9. The no-slip, heat flux and phase change boundary conditions were applied to analyze the physical phenomenon. The specific boundary conditions are presented below.

No Slip Condition at the wall: At the surface of the test substrate, the working fluid assumes zero velocity relative to the surface. Equation 3.7 below presents the no-slip condition of the working fluid on the test surface.

$$V\big|_{y=0}=0 \tag{3.7}$$

Conduction and Phase Change at the wall: At the solid-liquid interface, the heat transfer mechanism is by phase change and conduction. Liquid fluid conducts heat and when it has reached saturation conditions it changes phase into vapor. Equation 3.8 describes this boundary condition.

$$\dot{q} = \rho_l \cdot h_{fg} V_n - k_f \left. \frac{\partial T}{\partial y} \right|_{y=0} \tag{3.8}$$

<u>Interface Boundary Condition</u>: At the fluid-vapor interface, the conservation of mass requires that the mass of liquid that vaporizes be balanced by the amount of vapor formed and is presented as equation 3.9.

$$\rho_g \vec{v} \cdot \vec{n} = (\rho_l - \rho_g) V_n \tag{3.9}$$

From equation 3.9 above, the normal velocity, V_n, of the receding interface is given by Stefan relation 3.10: Equation 3.10 also satisfies the conservation of energy for a phase change heat transfer at the interface. The interfacial energy balance has been presented in the form of heat flux and latent heat of vaporization and is presented as Equation 3.10.

$$\rho_l \cdot h_{fg} V_n = k_l \left. \frac{\partial T_l}{\partial y} \right|_{y=y_{\text{int}}} - k_g \left. \frac{\partial T_g}{\partial y} \right|_{y=y_{\text{int}}} \tag{3.10}$$

3.1.4 Scaling Analysis

The phase change Equations 3.4-3.6 with steady-state conditions have been scaled with the appropriate scaling parameters. The scaling parameters for the fluid transport properties as well as the fluid thermophysical properties are presented below.

$$x^* = \frac{x}{D} \qquad y^* = \frac{y}{D} \qquad z^* = \frac{z}{D} \qquad u^* = \frac{u}{V_\infty}$$

$$v^* = \frac{v}{V_\infty} \qquad w^* = \frac{w}{V_\infty} \qquad P^* = \frac{P}{\rho V_\infty^2} \qquad T^* = \frac{T - T_l}{T_{sat} - T_l}$$

$$\rho = \frac{\rho_i}{\rho_l} \qquad k = \frac{k_i}{k_l} \qquad \mu = \frac{\mu_i}{\mu_l} \qquad Cp = \frac{Cp_i}{Cp_l}$$

Equations 3.11-3.13 present the phase change equations after the scaling analysis.

Continuity Equation:

$$\frac{\partial u^*}{\partial x^*} + \frac{\partial v^*}{\partial y^*} + \frac{\partial w^*}{\partial z^*} = 0 \tag{3.11}$$

X-momentum Equation:

$$u^* \frac{\partial u^*}{\partial x^*} + v^* \frac{\partial u^*}{\partial y^*} + w^* \frac{\partial u^*}{\partial z^*} = -\frac{\partial P^*}{\partial x^*} + \frac{\mu}{\rho V_\infty D}\left[\left(\frac{\partial^2 u^*}{\partial x^{*2}}\right) + \left(\frac{\partial^2 u^*}{\partial y^{*2}}\right) + \left(\frac{\partial^2 u^*}{\partial z^{*2}}\right)\right] \tag{3.12a}$$

Y-momentum Equation:

$$u^* \frac{\partial v^*}{\partial x^*} + v^* \frac{\partial v^*}{\partial y^*} + w^* \frac{\partial v^*}{\partial z^*} = -\frac{\partial P^*}{\partial y^*} + \frac{\mu}{\rho V_\infty D}\left[\left(\frac{\partial^2 v^*}{\partial x^{*2}}\right) + \left(\frac{\partial^2 v^*}{\partial y^{*2}}\right) + \left(\frac{\partial^2 v^*}{\partial z^{*2}}\right)\right] - \frac{gD(1 - \rho_{rc}}{V_\infty^2} \tag{3.12b}$$

Z-momentum Equation:

$$u^* \frac{\partial w^*}{\partial x^*} + v^* \frac{\partial w^*}{\partial y^*} + w^* \frac{\partial w^*}{\partial z^*} = -\frac{\partial P^*}{\partial z^*} + \frac{\mu}{\rho V_\infty D}\left[\left(\frac{\partial^2 w^*}{\partial x^{*2}}\right) + \left(\frac{\partial^2 w^*}{\partial y^{*2}}\right) + \left(\frac{\partial^2 w^*}{\partial z^{*2}}\right)\right] \tag{3.12c}$$

Energy Equation:

$$u^* \frac{\partial T^*}{\partial x^*} + v^* \frac{\partial T^*}{\partial y^*} + w^* \frac{\partial T^*}{\partial z^*} = \frac{k}{\rho Cp V_\infty D}\left[\left(\frac{\partial^2 T^*}{\partial x^{*2}}\right) + \left(\frac{\partial^2 T^*}{\partial y^{*2}}\right) + \left(\frac{\partial^2 T^*}{\partial z^{*2}}\right)\right] - \frac{h_{fg}}{Cp \nabla T}\left[\left(\frac{\partial f^*}{\partial x^*}\right) + \left(\frac{\partial f^*}{\partial y^*}\right) + \left(\frac{\partial f^*}{\partial z^*}\right)\right] \tag{3.13}$$

From equations 3.12 and 3.13 the following dimensionless terms or coefficients can be extracted.

$$\frac{\mu}{\rho V_\infty D} \qquad \frac{gD}{V_\infty^2} \qquad \frac{k}{\rho C p V_\infty D} \qquad \frac{h_{fg}}{C p \nabla T}$$

The boundary condition equations in scaled form are also presented as equations 3.14 - 3.17.

$$\left. V^* \right|_{y^*=0} = 0 \tag{3.14}$$

$$\frac{\dot{\mathbf{q}} \cdot D}{k_f (T_s - T_l)} = \frac{\rho_l h_{fg} V_n D}{k_f (T_s - T_l)} - \left. \frac{\partial T^*}{\partial y^*} \right|_{y^*=0} \tag{3.15}$$

$$\frac{\rho_l \cdot h_{fg} \mathbf{V_n} \cdot D}{k_l (T_s - T_l)} = \left. \frac{\partial T_l^*}{\partial y^*} \right|_{y^*=y_{\text{int}}} - \frac{k_g}{k_l} \left. \frac{\partial T_g^*}{\partial y^*} \right|_{y^*=y_{\text{int}}} \tag{3.16}$$

$$\rho \cdot V_\infty^2 \cdot D^2 = \sigma \cdot D \tag{3.17}$$

Rearranging the dimensionless terms in the three conservative equations (mass, momentum and energy) as well as the boundary conditions, the following dimensionless parameters are obtained.

$$\mathrm{Re}_D = \frac{\rho V_\infty D}{\mu} \qquad Fr = \frac{V_\infty}{\sqrt{gD}} \qquad \mathrm{Pr} = \frac{\mu C_p}{k} \qquad Ja = \frac{C_p \nabla T}{h_{fg}}$$

$$Nu_{\text{mod}} = \frac{\dot{\mathrm{q}} \cdot D}{k_f (T_s - T_l)} \qquad We = \frac{\rho \cdot V_\infty^2 \cdot D}{\sigma} \qquad Bo = \frac{g \cdot \Delta\rho \cdot L_c^2}{\sigma} \qquad P_{ratio} = \frac{P_i}{P_l}$$

The dimensionless numbers and/or parameters which have been obtained from the scaled equations are further explained in the following section.

The scaled equations 3.11, 3.12 and 3.13 are recast with the dimensionless parameters. Equations 3.18 and 3.19 are the momentum and energy equations with the dimensionless parameters obtained after the scaling analysis.

X-Momentum:

$$u^* \frac{\partial u^*}{\partial x^*} + v^* \frac{\partial u^*}{\partial y^*} + w^* \frac{\partial u^*}{\partial z^*} = -\frac{\partial P^*}{\partial x^*} + \frac{1}{\mathrm{Re}_D}\left[\left(\frac{\partial^2 u^*}{\partial x^{*2}}\right) + \left(\frac{\partial^2 u^*}{\partial y^{*2}}\right) + \left(\frac{\partial^2 u^*}{\partial z^{*2}}\right)\right] \quad \textbf{(3.18a)}$$

Y-Momentum:

$$u^* \frac{\partial v^*}{\partial x^*} + v^* \frac{\partial v^*}{\partial y^*} + w^* \frac{\partial v^*}{\partial y^*} = -\frac{\partial P^*}{\partial y^*} + \frac{1}{\mathrm{Re}_D}\left[\left(\frac{\partial^2 v^*}{\partial x^{*2}}\right) + \left(\frac{\partial^2 v^*}{\partial y^{*2}}\right) + \left(\frac{\partial^2 v^*}{\partial z^{*2}}\right)\right] - \frac{(1-\rho_{rat})}{Fr^2} \quad \textbf{(3.18b)}$$

Z-momentum:

$$u^* \frac{\partial w^*}{\partial x^*} + v^* \frac{\partial w^*}{\partial y^*} + w^* \frac{\partial w^*}{\partial y^*} = -\frac{\partial P^*}{\partial z^*} + \frac{1}{\mathrm{Re}_D}\left[\left(\frac{\partial^2 w^*}{\partial x^{*2}}\right) + \left(\frac{\partial^2 w^*}{\partial y^{*2}}\right) + \left(\frac{\partial^2 w^*}{\partial z^{*2}}\right)\right] \quad \textbf{(3.18c)}$$

Energy:

$$u^* \frac{\partial T^*}{\partial x^*} + v^* \frac{\partial T^*}{\partial y^*} + w^* \frac{\partial T^*}{\partial z^*} = \frac{1}{\mathrm{Pr}\,\mathrm{Re}_D}\left[\left(\frac{\partial^2 T^*}{\partial x^{*2}}\right) + \left(\frac{\partial^2 T^*}{\partial y^{*2}}\right) + \left(\frac{\partial^2 T^*}{\partial z^{*2}}\right)\right] - \frac{1}{Ja}\left[\left(\frac{\partial f^*}{\partial x^*}\right) + \left(\frac{\partial f^*}{\partial y^*}\right) + \left(\frac{\partial f^*}{\partial z^*}\right)\right] \quad \textbf{(3.19)}$$

The experimental matrix and parametric study for the present research work were formulated based on the obtained dimensionless numbers. Specific dimensionless numbers which are desired for high heat fluxes are low Jacob number (Ja <1) and high Nusselt number (Nu>>1). The fluid transport properties which were used to calculate the dimensionless numbers were obtained during preliminary experimental test runs. Water and Novec 7000 are used as the working fluids in all experiments for this research work. The dimensionless parameter range for the experiments was therefore based on water and Novec 7000 fluid. Table 3.1 presents the specific dimensionless parameters which were obtained after scaling analysis.

Table 3.1. Dimensionless parameters in phase change fluid transport

Dimensionless numbers	**Variables**
Reynolds number (Re)	$\mathrm{Re}_D = \dfrac{\rho V_\infty D}{\mu}$
Froude number (Fr)	$Fr = \dfrac{V_\infty}{\sqrt{gD}}$
Prandtl number (Pr)	$\mathrm{Pr} = \dfrac{\mu C_p}{k}$
Jacob number (Ja)	$Ja = \dfrac{C_p \nabla T}{h_{fg}}$
Modified Nusselt (Nu)	$Nu_{\mathrm{mod}} = \dfrac{\dot{\mathrm{q}} \cdot D}{k_f (T_s - T_l)}$
Peclet number (Pe)	$Pe = \mathrm{Re}_D \cdot \mathrm{Pr}$
Weber number (We)	$We = \dfrac{\rho \cdot V_\infty^2 \cdot D}{\sigma}$
Bond number (Bo)	$Bo = \dfrac{g \cdot \Delta\rho \cdot L_c^2}{\sigma}$
Property ratios	$P_{rat} = \dfrac{P_i}{P_l}$
Diffusivity term	$\dfrac{1}{\mathrm{Ja}} \left(\dfrac{\mathrm{V_n} D}{\alpha_l} \right)$

The working fluids, test surface and spray conditions have been developed to obtain the desired dimensionless numbers. Table 3.2 presents the thermophysical properties of the working fluids which were used in the spray cooling experiments.

Table 3.2. Thermophysical properties of water and Novec 7000

Thermophysical Property	Water	Novec 7000
Boiling point (^{o}C) @ 1 atm	100.000	34.000
Liquid density (kg/m3)	1000.000	1400.000
Critical pressure (MPa)	22.100	2.480
Critical temperature (oC)	386.000	165.000
Latent heat of vaporization (kJ/kg)	2270.000	142.000
Specific heat (kJ/kg-K)	4.187	1.300
Surface tension (N/m)	0.073	0.012
Thermal conductivity (W/m-K)	0.596	0.075
Viscosity (kg/m-s)	0.001	0.0005

The range of the desired dimensionless parameters has been used to develop the experimental matrix for this research work. Table 3.3 presents the range of some of the dimensionless numbers which were obtained with water and Novec 7000 as the working fluids. The dimensionless parameters are balanced so as to maximize the heat transfer performance during the experiments. The following section presents the specific experimental setups used to obtain the data for the present research work.

Table 3. 3. Range of dimensionless numbers

Dimensionless numbers	**Water**	**Novec 7000**
Reynolds number (Re)	560.29 - 7470.59	1702.34 - 22697.87
Prandtl number (Pr)	7.17	8.15
Jacob number (Ja)	0.15	0.14
Bond number (Bo)	0.03	0.28
Peclet number (Pe)	4014.88 - 53531.78	13868.40 - 184912.00
Weber number (We)	0.12 - 20.93	0.97 - 72.06

3.2 Experimental Setup

A thermal loop which operates on two-phase fluid flow has been constructed for the present study. The experimental setup consists of a fluid management system and a heater chamber that houses the test substrate. The working fluid is circulated in the loop using a two-phase centrifugal pump. Power to the test substrate is supplied by a voltage supply. The heater chamber that houses the test substrate has a glass window that allows visualization into the heater chamber during the spray cooling experiments. The thermal loop has been instrumented to obtain data for pressure, temperature, vapor quality and flow rates during experimentation. In addition, high speed video camera has been incorporated with the experimental setup to obtain data on the impacting fluid dynamics upon fluid spray on the test surface. Detail description of the specific experimental setups is presented in the following sections. Figure 3.2 below shows the schematic of the two-phase closed loop used for the experimental investigations.

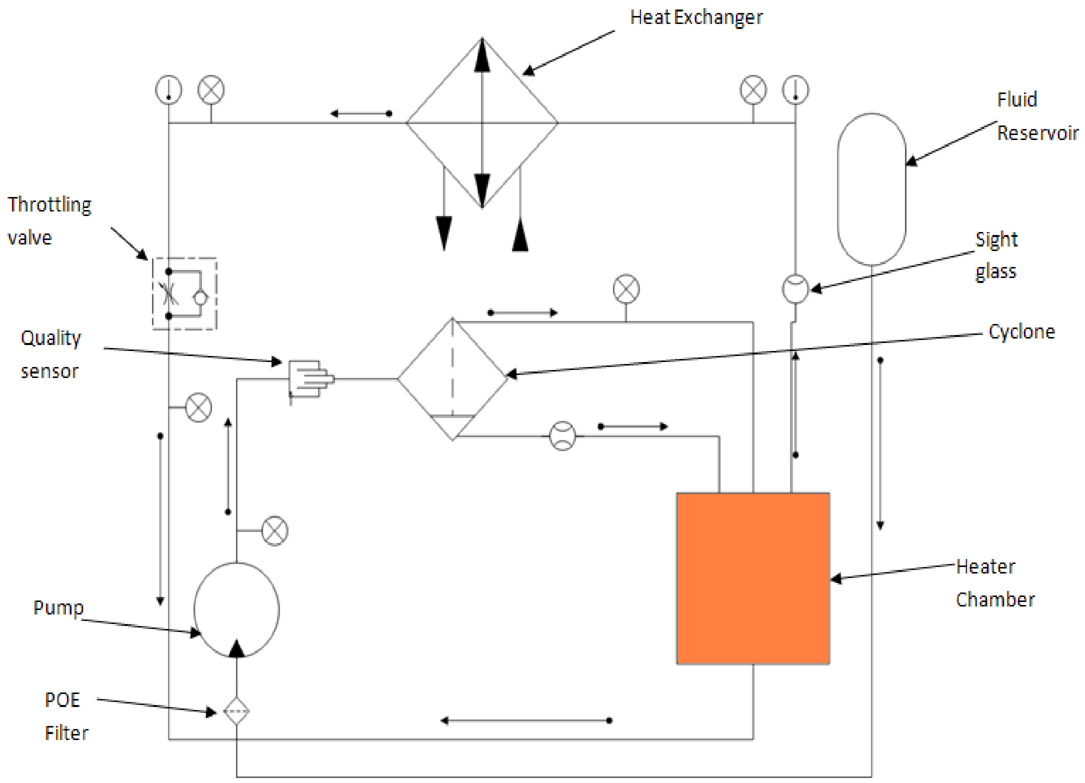

Figure 3.2. Schematic drawing of two phase thermal loop

The thermal loop operates on a two-phase fluid flow. A 2.64 kW (with 2.4 Liter/min flow rate) counter flow arrangement tube-in-tube heat exchanger is used to control the vapor quality in the fluid flow. A liquid-vapor mixture is throttled from the heat exchanger to a two-phase centrifugal pump through a one-way throttling valve. The fluid mixture is then pumped into a cyclone where the vapor stream is separated from the liquid stream by centrifugal forces. The vapor line is re-connected to the liquid stream to atomize the liquid at the entry of the spray nozzle. Fine fluid droplets (spray) produced is impinged on the heated test surface. The vapor produced due to phase change of the liquid spray upon impingement on the heated surface expands into the heat exchanger. Excess liquid (fluid) on the test surface inside the heater chamber is drained and reconnected to fluid mixture from the throttling valve at the entry of the centrifugal pump. The vapor to the heat exchanger is cooled back down into a liquid-vapor mixture and the process is repeated for the cycle. A reservoir has been incorporated into the loop for fluid supply during shortages and high fluid demand. The major components of the thermal loop are presented in the following section.

3.2.1 Major Components of the Closed Thermal Loop

The thermal loop shown in Figure 3.2 above has been constructed to operate on a two-phase fluid flow. The major components of the thermal loop connected with half inch copper tubing are:

a. Heat Exchanger (2.64 kW counter-flow arrangement tube-in-tube exchanger)
b. Pump (18.92 L/min rotary pump with 1/6 horse power motor)
c. Valves (One-way valves and four-ports-three-connections valves)
d. Cyclone
e. Heater Chamber (contains test specimen and nozzle for fluid spray)
f. Reservoir
g. Vacuum Pump
h. POE Oil Filter

Figure 3.3 below shows the connections of the components of the thermal loop.

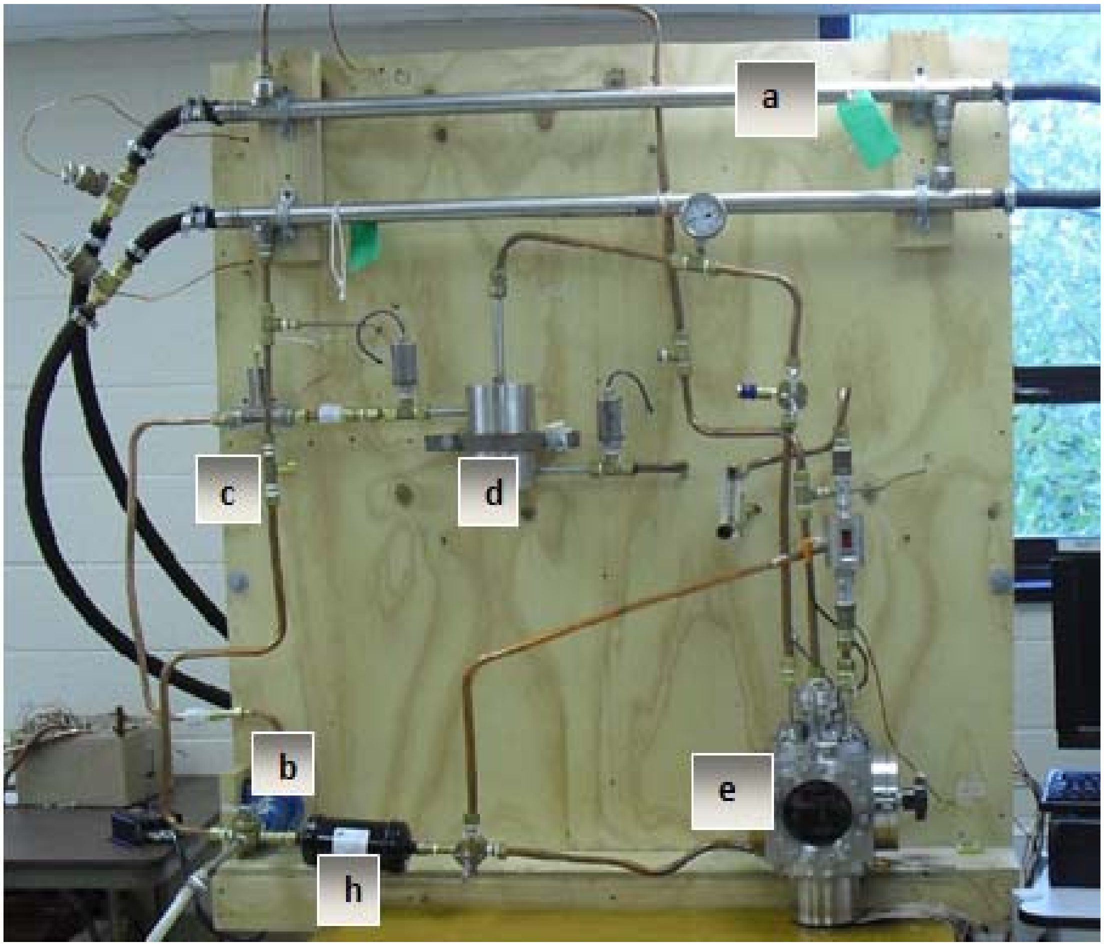

Figure 3.3. Two phase thermal loop

3.2.2 Measuring Instruments

Temperature, pressure, flow rates and vapor quality are the main variables measured for the experimental investigations. The measurement instruments are connected to an IOtech 6000 series scanner for data acquisition. Pressure transducers for measurement of pressure were calibrated a priori to installation on the thermal loop. Table 3.2 presents the specific instruments used for each measured variable.

Table 3.4. Measuring Instruments

Variable	Instrument
Temperature	K-type thermocouple
Vapor quality	Void-fraction sensor
Flow rates	Flow meter
Pressure	PX 303A Pressure transducers

3.2.3 Data Acquisition System (DAQ)

An IOtech 6000 series DAQ (obtained from Measurement Computing Corporation, 10 Commerce Way Norton MA 02766, USA) is used to collect the data measured. The different data variables were recorded at the appropriate frequencies between 1-100 kHz. The data collected are stored on a computer system using IOtech Encore software that communicates between the DAQ and the computer CPU. Figure 3.4 shows the IOtech DAQ system used for the data acquisition of all the measured data.

Figure 3.4. IOtech Data Acquisition system

3.3 Heat Flux Measurement

Heat flux measurements are carried out on test substrate (copper heater) during the run of the two-phase thermal loop. A power supply (Agilent 6030A with specifications of 0~200 Volts; 0~17 Ampere) is used to provide power to the test specimen. The heat flux at each power setting is obtained by dividing the wattage (power) by the surface area of the test specimen. Heat losses are accounted for in each heat flux measurement. Steady state condition is ensured at each power setting during the cooling process with fluid spray impingement on the test surface. K-type thermocouples are used to measure the temperature of the surface of the test specimen and the temperature distribution along the crown of the test specimen to check for steady state conditions. The test specimen is enveloped in an air tight heater chamber. Figure 3.5 shows fluid spray impingement on the surface of the test substrate inside the heater chamber.

Figure 3.5. Fluid impingement on a test surface

The heater chamber as shown in Figure 3.5 has a glass window that allows for visualization of the fluid spray upon impingement on the heated test surface. The fluid spray is produced by an ultra-fine spray nozzle. Different nozzle orifice sizes and spray angles were used depending on the size of the test specimen. The spray nozzle tip-to-surface distance was also adjusted in each experiment for optimal fluid coverage on the test surface. Specific nozzle orifice sizes, spray angles and nozzle offset distances are reported in the data analysis section in Chapter 4.

Power to the test specimen provided by the Agilent 6030A voltage supply (Agilent Technologies, 5301 Stevens Creek Blvd, CA 95051, USA) is programmed at voltage increment of 10 volts. At each voltage, the corresponding current is recorded and the power output is determined. Steady-state condition is ensured with the spray cooling process at each voltage setting. Figure 3.6 shows the front and rear view of the Agilent 6030A programmable power supply.

Figure 3.6. Agilent 6030A programmable power supply (front and rear view)

The test specimen is made of ultra conductive copper material (Alloy 101), with holes along the crown to accommodate K-type thermocouples for temperature measurement. Thin film resistive heaters or heater catridges are used to heat the test specimen. The test specimen is insulated using a glass mica and utral high temperature strip made of ceramic material. Figure 3.7 shows the schematic of the heater specimen.

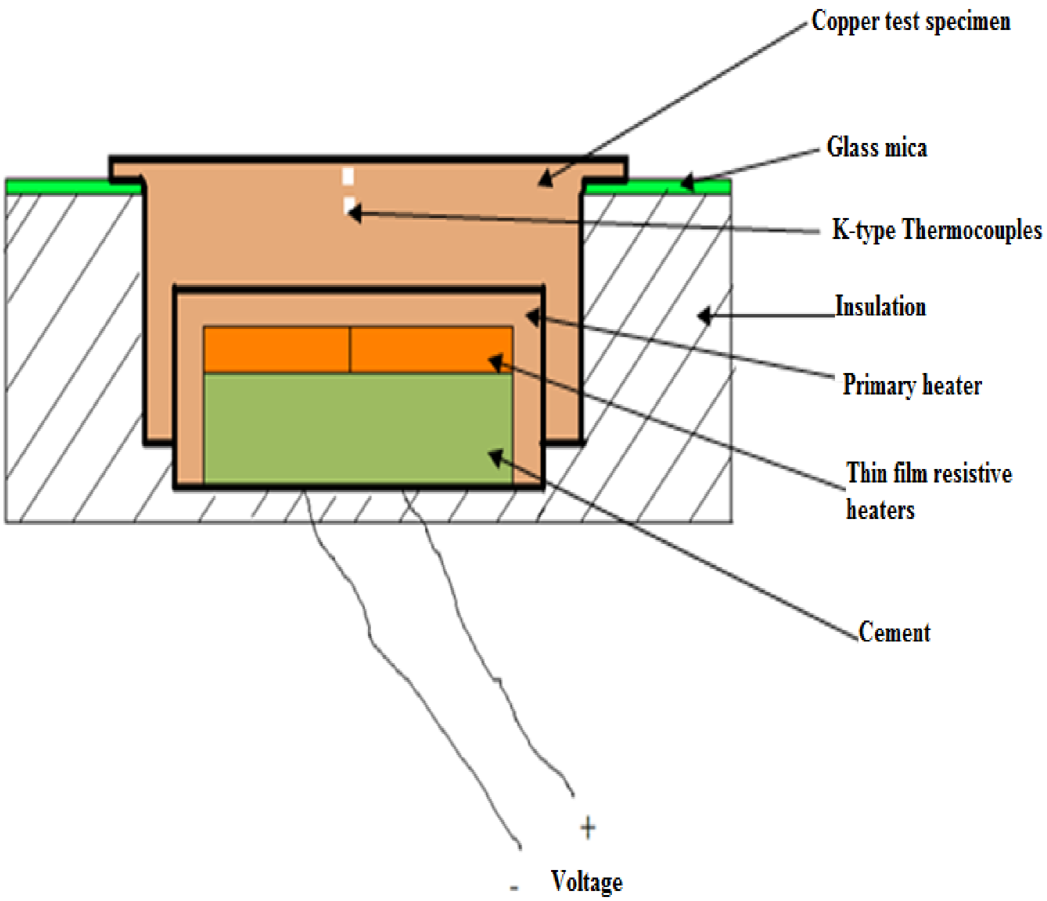

Figure 3.7. Schematic of test specimen with thin film resistive heaters

Figure 3.8 below shows the assembly process of sample test specimen with the thin film resistive heaters. The thin film resistive heaters are embedded in the primary heater and supported by a cement. Four of 250 Watts thin film resistive heaters were used in this specific specimen assembly to produce a 1kW heater specimen.

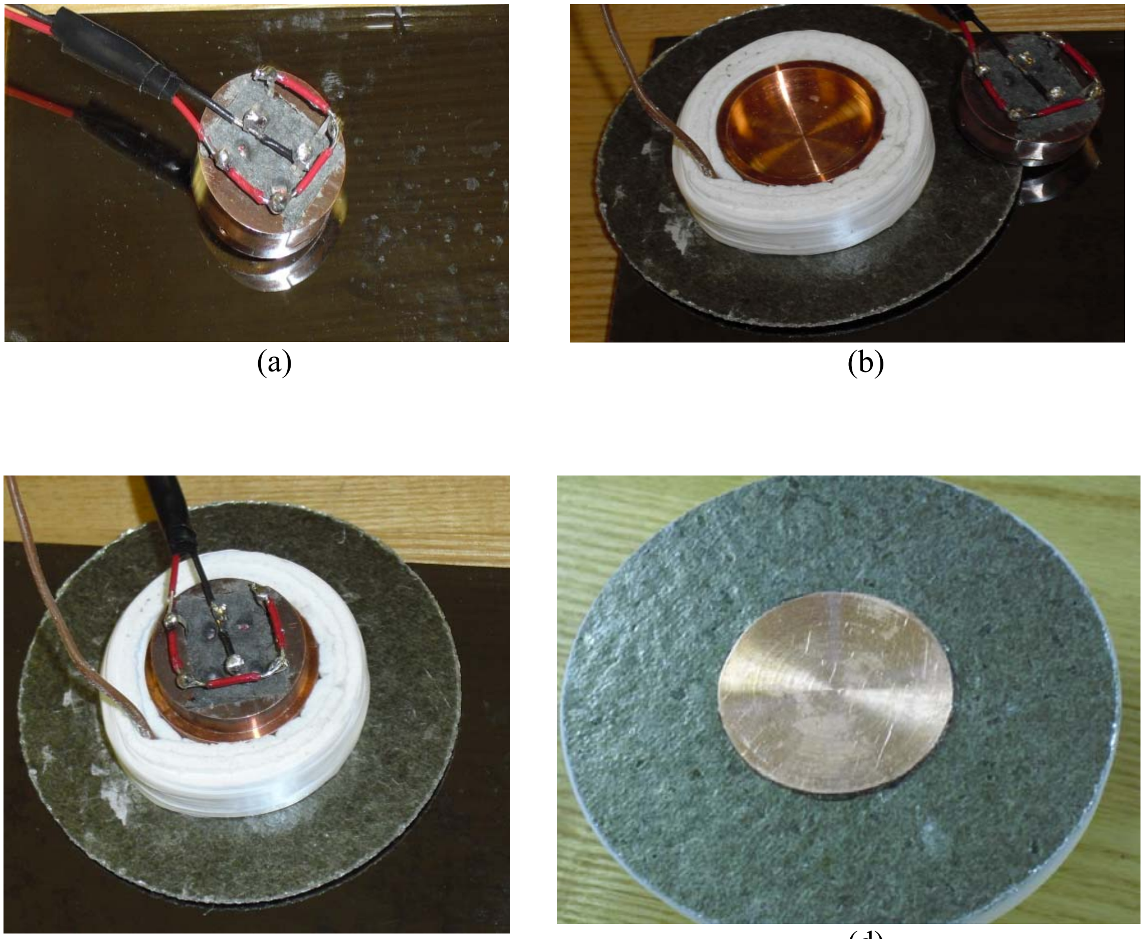

(a) (b)

(c) (d)

Figure 3.8. Assembly of 1kW heater specimen: (a) primary heater element, (b) insulation of test specimen, (c) assembled specimen with K - type thermocouple and (d) completed specimen showing the top surface

Experiments were conducted on both smooth and modified or enhanced surfaces. The enhanced surfaces were produced based on the analytical considerations for fluid wicking on the surface. The wicking phenomenon and enhanced heat transfer mechanism due to the modified surfaces are presented in this document. The modification of the surfaces were in the form of grooves with different sizes and angles. Figure 3.9 shows samples of both smooth and modified surfaces which were tested in the spray cooling experiments.

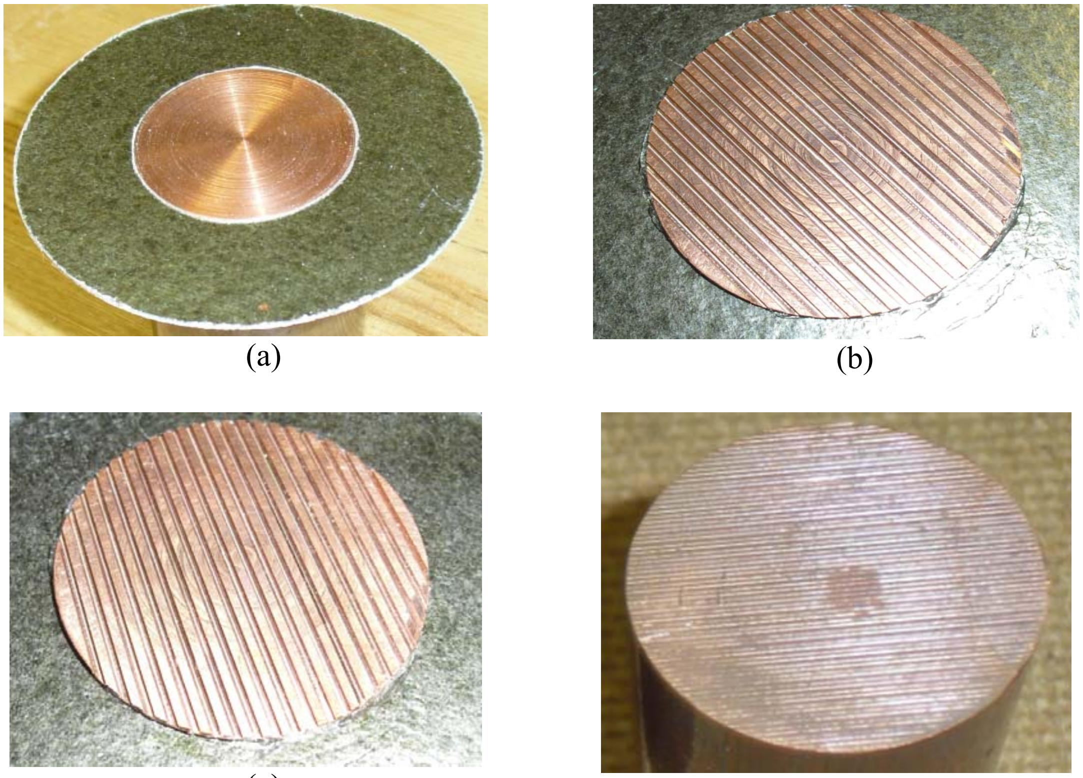
(a) (b)

(c) (d)

Figure 3.9. Samples of smooth and modified surfaces: (a) smooth surface, (b) 1.27 mm groove surface, (c) 2.03 mm groove surface and (d) 0.06 mm groove surface

Specimen of different area sizes were also prepared for heat flux experimentation. The test substrate area sizes were determined based on the spray profile and spray impact area which were obtained in a bench test of the spray nozzles. Figure 3.10 shows the schematic of the nozzle spray profile and how the test surface area sizes (A1, A2, A3 and A4) were selected.

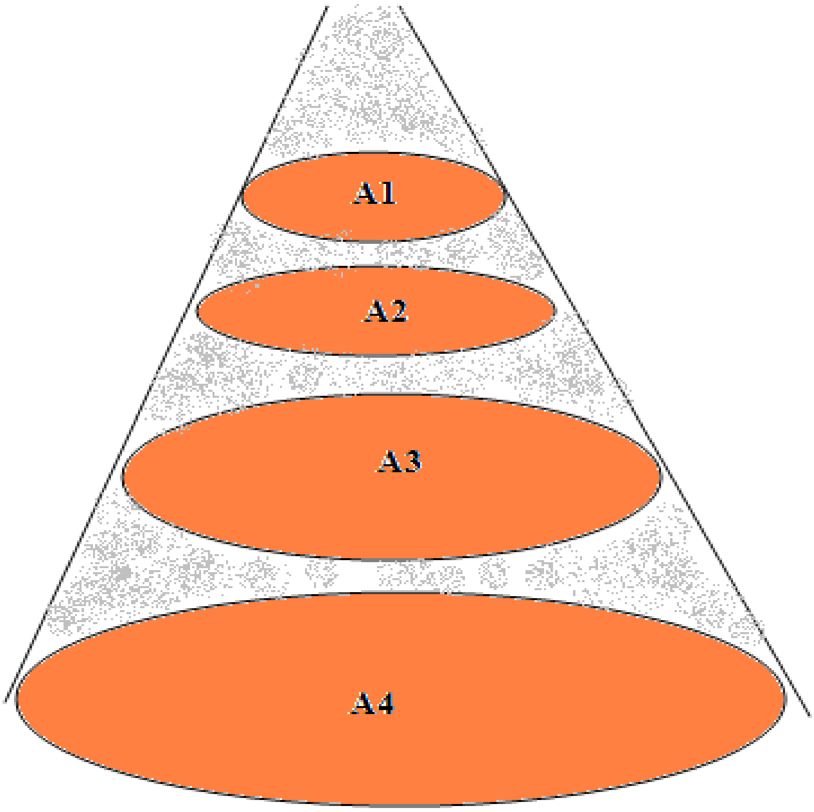

Figure 3.10. Spray profile and substrate area determination

The optimal spray profile as shown in Figure 3.10 was obtained at fixed flow rate and spray pressure as indicated by the manufacturer of the spray nozzle. The substrate surface area sizes were determined based on the cross section of the spray profile at different levels along the spray. Specific test substrates with diameters of the top surface of 1.00 inch, 1.25 inches, 1.50 inches and 2.00 inches were prepared. The converted surface areas are 5.07 cm^2; 7.92 cm^2; 11.40 and 20.27 cm^2 respectively. Figure 3.11 schematically shows the different area sizes with the corresponding diameters in inches.

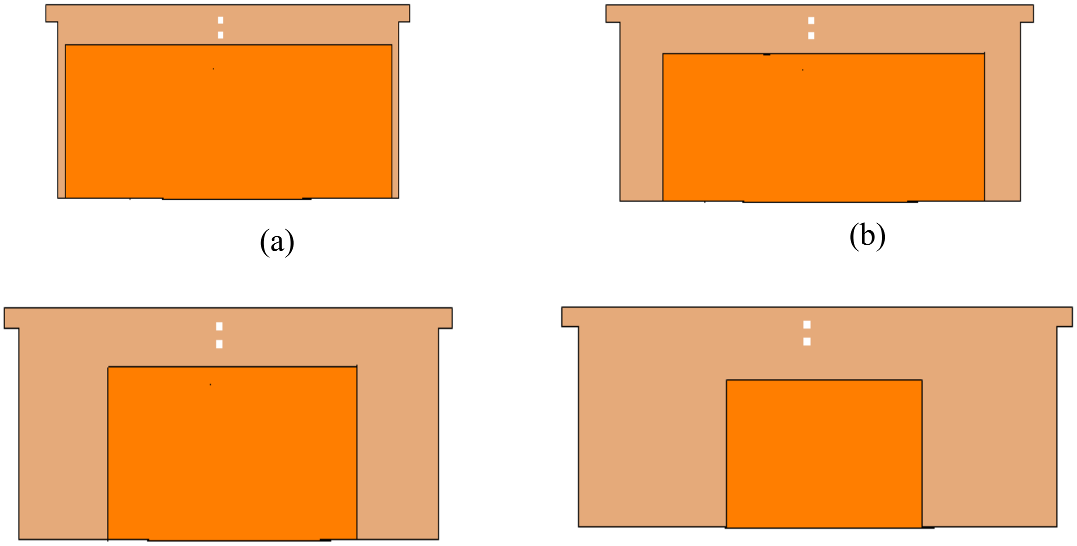

(a) (b)

(c) (d)

Figure 3.11. Schematic of different area sizes tested in heat flux experiments: (a) top surface area of 5.07 cm^2, (b) top surface area of 7.92 cm^2, (c) top surface area of 11.40 cm^2 and (d) top surface area of 20.27 cm^2

The experimental and specimen setups were prepared to meet the specific objective of this work. The parametric studies for the present research work are presented in the following section.

3.4 Parametric Study

An experimental matrix has been developed for parametric studies based on the specific objectives presented in Chapter 1. The parameters are studied to determine their effects on critical heat flux and heat transfer coefficient in spray cooling experiments. In addition, the heat transfer regime of spray cooling is studied. The experimental test conditions for each parametric study are reported in the results and discussion section in Chapter 4. The specific parameters studied to determine their effects on critical heat flux and heat transfer coefficient are presented in the following sections.

3.4.1 Test Surface Area Scalability and Critical Heat Flux (CHF)

Different surface area sizes of test substrate were tested in a spray cooling experiment using the two phase thermal loop that has been developed. Specific test substrates with diameters of the top surface of 1.00 inch, 1.25 inches, 1.50 inches and 2.00 inches were tested. The converted surface area sizes tested are: 5.07 cm^2; 7.92 cm^2, 11.40 cm^2 and 20.27 cm^2. In each experimental test of the substrate, the working fluid flow rate is controlled to obtain optimal fluid coverage on the test surface. Excess liquid fluid on the surface of the test substrate is avoided by optimally controlling the flow rate of the working fluid. The specific flow rates of the working fluid during the experiments are presented in the data analysis section in Chapter 4. The effect of test surface area scale-ups on the critical heat flux and heat transfer coefficient is determined and the results are presented in Chapter 4.

3.4.2 Test Surface Modifications and Heat Transfer Performance

Different modified surfaces are also tested and their effects on heat flux and heat transfer coefficient are determined. Table 3.6 shows the specific modified structures developed on the surface of the test substrates.

Table 3.5. Modified surfaces tested

Surface	Modified structure type	Groove size (μm x μm)
Surface 1	90^o grooves	60 x 60
Surface 2	90^o grooves	1270 x 1270
Surface 3	90^o grooves	2030 x 2030
Surface 4	60^o grooves	1270 x 1270

The modified structures on the surface of the test substrate have been developed to obtain fluid wicking on test surface. The capillary wicking phenomenon on the modified surface is based on the Concus-Finn condition. The Concus-Finn condition is formulated based on the half-corner angle of the modified groove and the solid contact angle at which the wicking fluid substends with the surface. In addition, low Bond number effects have been considered for the fluid wicking on the test surface. Figure 3.12 shows the capillary wicking phenomenon of the fluid on the modified test surface with half corner angle of the groove (α) and the solid contact angle (θ) of the wicking fluid with the surface.

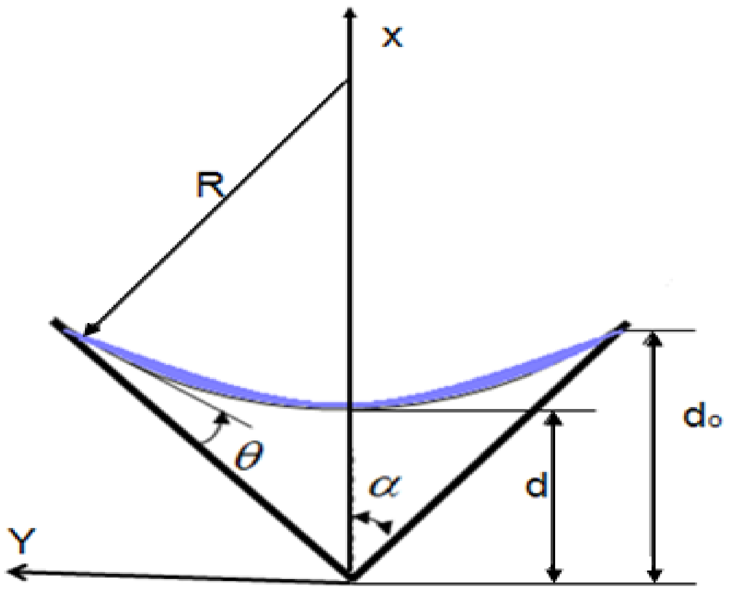

Figure 3.12. Wicking surface with half-corner and solid contact angles

From Figure 3.12, R, d and d_o are the radius of curvature, lower and upper meniscus of the wicking fluid respectively. The Concus-Finn condition is satisfied such that the half corner angle of the groove (α) and the solid contact angle (θ) of the wicking fluid with the surface meets the criteria: $\alpha < \frac{\pi}{2} - \theta$. In addition, the wicking grooves are designed such that low Bond numbers (Bo< 1) are obatined. The characteristic groove length is therefore designed according to equation 3.20 presented below.

$$0.32\sqrt{\frac{\sigma}{g\,\Delta\rho}} < L_g < \sqrt{\frac{\sigma}{g\,\Delta\rho}} \tag{3.20}$$

In analyzing unidirectional grooves akin to corner flows in complex geometry, the Young-Laplace curvature formulation is used to compute for the capillary pressure difference across the interface. Thus, an interfacial capillary pressure difference is defined as: $\Delta P = \frac{2\sigma}{R}$. From the wicking groove geometry as shown in Figure 3.12, the local radius of curvature is defined by Equation 3.21.

$$R = \frac{d\left(Cos\,\theta - Sin\,\alpha\right)}{Sin\,\alpha} \qquad \textbf{(3.21)}$$

The wicking phenomenon in the grooves has been analyzed using the mass and momentum equations (Equations 3.1 and 3.2) which are presented in the previous section. Based on the work of (Allen, 2003), the mass amd momentum equations are presented in dimensionless form as Equations 3.22 and 3.23 respectively.

$$\frac{\partial(\eta^2)}{\partial\tau} = \frac{\partial}{\partial\zeta}\left[\left\langle\tilde{w}\right\rangle\eta^2\right] \qquad \textbf{(3.22)}$$

$$\frac{\partial\tilde{p}}{\partial\zeta} = \frac{\partial^2\tilde{w}}{\partial\xi^2} + \frac{1}{\tan^2\alpha}\frac{\partial^2\tilde{w}}{\partial\xi^2} \qquad \textbf{(3.23)}$$

A flow coefficient (F) is defined such that $\left\langle\tilde{w}\right\rangle = F\frac{\partial\eta}{\partial\zeta}$.

The dimensionless variables which were used to obtain Equations 3.22 and 3.23 are:

$$\zeta = \frac{z}{L} \qquad \tilde{w} = \frac{w}{W} \qquad \tau = \frac{Wt}{L} \qquad \xi = \frac{x}{d_o} \qquad \eta = \frac{d}{d_o}$$

From the scaling parameters, w is the wicking velocity and L is the length of the groove. The dimensionless Equations 3.22 and 3.23 are reconstructed in dimensional form for steady flow conditions and combined with Equation 3.21 to obtain the wicking velocity of the fluid inside the groove. The wicking velocity is therefore determined and presented as Equation 3.24 with the aspect ratio $e = \frac{d_o}{L}$.

$$w = \frac{e\,F\sigma\,Sin^3(\alpha)(1-\eta^3)}{3\mu(\cos\theta - \sin\alpha)} \tag{3.24}$$

Equation 3.24 has been solved numerically to obtain the effect of the half corner angle on the wicking velocity for different fluids at specific solid contact angles. The solution obtained is presented in the results and discussion section in Chapter 4.

3.4.3 Heat Flux Regimes in a Spray Cooling Experiment

A high speed video camera and image processing system and/or software have been used to visually observe the fluid-surface interactions upon fluid spray impingement on the heated surface in a spray cooling experiment. The recorded images are analyzed to determine the fluid physics in the various heat flux regimes in spray cooling experiment. Figure 3.13 shows the setup for recording the video and the data during the spray cooling experiments.

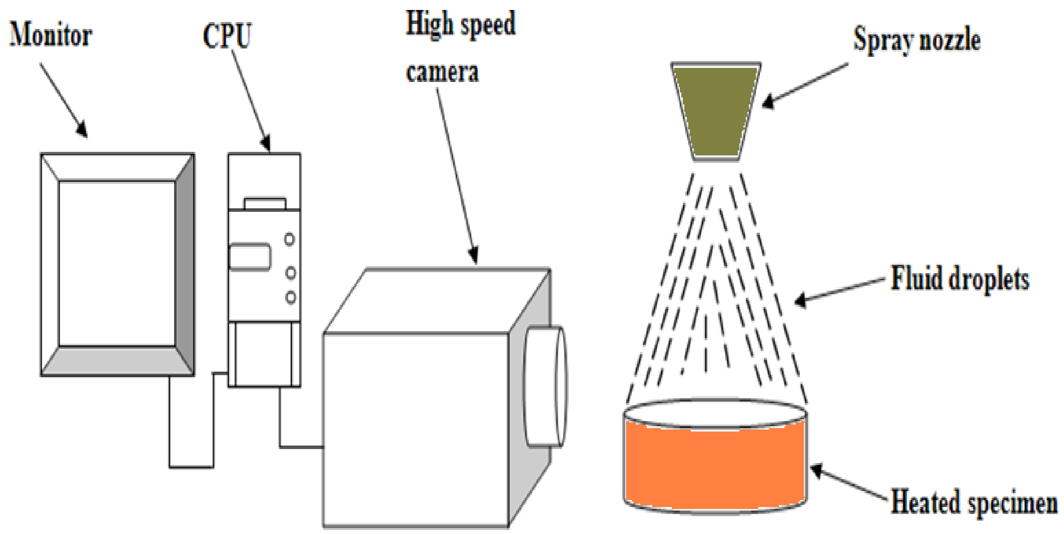

Figure 3.13. Setup for live video image recordings

The video images were taken using the high speed camera set at 10,000 frames per second (fps). The high speed video camera was set at 10,000 fps to resolve the time scales in magnitude of 0.1 milliseconds which are associated with bubble generation and rupture. The images were analyzed using Photron FastCam Viewer (PFV) software. The live video images were recorded at different times during the experiment, being: non-boiling regime, phase change regime and the incipience of critical heat flux regime.

3.4.4 Liquid Film Thickness on Heat Transfer Performance

The flow rate of the working fluid is controlled to maintain thin liquid film on the heated surface. Liquid film development on the test surfaces is studied to determine its effect on the heat transfer performance. Figure 3.14 shows a schematic of thin liquid film flow over an inclined heated flat surface.

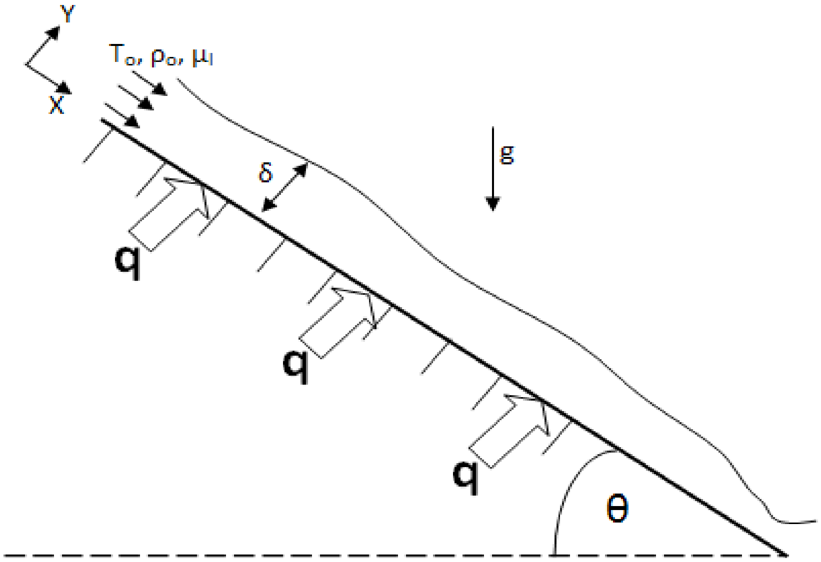

Figure 3.14. Model representation of liquid flow on an inclined heated plate

From Figure 3.14, the surface of the test substrate is subjected to a constant heat flux (q), with flowing liquid free-stream conditions (T_o, ρ_o, μ_l) on the surface. The plate is inclined at an angle, θ. The thickness of the liquid film on the surface is δ. The conservative laws describing the fluid transport properties and heat transfer presented above have been applied to the underlying problem with a 2-D formulation. The specific boundary conditions applied for the analyses are presented as:

1. No slip condition at the wall: $u(y=0) = v(y=0) = 0$
2. No penetration effects: $v(x, y) = 0$
3. Velocity boundary layer approximations: $\dfrac{\partial u}{\partial y} >> \dfrac{\partial u}{\partial x}$; $\dfrac{\partial^2 u}{\partial y^2} >> \dfrac{\partial^2 u}{\partial x^2}$
4. The body force in x-momentum equation for an inclined place: $\rho g \sin(\theta)$
5. Viscous dissipation term negligible: $\mu \Phi = 0$
6. Constant fluid properties except density which depends on temperature
7. No heat generation inside the fluid: $Q_{gen} = 0$
8. Thermal boundary layer approximations: $\dfrac{\partial T}{\partial y} >> \dfrac{\partial T}{\partial x}$; $\dfrac{\partial^2 T}{\partial y^2} >> \dfrac{\partial^2 T}{\partial x^2}$
9. Phase change at the liquid vapor inter-phase is by latent energy:

   $$q(y=\delta) = \rho_l h_{fg} V_n$$
10. Heat flux at the wall:

    $$q = -k \left.\frac{\partial T}{\partial y}\right|_{y=0}$$

With the above assumptions and the boundary layer approximation for the pressure gradient $\frac{\partial P}{\partial x} = \rho_v\, g$; the velocity profile for liquid film thickness (δ) is thus obtained as:

$$u(y) = \frac{g(\rho \sin(\theta) - \rho_v) y \delta}{\mu_l}\left[1 - \frac{y}{2\delta}\right] \tag{3.25}$$

The mean velocity of the falling liquid film is obtained by integration of the velocity profile over the film thickness (δ). The mean film velocity is presented as Equation 3.26 below:

$$U_m = \frac{g(\rho \sin(\theta) - \rho_v)\delta^2}{3\mu_l} \tag{3.26}$$

Using Boussinesq approximation for density dependence on temperature for an evaporating film, a temperature function is obtained as:

$$T = \left[\frac{1}{\beta}\left(1 - \frac{1}{r\sin(\theta)}\left\{\frac{3\mu_l\, U_m}{g\,\delta^2 \rho_v} + 1\right\}\right) + T_o\right] \tag{3.27}$$

where: $r = \frac{\rho_o}{\rho_v}$, *density ratio*

Combining the latent energy term and the sensible energy using the temperature function for the thin liquid film evaporation, the total heat flux is obtained as Equation 3.28.

$$q = -\frac{k_l}{\delta}\left[\left(T_s - T_o\right) - \frac{1}{\beta}\left(1 - \frac{1}{r\sin\theta}\left\{\frac{3\mu_l\, U_m}{g\,\delta^2 \rho_v} + 1\right\}\right)\right] + \rho_l\, h_{fg}\, V_n \tag{3.28}$$

The heat flux is therefore determined to be inversely proportional to the cube of the liquid film thickness. Equation 3.28 is solved numerically and the result is presented in the data analysis section of Chapter 4. Prior to the spray cooling experiments based on the parameters to be studied, preliminary experiments and numerical simulations were conducted. The section below presents the preliminary results.

3.5 Preliminary Experiments and Numerical Simulations

Nucleate pool boiling experiments have been conducted on Novec 7000 fluid. Numerical simulations on heat conduction through the test substrates have also been conducted. The results from the preliminary experiments and numerical simulations are presented below

3.5.1 Nucleate Pool Boiling Experiments

Boiling curves have been determined for Novec 7000 fluid using Hilton Boiling Heat Transfer Unit (H655). For the purpose of comparison, boiling curve for R 141b (1,1-dichloro-1-fluoroethane) has also been obtained. The thermophysical properties of Novec 7000 fluid and R 141b fluid are presented in Table 3.6.

Table 3.6. Thermophysical properties for Novec 7000 and R 141b fluids

Thermophysical Property	R 141b	Novec 7000
Boiling point (^oC) @ 1 atm	32.0	34.0
Critical temperature (^oC)	205.0	165.0
Latent heat of vaporization (kJ/kg)	223.0	142.0
Specific heat (J/kg-K)	1,160.0	1,300.0

The section below presents nucleate pool boiling experiments on Novec 7000 fluid and R 141b (1,1-dichloro-1-fluoroethane). Figure 3.15 shows the schematic of the boiling heat transfer unit which was used to obtain the boiling curves. The heater element is a 600 Watt cartridge heater embedded in thick copper specimen.

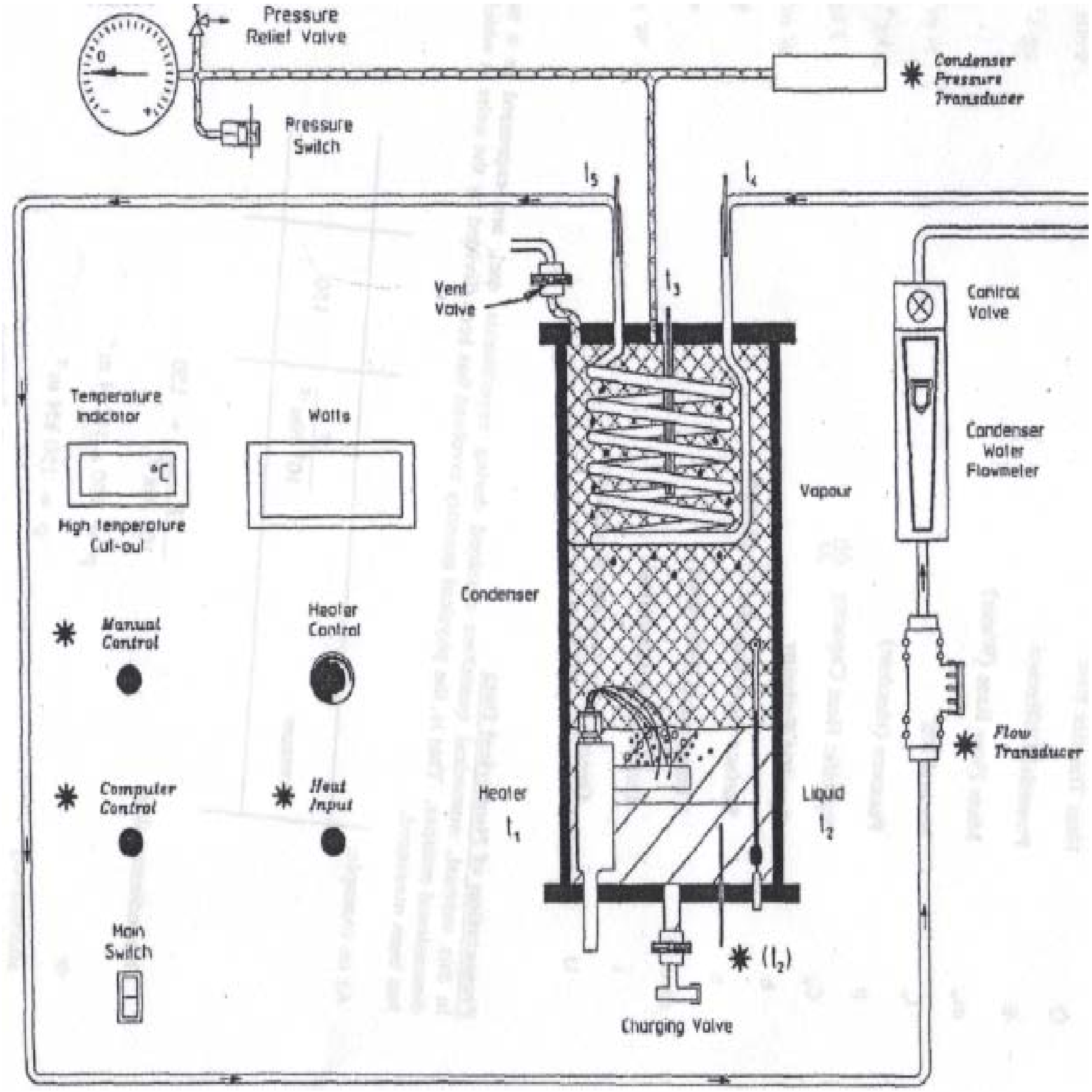

Figure 3.15. Schematic of Hilton Boiling Heat Transfer Unit (H655)

The boiling heat transfer unit was instrumented with K-type thermocouples and pressure transducers and connected to a data acquisition and computer system to record temperatures and pressures respectively. The condenser cooling water was run at flow rate of 0.2 gallons per minute. Figure 3.16 presents the boiling curve that has been obtained with Novec 7000 working fluid. The boiling experiment was run at 101.325 kilo Pascal (kPa). The total surface area of the heater element in the heat transfer boiling unit is 18 cm^2.

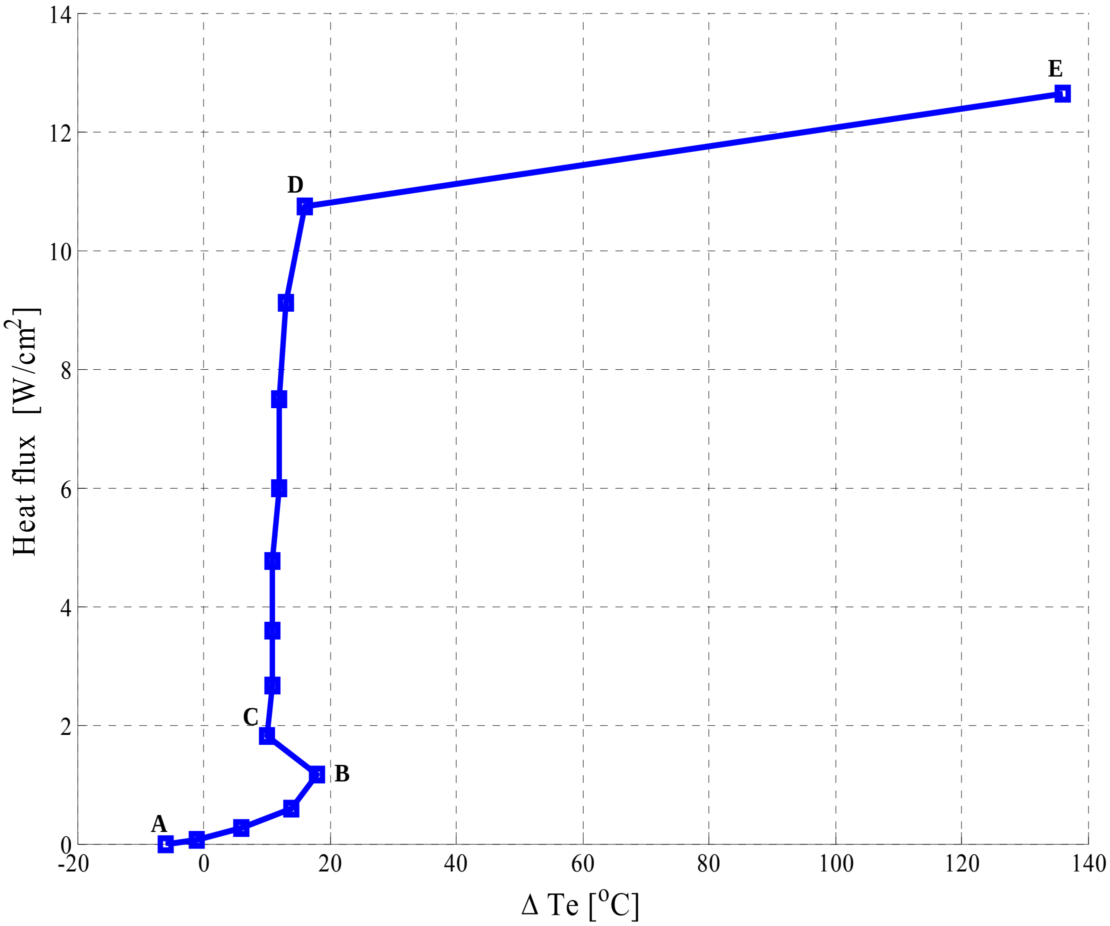

Figure 3.16. Boiling curve for Novec 7000 working fluid

In Figure 3.16, the heat flux has been plotted with the excess temperature to determine the boiling curve for Novec 7000 fluid. The excess temperature is defined as the difference between the surface temperature of the heater element and the saturation temperature of the working fluid (Novec 7000). The saturation temperature of Novec 7000 fluid at 101.325 kPa is 34 °C. Point A to B describes the free convection boiling regime. Small bubbles and/or vapor formed on the surface of the heater element. Maximum heat flux of 1.16 W/cm^2 is obtained at excess temperature ($\Delta T_e \leq \Delta T_B$) of about 18 °C in the free convection boiling regime.

Point B is the onset of nucleate boiling (ONB). There is initial excess temperature drop due to the bubble departure from the surface of the heater element and the phase change process. Point C to D describes the nucleate boiling regime. The vapor which formed on the heater surface initially departed as isolated bubbles. As the power to the heater element is increased, more vapor and/or bubbles are generated. The densely generated bubbles merged as slugs and escaped from the surface of the heater in the form of vapor jets and/or columns. Excess temperature range ($\Delta T_C \leq \Delta T_e \leq \Delta T_D$) of 10-16 °C is characterized in this regime. Maximum heat flux of 11 W/cm^2 is obtained in the nucleate boiling regime at excess temperature of about 16 °C.

At point D, transition boiling and/or unstable film boiling coexist. Point D to E describes the film boiling regime. Heat flux increase of only 1.91 W/cm^2 is achieved over a wide temperature range 16-136 °C in the film boiling regime. For the purpose of comparison, heat flux curve has also been determined for Refrigerant 141b (R141b) using the same boiling heat transfer equipment. Figure 3.17 shows the heat flux versus excess temperature that has been plotted for Novec 7000 fluid and R 141b in a nucleate pool boiling experiment.

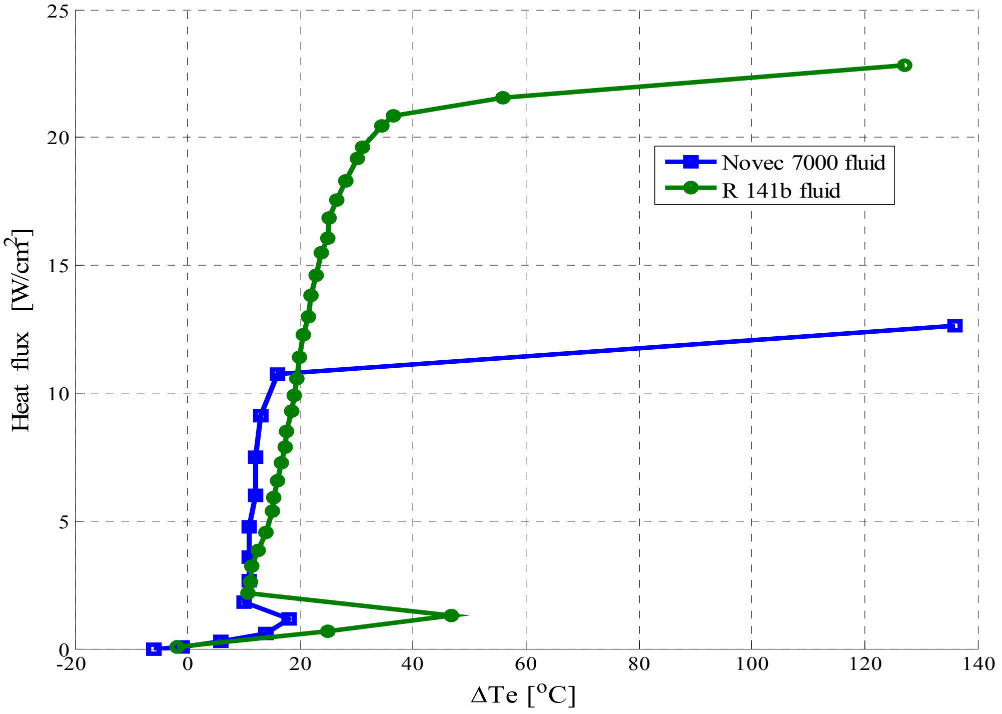

Figure 3.17. Nucleate boiling heat flux curves for Novec 7000 and R 141b

Figure 3.17 shows that critical heat fluxes of 11 W/cm^2 and 22 W/cm^2 are obtained at excess temperatures of 16 ^{o}C and 58 ^{o}C for Novec 7000 fluid and R 141b respectively. In heat transfer cooling applications where output heat flux range of 10-15 W/cm^2 is desired with lower excess temperatures, Novec 7000 fluid will be a good prospect as the cooling fluid. Unstable film boiling and/or film boiling were observed at excess temperatures above 80 ^{o}C for both Novec 7000 fluid and R 141b. Figure 3.18 illustrates snapshot of film boiling in the boiling experiment.

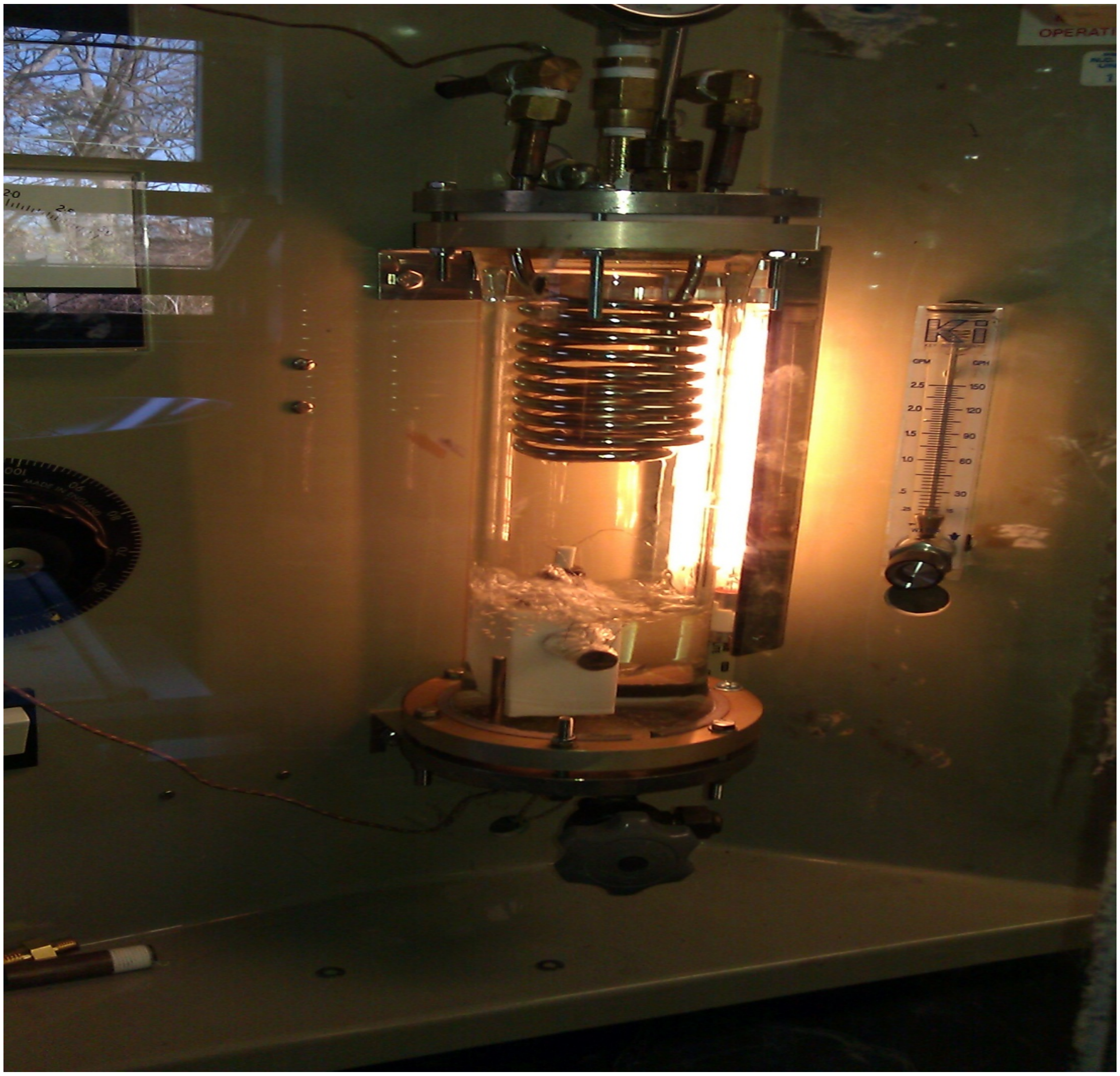

Figure 3.18. Film boiling regime

A blanket of vapor forms on the surface of the heater element as shown in Figure 3.18. The vapor blanket insulates the heater element therefore decreasing the fluid interacting with the heater element. Heat transfer performance was reduced. The boiling experiment has been expanded into spray cooling experiments. Results obtained in the spray cooling experiments are presented in Chapter 4.

3.5.2 Numerical Analysis

Numerical computations on heat conduction through test substrates have been carried out to obtain the temperatures profiles at various sections across the test substrates. Ansys Gambit and Fluent software were used for the numerical simulations. The computational domain was developed and meshed with Ansys Gambit. The meshed domain was exported to Ansys Fluent for the numerical simulations. Figure 3.19 shows the meshed domain that was transported to Ansys Fluent for the computations.

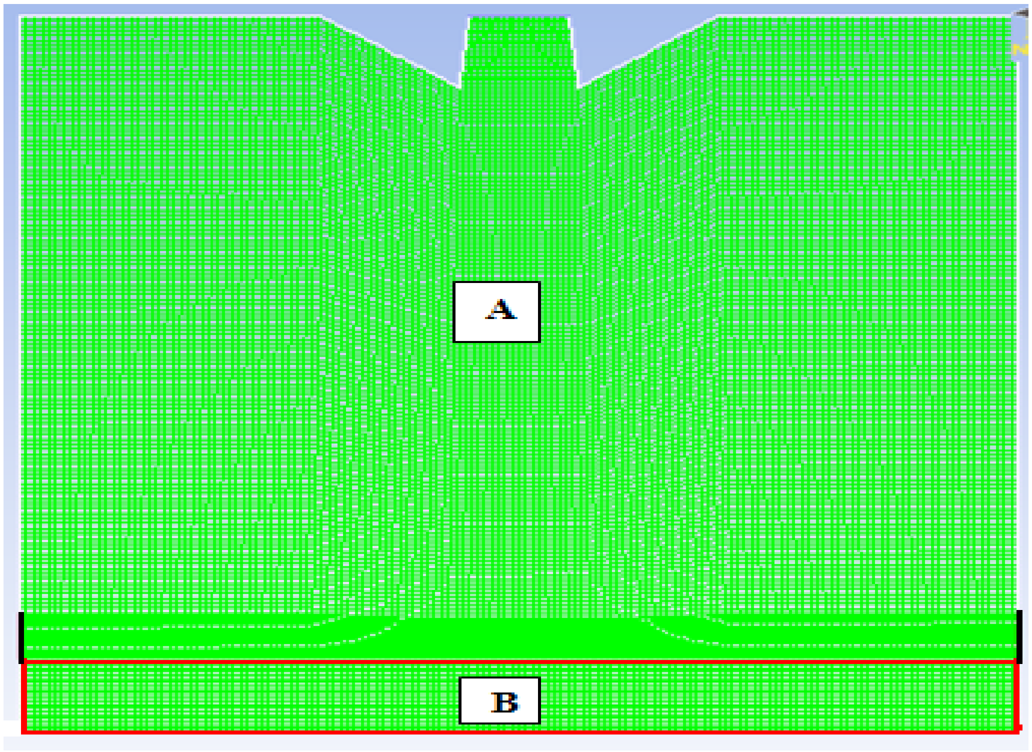

Figure 3.19. Meshed domain for computational simulations

As shown in Figure 3.19, regions A and B are the fluid and solid domains respectively. Total computational domain of 0.04 m x 0.025 was used for the numerical simulations. Nodal spacing based on exponential meshing scheme was used to obtain finer mesh near the surface of the heated substrate. The boundary conditions used for the computations are presented in Table 3.7.

Table 3. 7. Boundary conditions for numerical computations

Position	Boundary condition
Inlet	Velocity inlet
Exit	Outflow
Sides	Wall
Surface of heated substrate	No slip and Conduction heat transfer
Bottom of heated substrate	Constant heat flux

Two meshed domains were considered for numerical computations for grid independence. The stream function was used as a measure for the grid independence study. Table .3.8 presents the domain sizes and the respective stream functions which were obtained. The corresponding numerical results are shown in Figure 3.20 below.

Table 3. 8. Grid independence study

Mesh	Number of cells	Number of faces	Number of nodes	Stream function [kg/s]
1	56,000	112,480	56,481	0.00201
2	39,600	79,600	40,001	0.00199

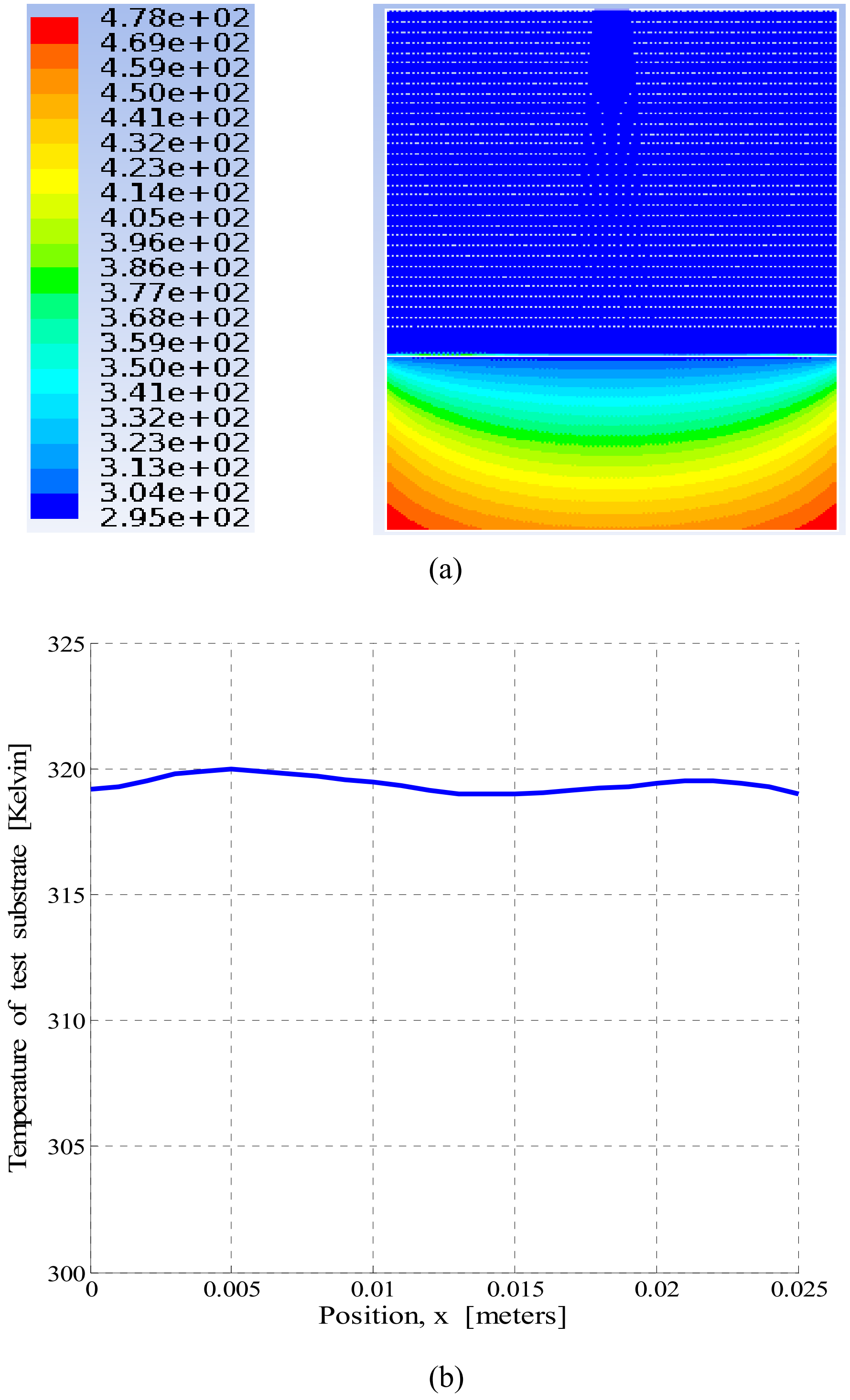

Figure 3.20. Numerical results: (a) temperature contour (b) temperature profile of surface

Figure 3.20 (a) and (b) show the temperature contour and the surface temperature of the heated substrate respectively. The result shows that the temperature profile along the surface of the heated substrate is significantly constant. Temperature range of about 319-320 ^{o}K (46 - 47 ^{o}C) was obtained at heat flux of 20 W/cm^{2}. An average temperature of 319.5 ^{o}K (46.5 ^{o}C) is therefore good representation of the surface temperature of the heated substrate. Mean temperature variation of 0.5 ^{o}C is therefore recorded. Figure 3.21 shows the temperature profile at the bottom and the top surface of the heated substrate at heat flux of 100 W/cm^{2}.

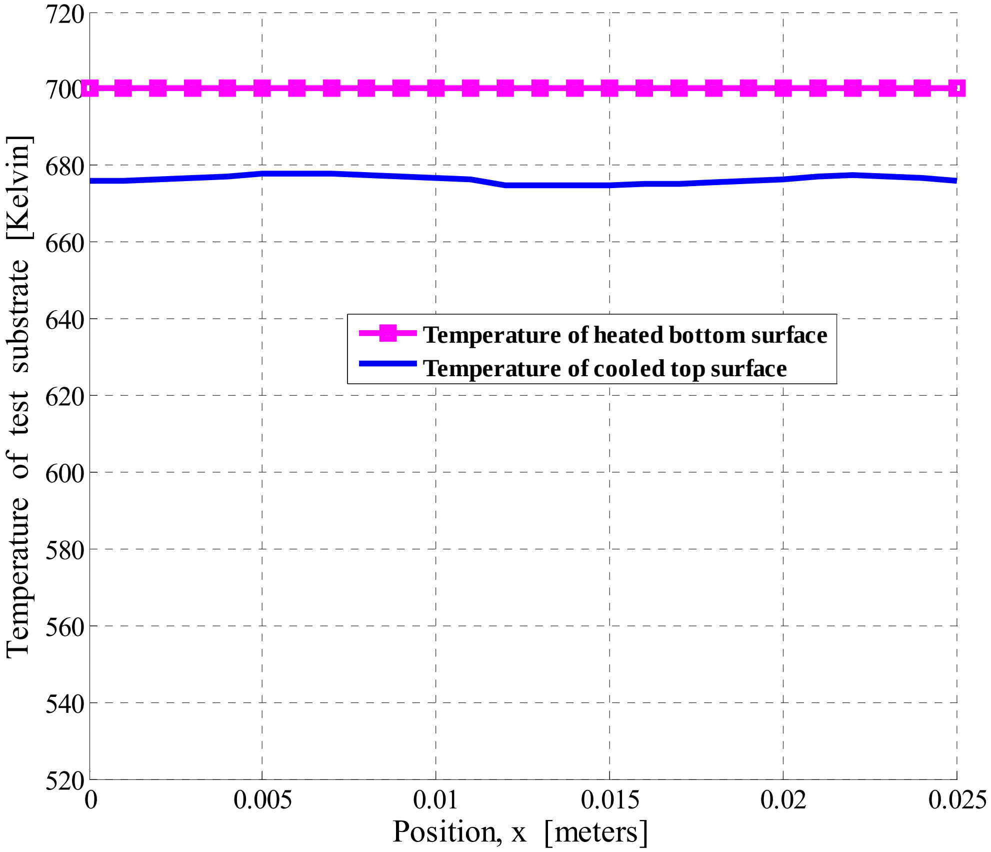

Figure 3.21. Temperature profile at bottom and top surface of substrate

As shown in Figure 3.21, the temperature at the bottom of the heated substrate where constant heat flux is applied is at constant temperature of 700 ^{o}K (427 ^{o}C). At the top surface of the heated substrate, no slip and conduction heat transfer boundary conditions were applied. The temperature at the surface of the heated substrate is in range of 675-678 ^{o}K (402 - 405 ^{o}C). Average temperature of 676.5 ^{o}K (403.5 ^{o}C) is a good representation of the surface temperature of the heated substrate. Mean temperature variation of 1.5 ^{o}C is measured. Based on the numerical results and for practical considerations, instrumentation of the heated substrate with two thermocouples and finding the average will give a good representation of the mean surface temperature of the heated substrate within the experimental error. Figure 3.22 illustrates the velocity contour magnitudes of the computational domain.

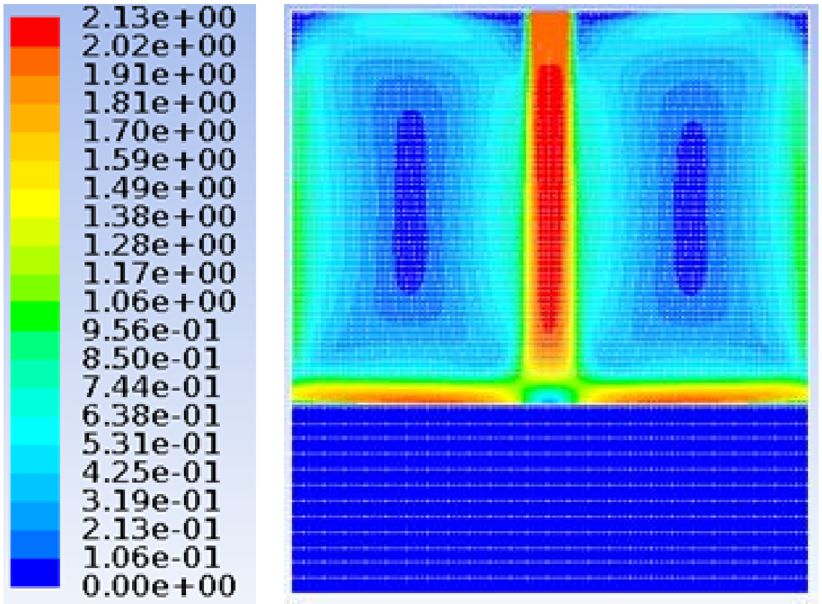

Figure 3.22. Velocity contour magnitudes of computational domain

3.5.3 Characterization of Modified Surfaces

The modified surfaces have been characterized using digital image processing tools to determine the profile of the groove characteristics. Unidirectional and multi-directional grooves were analyzed. Snapshot images of the surface modification were taken using AxioCam MKC5 microscope (manufactured by Zeiss) at magnification of 1.25x. The images were then processed using Image J software. Figure 3.23 shows the surface profile of the multi-directional grooves which was analyzed using Image J.

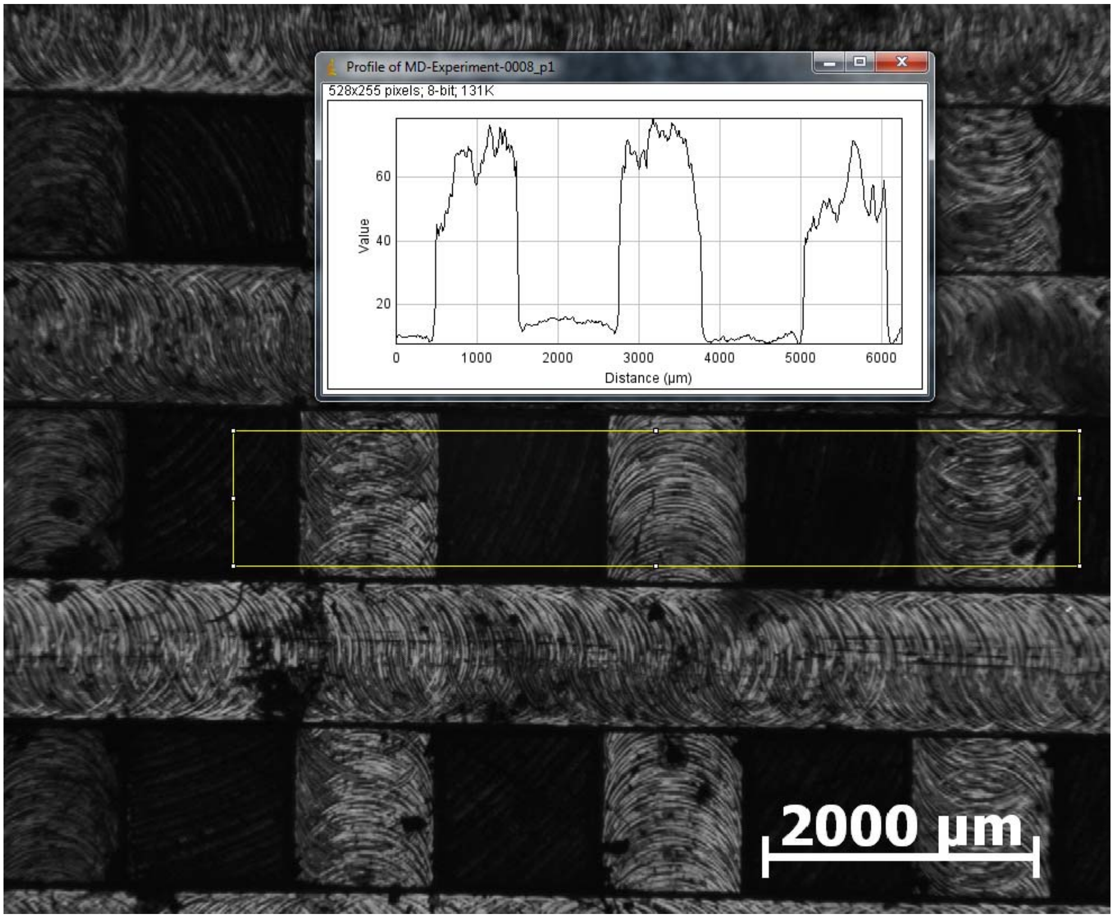

Figure 3.23. Surface profile of the modified surface

Figure 3.23 illustrates the profiler of the multi-directional quadrilateral-shaped grooves of the 1270 µm x 1270 µm modified surface. The crest and trough represent the protrusions and recess of the modifications on the surface. The processed digital images show unevenness on the crest of the modified surface. The modification of the surface has also been analyzed based on color contour to show the channels of the modified surface. Figure 3.24 shows a 3-D color contour of the surface topography of a section of the modified surface. The heat transfer performance of the modification of the surface is presented in Chapter 4.

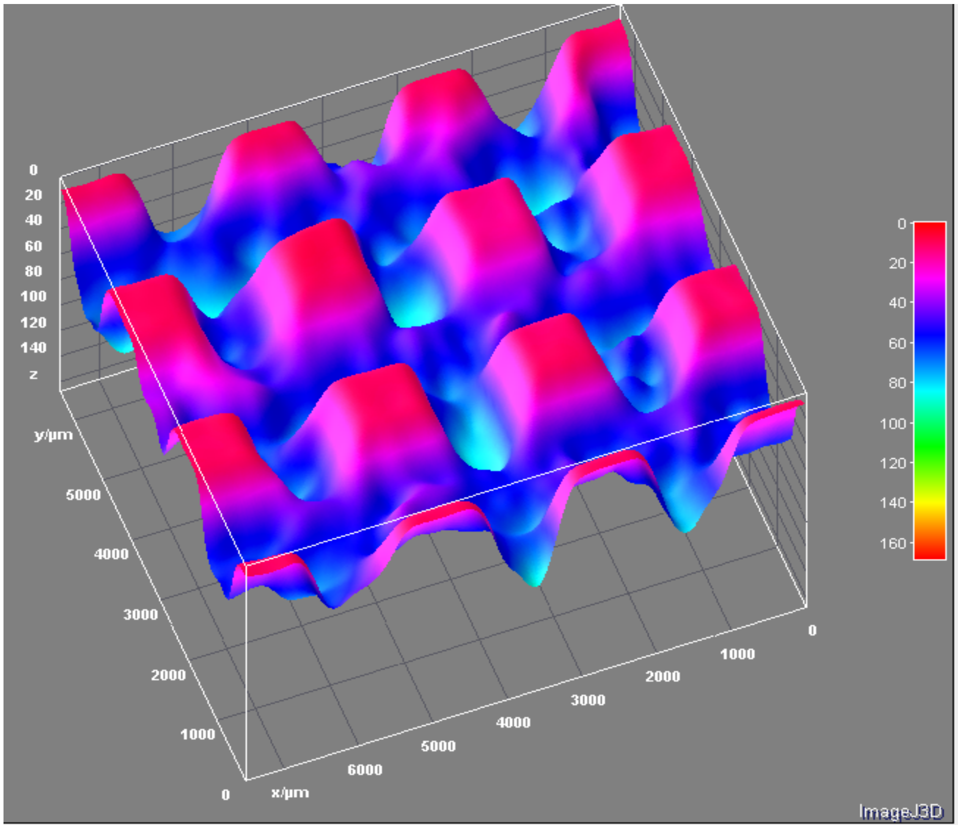

Figure 3.24. 3-D plot of surface topography of modified surface

The heat transfer performance of the parameters considered for this work is reported in the form of heat flux versus cooling temperature difference. The uncertainty with the reported data is presented below. The generalized experimental uncertainty (U_c) of output F based on inputs values of x is presented as Equation 3.29.

$$U_c = \sqrt{\left(\frac{\partial F}{\partial x_i}\Delta x_i\right)^2} \qquad \textbf{(3.29)}$$

Applying Equation 3.29 in finding the experimental uncertainty with the heat flux measurement U_q, Equation 3.30 is obtained. In Equation 3.30, A and P represent the surface area and the power to the substrate respectively.

$$U_q = \sqrt{\left(\frac{\partial q}{\partial A}\Delta A\right)^2 + \left(\frac{\partial q}{\partial P}\Delta P\right)^2} \qquad \textbf{(3.30)}$$

Equation 3.30 is evaluated to obtain the experimental uncertainty of the heat flux as:

$$U_q = \sqrt{\left(-\frac{P}{A^2}\Delta A\right)^2 + \left(\frac{1}{A}\Delta P\right)^2} \qquad \textbf{(3.31)}$$

A mean uncertainty on the experimental results for the heat flux is therefore obtained using Equation 3.31. Based on the preliminary results obtained in the spray cooling experiments, the maximum uncertainty for the heat flux is 7.83 W/cm^2. The maximum mean heat fluxes reported in Chapter 4 are therefore presented as:

$$\overline{q} = q \pm 7.83 \qquad W / cm^2 .$$

The results obtained in the spray cooling experiments are presented in the results and discussions section of Chapter 4. In addition, analytical results are also presented.

CHAPTER 4

RESULTS AND DISCUSSIONS

The data obtained in spray cooling experiments have been analyzed and the results are presented in this section. The results are presented in the form of: heat flux versus cooling temperature difference; heat transfer coefficient versus cooling temperature difference; and spray cooling heat transfer regimes versus the excess temperature. Water and Novec 7000 engineering fluid were the two working fluids which were used to obtain the data during the spray cooling experiments. The test and operational conditions during each experiment were recorded and are reported in this section.

The results reported in this chapter have been obtained as averages of consistently repeated experiments. The test and operational conditions were fixed in each of the repeated experiments. The ranges of flow rate of the working fluid recorded in the experiments are 0.84-1.26 grams per second (gps) and 1.18-1.77 grams per second for water and Novec 7000 fluid respectively. The thermal loop system pressure for both water and Novec 7000 fluid was in range of 101.45-165.80 kPa. The following section presents the results of the parametric studies based on the specific objectives of the present research work.

4.1 Effects of Test Surface Area Scalability on Critical Heat Flux (CHF)

Figure 4.1 shows heat flux versus cooling temperature difference (ΔT) plotted for the various tested surface areas of the substrates with water as the working fluid. The working fluid flow rate was set at 0.84 gps for all the four surfaces tested. The plot shows the heat flux curves for specific test substrate area sizes (5.07 cm^2, 7.92 cm^2, 11.40 cm^2 and 20.27 cm^2). The cooling temperature difference is defined as the difference between the substrate surface temperature and the temperature of the cooling fluid.

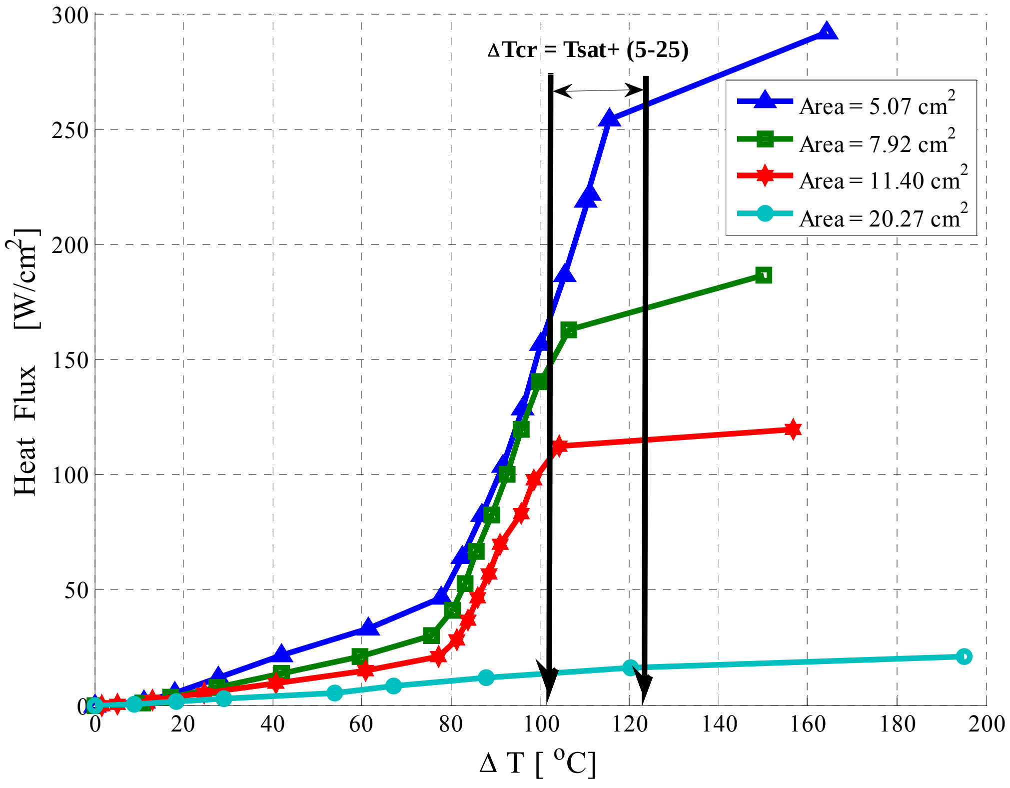

Figure 4.1. Spray cooling heat flux curves for different area sizes

As shown in Figure 4.1, the heat fluxes for all the four tested substrates of different area sizes are linear and below 50 W/cm^2 at cooling temperature difference lower than 80^{o}C. The heat fluxes increase sharply for all substrates at temperature difference between 85-120 ^{o}C. Increased vapor generation rates were observed on the surface of the test substrates at cooling temperature difference between 85-120 ^{o}C. In addition, Figure 4.1 shows that the maximum heat flux decreases with increasing area sizes. Critical heat flux of 254 W/cm^2 was obtained for the 5.07 cm^2 area size at cooling temperature difference of 118 ^{o}C. Critical heat fluxes of 170 W/cm^2 and 120 W/cm^2 were obtained for 7.92cm^2 and 11.40cm^2 area sizes respectively at cooling temperature difference of about 110 ^{o}C. The results indicate that critical heat flux occurs when the cooling temperature difference is about 5-25^{o}C above the saturation temperature with water as the working fluid.

For the 20.27 cm^2 area size, the surface temperature of the test substrate increased sharply for the first few power inputs and equilibrium temperature could not be attained. The experiment therefore could not be carried to completion due to the initial temperature instability of the test substrate. Observations at the surface of the 20.27 cm^2 test substrate showed that there was poor fluid coverage on the test surface. The impact area of the fluid spray (about 12 cm^2) by the M2 nozzle type was observed to be lower than the 20.27 cm^2 area size. Much of the surface was therefore dry of the fluid droplets.

However, for the other tested substrates with surface area sizes (5.07 cm^2, 7.92 cm^2 and 11.40 cm^2), the surface areas were observed to be subscribed by the impact area of the fluid spray. Fluid coverage was therefore optimized for these surface areas of the test substrates. It is therefore important that for single nozzle spray cooling, the surface area of the test substrate be selected such that it is subscribed by the impact area of the fluid spray. Figure 4.2 shows schematically the fluid coverage that was observed on the surface of the substrates for different area sizes during fluid impingement on the test surface.

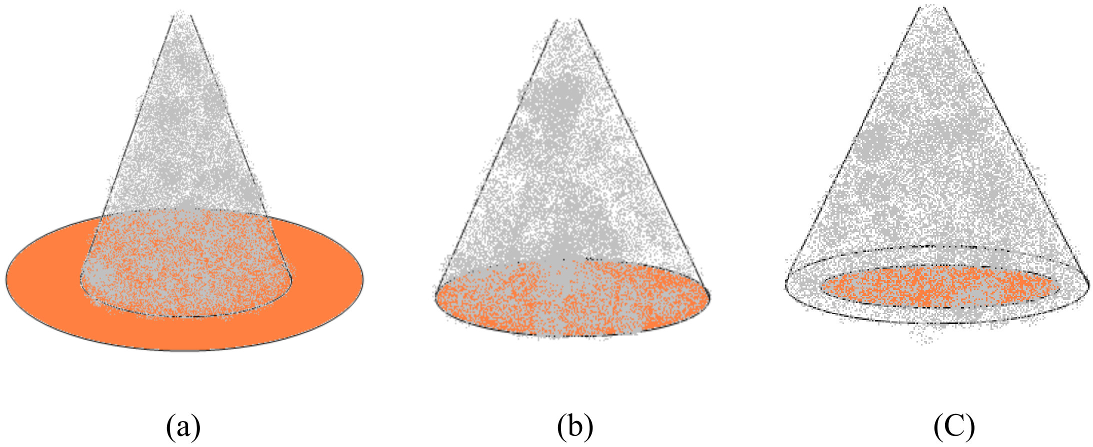

Figure 4.2. Fluid coverage on test surface of different area sizes: (a) Area of 20.27 cm^2, (b) Area of 11.40 cm^2 and (c) $A_{surface}$ less than A_{spray}

Figure 4.2 is an illustration depicting that with substrate surface area sizes equal to and/or below the spray impact area ($A_{substrate} \leq A_{spray}$), the spray fluid covers the test surface sufficiently. The working fluid is therefore optimally managed in the spray cooling process. Dry zones are avoided on the test surface of the substrates. However, poor fluid coverage was observed for test surface areas which were larger than the fluid spray impact area. Therefore, for practical applications and optimal fluid management, the surface area of the test substrate should be selected such that it is sufficiently subscribed by the fluid spray impact area. For test substrates with larger surface areas than the spray impact area, methods have been developed to ensure fluid spread and test surface wettability. The section below presents how wicking grooves and/or modified surfaces have been used to increase the fluid spread on larger surfaces of the test substrates.

4.2 Effects of Surface Modifications on Heat Transfer Performance

Heat transfer performance curves have been obtained for modified and smooth surfaces with water as the working fluid. The flow rate of the working fluid was set at 1.26 grams per second to obtain the experimental data for both the modified and smooth surfaces. The heat transfer performance was measured in terms of heat flux gains and heat transfer coefficient enhancement. The following section presents the heat transfer performance of the modified surface compared to the smooth surface, first with heat flux versus cooling temperature difference and then with heat transfer coefficient versus cooling temperature difference.

4.2.1 Heat Flux Gain of Modified Surface over Smooth Surface

The heat transfer performance of the modified surface which is measured in terms of heat flux is compared to that of a smooth surface. The modified surface was developed in a form of wicking grooves. Figure 4.3 shows the heat flux versus cooling temperature difference (ΔT) plotted for the modified and the smooth surfaces. The cooling temperature difference is the difference between the surface temperature of the substrate and that of the working fluid.

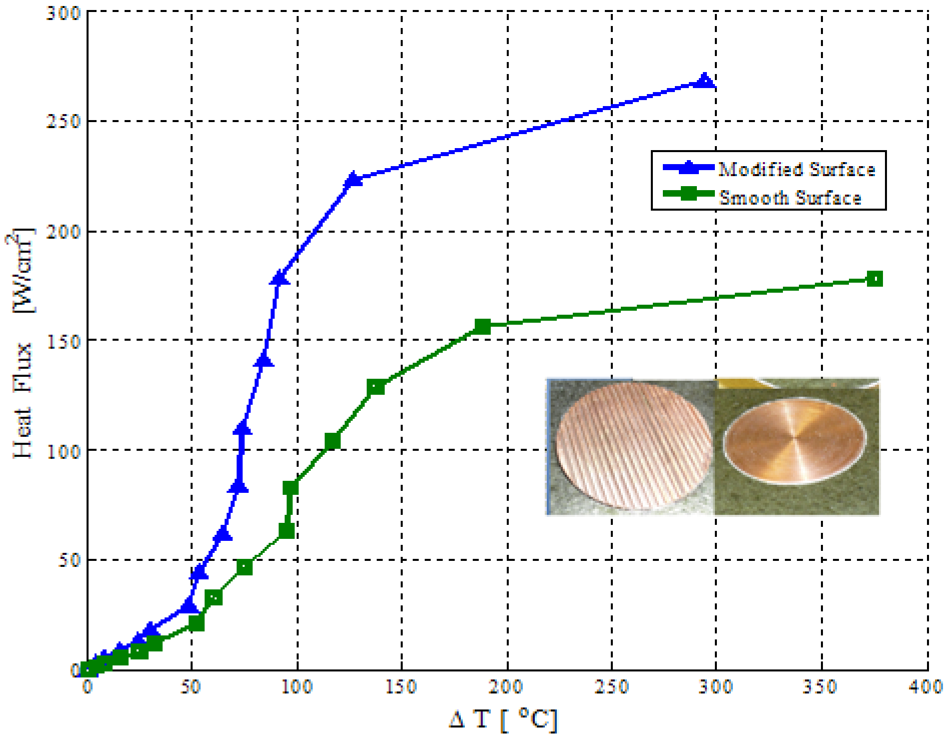

Figure 4.3. Spray cooling heat flux curves for modified and smooth surfaces

Figure 4.3 shows that there is no significant difference in the heat fluxes for the modified and smooth surfaces at cooling temperature difference below 50 °C. However, at cooling temperature difference above 75 °C there is appreciable difference in the heat fluxes obtaind for the modified and smooth surfaces. Heat flux gain of about 130% is obtained for the modified surface over the smooth surface at cooling temperature difference of about 90 °C.

Higher critical heat flux is obained for the modified surface over the smooth surface. Critical heat flux of 225 W/cm^2 and 160 W/cm^2 at cooling temperature differeence of 130 °C and 180 °C were obtained for the modified and smooth surfaces respectively. The modified surface therefore has higher heat transfer performance (measured in terms of heat flux) than the smooth surface. In addition, lower cooling temperature differences were obtained for the modfied surface over the smooth surface. Modified surfaces in the form of wicking grooves can therefore be deployed in spray cooling heat transfer applications where higher heat fluxes and lower cooling temperature difference are desired. The section below presents the heat transfer performance of the modified surface compared to that of a smooth surface, measured in terms of heat transfer coefficient

4.2.2 Heat Transfer Coefficient Enhancement of Modified Surface

The heat transfer performance of the modified surface has also been measured in the form of heat transfer coefficient. The result is compared to that of a smooth surface. The same operating conditions were ensured during the spray cooling experiments. Water was used as the working fluid in both experiments with flow rate set at 1.26 grams per second. Figure 4.4 shows the heat transfer coefficient versus the cooling temperature difference (ΔT) for the modified and the smooth surfaces.

The result shows that the heat transfer coefficient increases for the modified and smooth surfaces upto cooling temperature difference of about 100 ^{o}C and 135 ^{o}C respectively. Higher heat transfer coefficients are obtained for the modified surface than the smooth surface. Maximum heat transfer coefficient enhancement of 8500 W/m^2-K is achieved at cooling temperature difference of about 100 ^{o}C for the modified surface over the smooth surface. Beyond cooling temperature difference of about 140 ^{o}C, there is significant reduction in the heat transfer coefficient for both the smooth and modified surfaces.

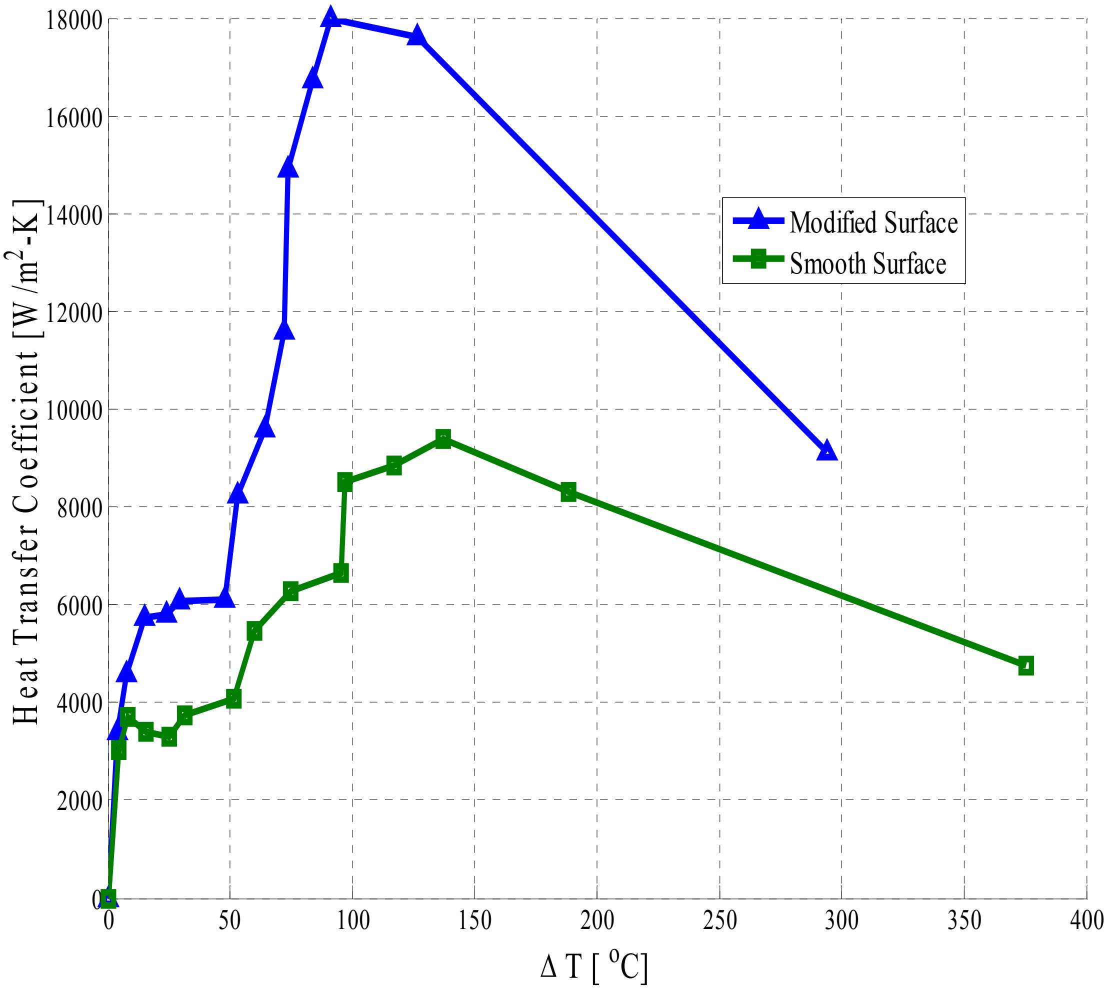

Figure 4.4. Heat transfer coefficient for modified and smooth surfaces

Thermally induced splashing of impacting spray fluid into smaller skidding droplets was observed at very high surface superheats (>140 °C) during the experiments. The small skidding fluid droplets at the high surface superheats reduced the surface-to-fluid interaction. Test surface wettability was therefore reduced. In addition, the smaller skidding droplets delayed evaporative cooling and therefore mitigating the heat transfer coefficient. Figure 4.5 below shows the thermally induced splashing of the impacting fluid into smaller droplets on a heated surface at surface supeheat of 140 ^{o}C.

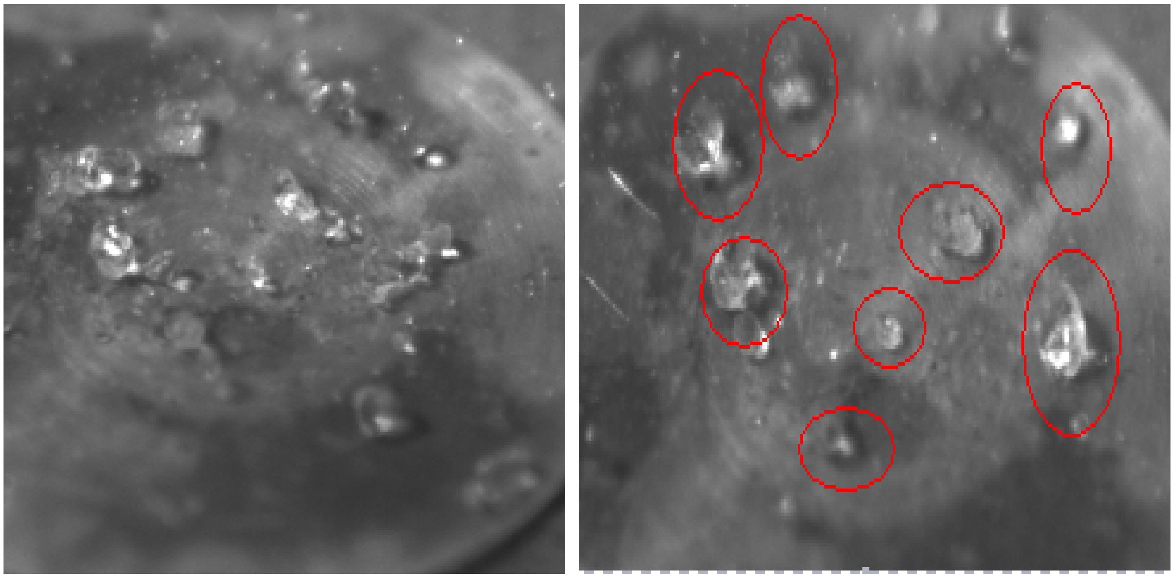

Figure 4.5. Thermally induced splashing of impacting fluid droplets

Figure 4.5 shows small fluid droplets skidding on the surface of the heated substrate at high surface superheats. Surface superheat temperatrure ($\Delta T > 140$ ^{o}C) was recorded. Visualization and image processing tools were therefore used to observe a single fluid droplet impinging on a smooth surface at surface superheats temperature of 140 ^{o}C and above. Figure 4.6 shows an impacting fluid droplet on a smooth surface at surface superheat temperature of 140 ^{o}C.

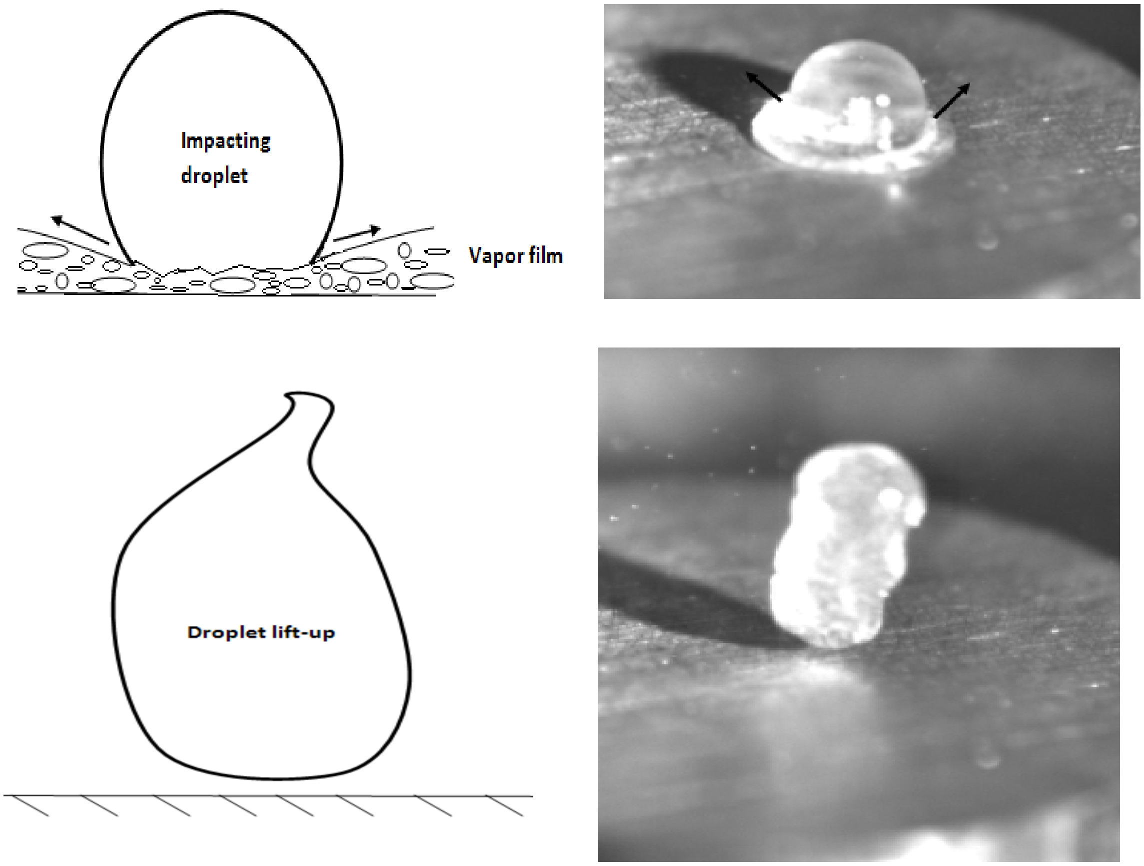

(a)

(b)

Figure 4.6. Impacting droplet at high surface superheat: (a) schematic (b) snapshots

Figures 4.6 (a) and (b) show the schematic and snapshots from the experiment of the impacting fluid droplet on the heated substrate respectively. Vapor film forms between the fluid droplet and the surface of the substrate as shown in Figure 4.6. The vapor film layer causes the fluid to skid and/or lift-up from the surface of the substrate. The formation of the skidding and/or lift-up fluid droplet on the smooth surface decreased the wettabilty of the test surface. The experiment was repeated on the modified surface. Figure 4.7 shows an impacting fluid droplet on the modified and smooth surfaces at the same suface superheat of 140 ^{o}C.

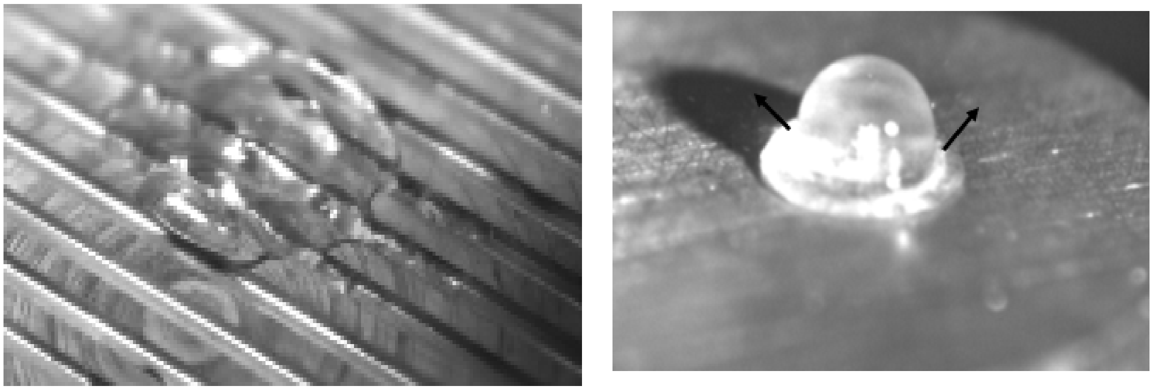

(a) (b)

Figure 4.7. Impacting fluid droplet on (a) modified and (b) smooth surfaces

Figures 4.7 (a) and (b) show the fluid-to-surface interactions of the impacting fluid droplet on the modified and smooth surfaces respectively. The fluid droplet skids and/or rebound on the smooth surface. For the modified surface, fluid skidding and/or rebound was avoided due to the wicking phenomenon of the surface. The capillary wicking forces dominate the rebound forces for the modified surface. Surface wettability was increased with the modified surface. Modified surfaces in the form of wicking grooves can therefore be used to enhance surface-to-fluid interactions in thermal management schemes at high surface superheats. Figure 4.8 shows snapshots of the wicking phenomenon on the modified surfaces. The modification of the surface was developed in the form of wicking grooves.

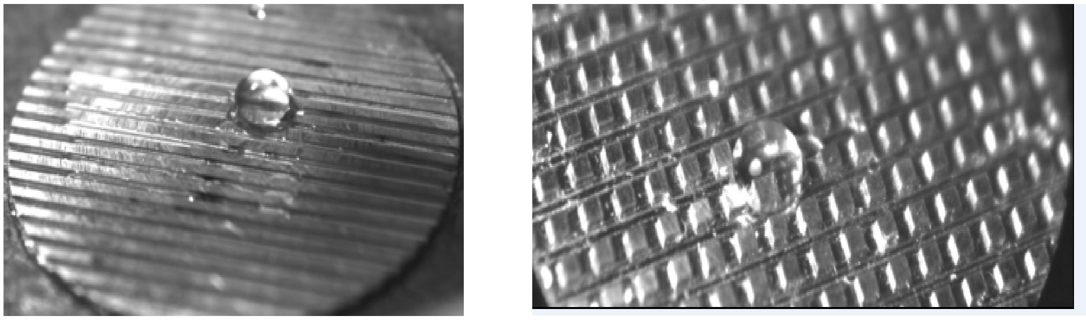

t = 0.001 seconds

t= 0.001 seconds

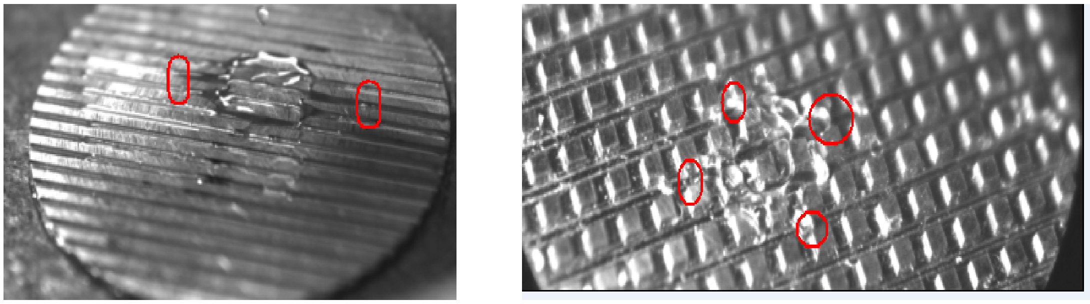

t = 0.101 seconds

t= 0.101 seconds

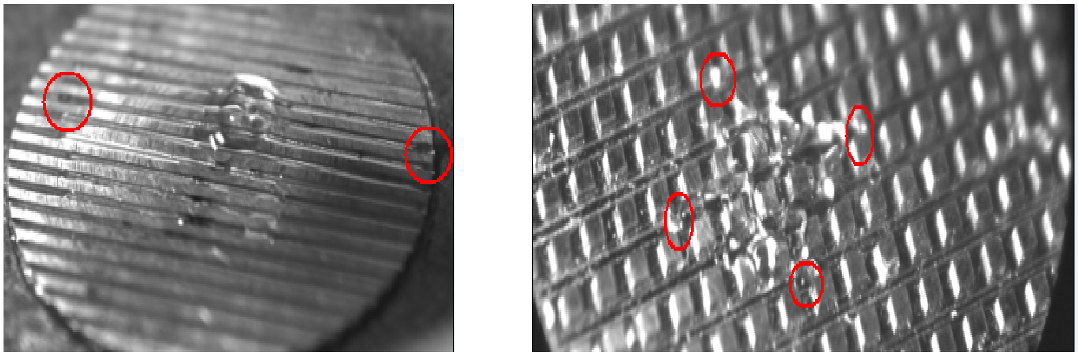

t = 0.189 seconds

t = 0.189 seconds

(a)

(b)

Figure 4.8. Wicking phenomenon on (a) unidirectional and (b) multi-directional surfaces

Figures 4.8 (a) and (b) show the wicking phenomenon on the unidirectional and multi-directional modified surfaces respectively. The red circles show the tip of the wicking fluid at different times after fluid impingement. Wider extent of fluid spread is associated with the unidirectional grooves than the multi-directional grooves as shown in Figure 4.8. The multi-directional grooves decreased the wicking phenomenon due to intermittent wall breaks. Experimentally determined wicking velocities of 0.134 m/s and 0.016 m/s are obtained for the unidirectional and multi-directional grooved surfaces respectively. The wicking velocities were also determined analytically. Figure 4.9 shows the analytical wicking velocity versus half-corner angles of characteristic grooves.

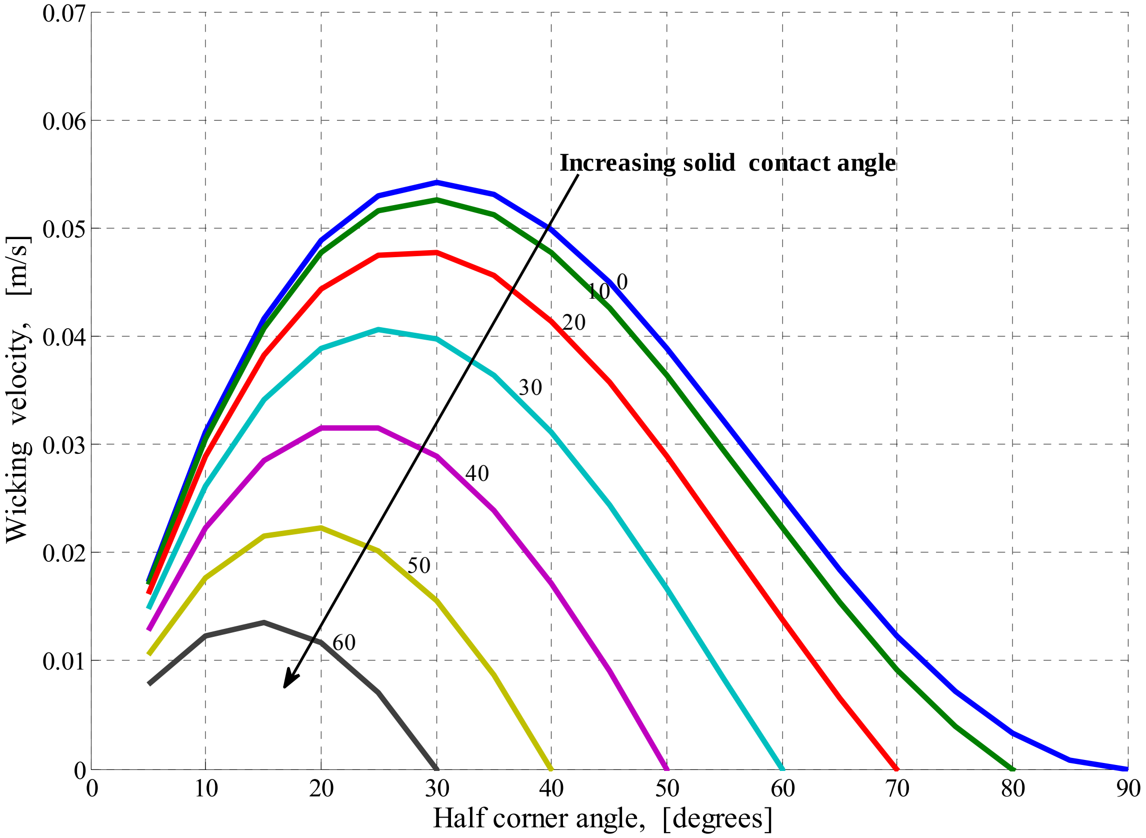

Figure 4.9. Wicking velocity (tip velocity) versus half corner angle

Figure 4.9 shows that the wicking velocity decreases with increasing solid contact angles. At all half-corner angles, the zero solid contact angle fluid has higher wicking velocities. A perfect wetting surface therefore has higher wicking velocity than less wetting surfaces. At half-corner angle of 30 degrees, highest wicking velocity of about 0.055 m/s is obtained when the wicking fluid assumes a zero contact angle with the surface. High wicking velocity increases the convective heat transfer terms associated with spray cooling.

From the foregoing parametric considerations, wicking grooves of half-corner angle of 30 degrees are therefore of practical use in spray cooling applications. Total corner angle of the groove at about 60^o gives the optimal groove design. Enhanced fluid spread on 60^o grooved surfaces due to capillary wicking and/or driven flow results in thin liquid film evolution on the surface. Therefore, for thermal management schemes where evaporative cooling of thin liquid film is desired, such surfaces are of great practical use. The following section presents the heat flux regimes which were observed in the spray cooling experiments.

4.3 Heat Flux Regimes in Spray Cooling Heat Transfer

Heat flux curve has been obtained on a smooth surface with area of 11.40 cm^2 with Novec 7000 as the working fluid. The result is compared to that of water as the working fluid. Figure 4.10 below shows the heat flux versus cooling temperature difference for Novec 7000 and water as the working fluids. The working fluid flow rate was set at 1.20 grams per second in both experiments. The cooling temperature difference is defined as the temperature difference between the substrate surface temperature and that of the cooling fluid.

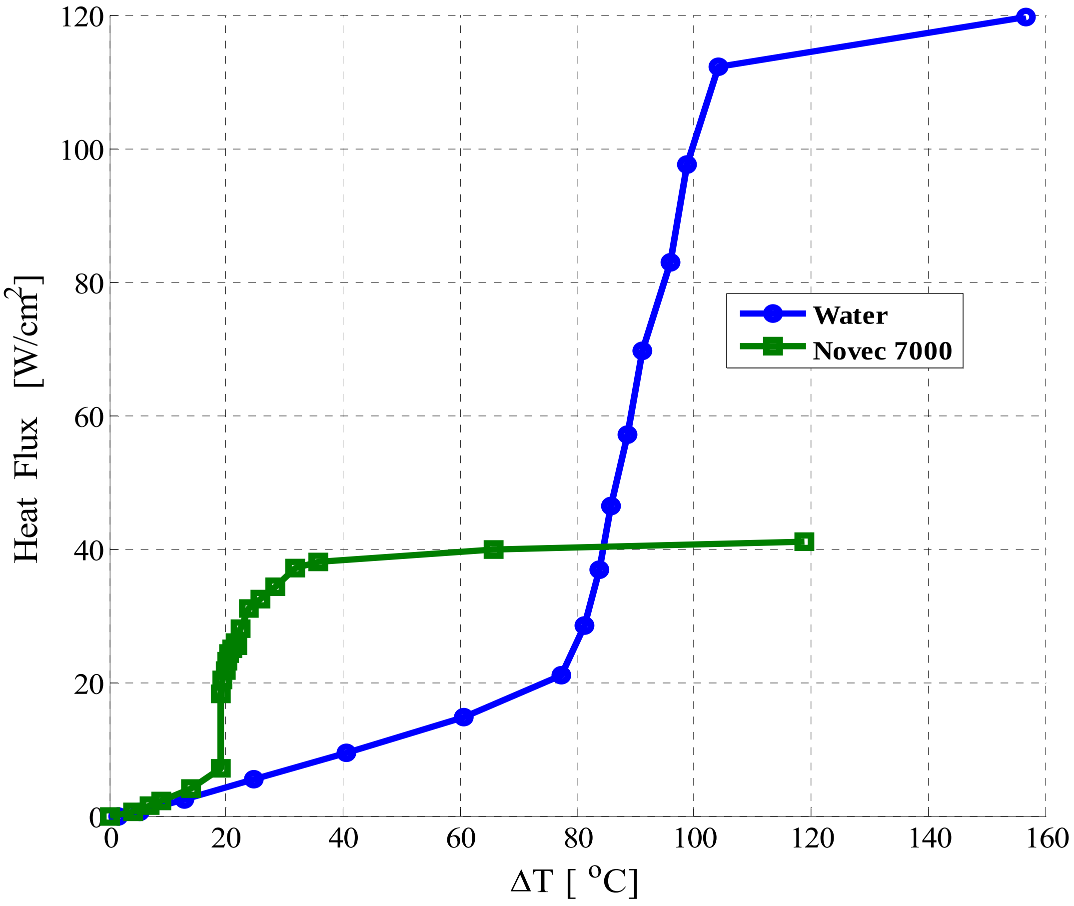

Figure 4.10. Heat flux curves for water and Novec 7000 working fluids

Figure 4.10 shows the heat flux comparison for water and Novec 7000 as the working fluids. The cooling temperature difference (ΔT) is the difference between the surface temperature of the test substrate and the working fluid. As shown in Figure 4.10, there is no significant heat flux difference between water and Novec 7000 at cooling temperature difference below 20 °C. However, at cooling temperature difference above 20 °C, there is appreciable heat flux difference between the water and Novec 7000 as the working fluids. Novec 7000 and water have boiling points of 34 °C and 100 °C respectively at 101.325 kPa (1 atm) pressure. Heat flux increase of 30 W/cm^2 and 90 W/cm^2 were achieved over cooling temperature difference range of 20-40 ^{o}C and 78-105 ^{o}C for the Novec 7000 fluid and water respectively. The high heat flux increase over this cooling temperature difference range for the Novec 7000 fluid and water is attributed to the phase change which occurs at the boiling points of the working fluids.

Maximum heat fluxes of about 40 W/cm^2 and 115 W/cm^2 were obtained at cooling temperature difference of 62 ^{o}C and 102 ^{o}C for Novec 7000 and water respectively. Higher critical heat flux is therefore obtained with water as the working fluid. However, at heat fluxes above 14 W/cm^2 and up-to critical heat flux, lower cooling temperature differences are obtained with Novec 7000 as the working fluid. Novec 7000 working fluid is therefore a good prospect as cooling fluid in thermal management schemes where lower touch temperatures are desired. Further investigations were conducted to understand the heat flux regimes in spray cooling applications and are presented in the following section.

Experimental setups which include fast speed image logging and data acquisition systems were developed to collect data on bubble generation; bubble departure; and bubble rupture in spray cooling experiments. High speed video camera set at 10,000 frames per second was used to acquire the data and images on the bubble phenomenon. In addition, K-type thermocouples were used to monitor the surface temperature of the heated substrate in the various heat flux regimes. Figure 4.11 shows the various heat flux regimes which have been observed in a spray cooling experiment with water as the working fluid.

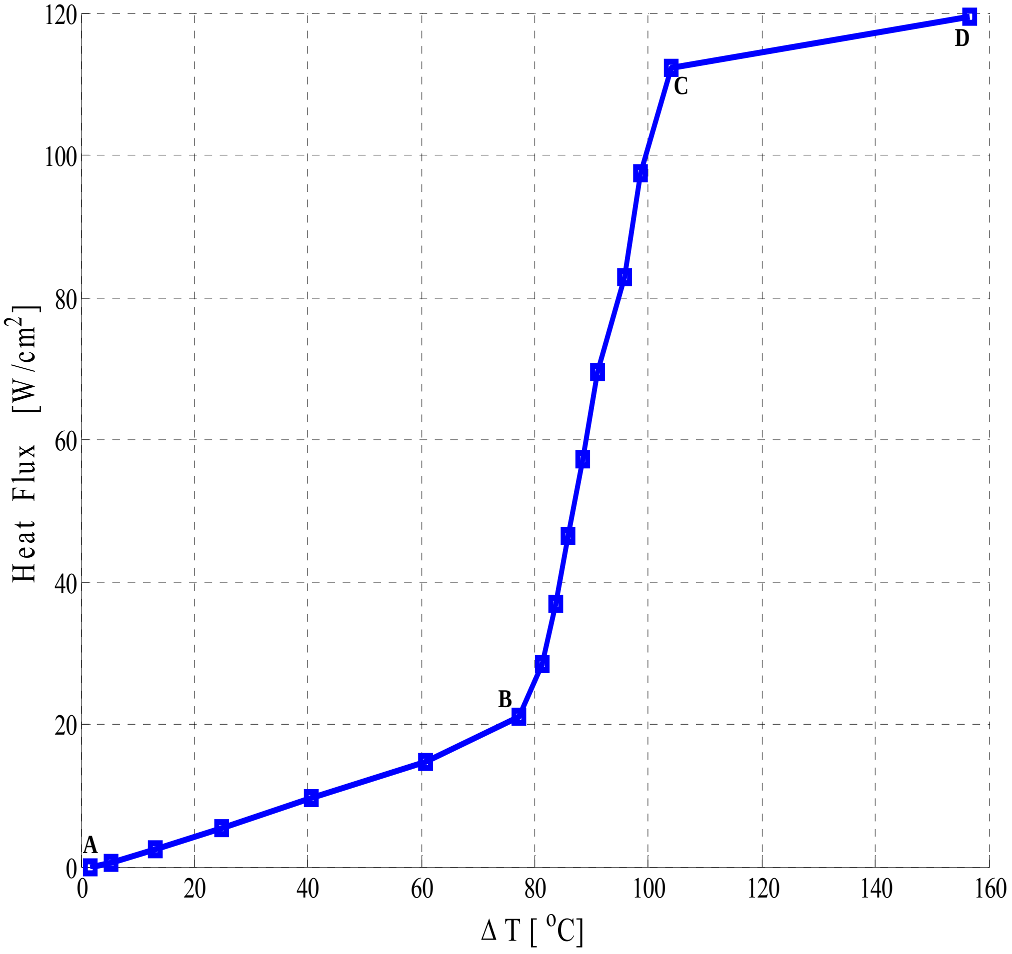

Figure 4.11. Heat flux regimes in spray cooling experiment

Figure 4.11 shows the range of cooling temperature differences which were obtained at various heat fluxes using water as the working fluid. The points which mark the heat flux regimes are identified with the letters A-B; B-C; and C-D. Forced convection heat transfer is associated from the range A-B. The cooling temperature difference, ($\Delta T \leq \Delta T_B$) is about 80 ^{o}C. In this regime, forced non-boiling heat transfer occurs and no vapor is generated. Highest heat flux of about 20 W/cm^2 was achieved in this regime

At cooling temperature difference above point B, small bubbles were observed on the surface of the test substrate. The bubble generation increased from point B to C. Phase change of the liquid fluid into vapor increased the heat flux drastically from point B to C. Heat flux increase of about 90 W/cm^2 was achieved in this regime over cooling temperature difference range of 78-104 ^{o}C. Cooling temperature difference up-to 104 ^{o}C ($\Delta T_C \approx 104$ ^{o}C) was recorded. Close to point C, most of the small bubbles which form on the surface of the test substrate coalesce into single bubble.

At point C and beyond, the single bubble formed from the small bubbles grows and ruptures on the surface of the substrate. At cooling temperature difference close to point D, there is delay in the rupture of the single bubbles. The single bubbles formed a dome structure with vapor core. The vapor core inside the single bubbles rendered the test surface dry and/or partially wetted. Small heat flux increase of only 8 W/cm^2 was achieved in this regime for a wide cooling temperature difference range of 104-158 ^{o}C. At point D, thermal oscillation of the surface temperature of the test substrate due to single bubble growth and rupture was recorded. Figure 4.12 below shows snapshot images of single bubble growth and rupture in a spray cooling experiment. The working fluid was water. The cooling temperature difference at which the images were taken was in the range of 105-160 ^{o}C. The images were processed using Image J software.

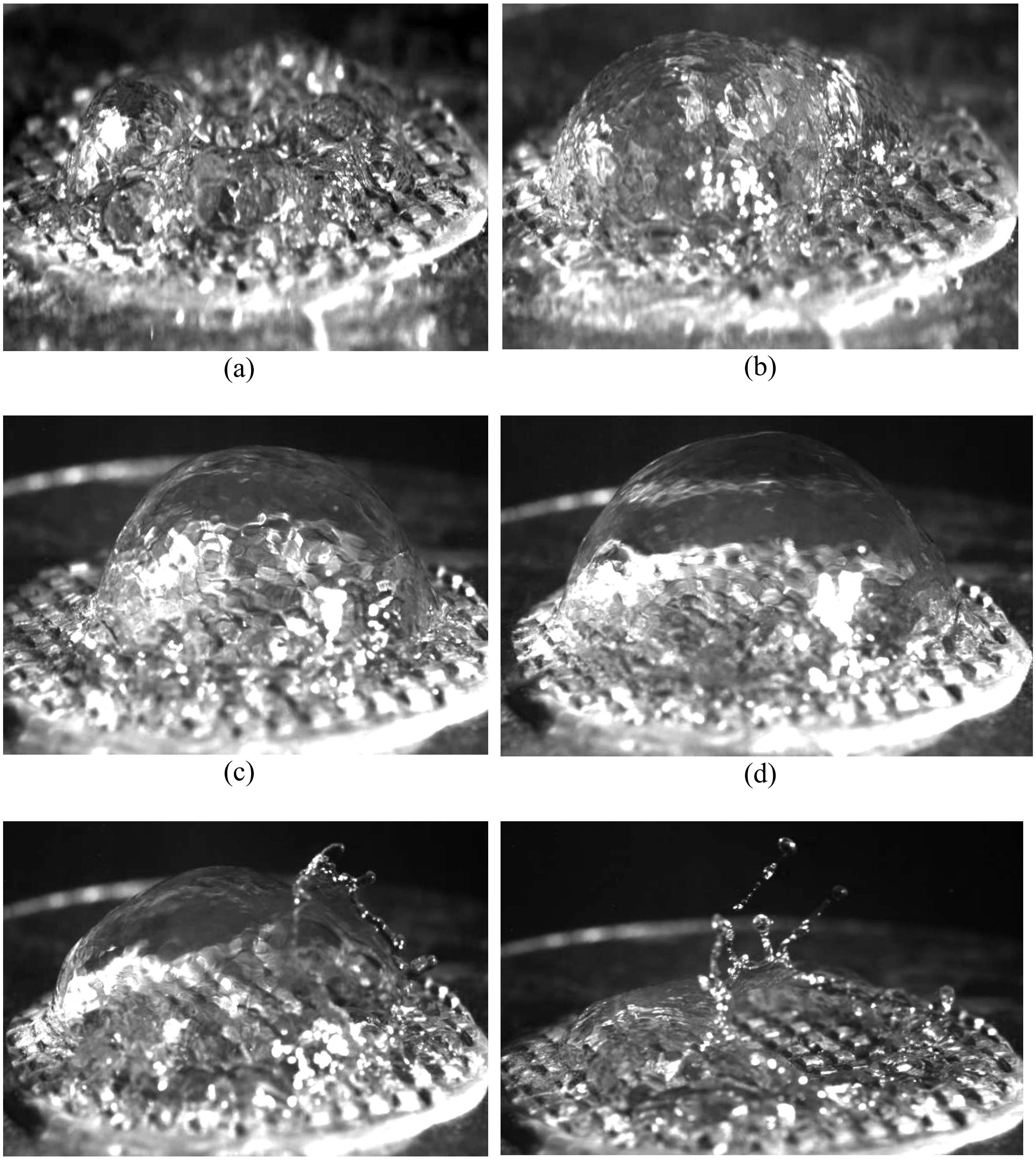

(a) (b)

(c) (d)

(e) (f)

Figure 4.12. Single bubble growth and rupture: (a) small bubble generation; (b) coalescence of small bubbles; (c) single bubble growth; (d) end of single bubble growth; (e) single bubble ruptures; (f) receding ruptured bubble

As shown in Figure 4.12 (a) to (d) the small bubbles which form on the surface of the test substrate coalesce into a single bubble. The single bubble grows and is filled with vapor at its core. The vapor inside the core of the single bubble expands as the substrate is continuously heated. When the vapor pressure inside the growing single bubble exceeds that of the environment, the bubble ruptures as it is shown in (e) to (f). High amount of energy is released upon bubble rupture. This is captured in a temperature drop of the surface of the test substrate. Figure 4.13 shows the temperature profile of the surface of the substrate during bubble growth and rupture as indicated previously by Figure 3.11.

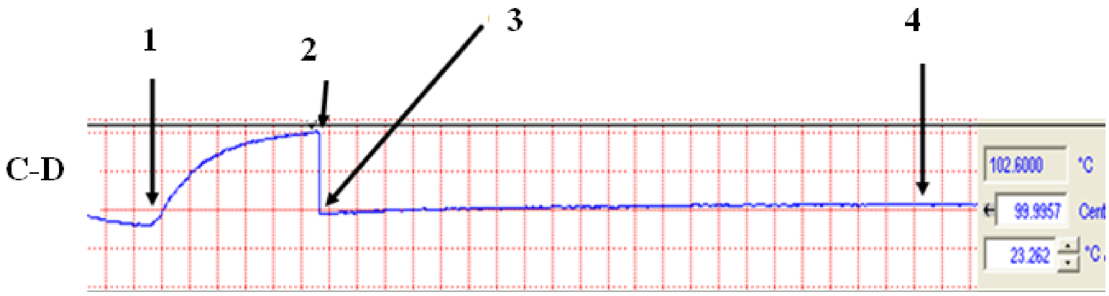

Figure 4.13. Temperature profile during bubble growth and rupture

As shown in Figure 4.13, point 1 is the onset of bubble growth. The surface temperature of the substrate increases during the bubble growth between point 1 and 2. The temperature increase during bubble growth (1 to 2) is exponential as shown in Figure 4.13. At point 2 when the bubble has reached its maximum size and the vapor pressure inside the single bubble exceeds that of the environment pressure, the bubble ruptures. Temperature drop up-to 23 ^{o}C has been recorded during bubble rupture as shown from point 2 to 3. When the bubble ruptures, new small bubbles begin to form. Small bubbles generation regime is shown beyond point 3.

At surface temperature of the substrate between 110-120 ^{o}C, the repeating or cyclic bubble growth and rupture is very rapid. Temperature rise and drops are measured during the bubble growth and rupture respectively. Figure 4.14 shows the temperature profile during rapid bubble growth and bubble rupture; and delayed bubble rupture.

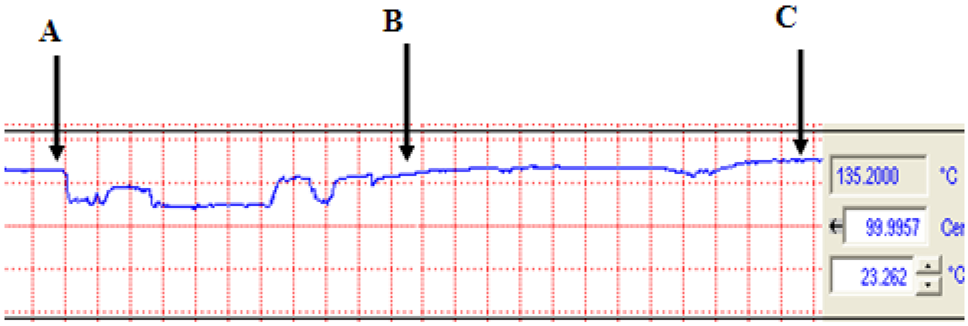

Figure 4.14. Temperature profile at rapid bubble growth and rupture

In Figure 4.14, point A to B shows the rapid bubble growth and bubble rupture. Temperature rise and drops were recorded at bubble growth and bubble rupture respectively. Beyond point B, there is delay in the bubble rupture. The surface temperature of the substrate increases unsteadily from point B to C when there is delay in bubble rupture. Pressure of the heater chamber increased unsteadily during the delayed bubble rupture regime. Figure 4.15 shows the pressure difference (ΔP) versus the surface temperature during the bubble growth and rupture phenomenon. The pressure difference (ΔP) is the difference in pressure between the heater chamber and the atmosphere.

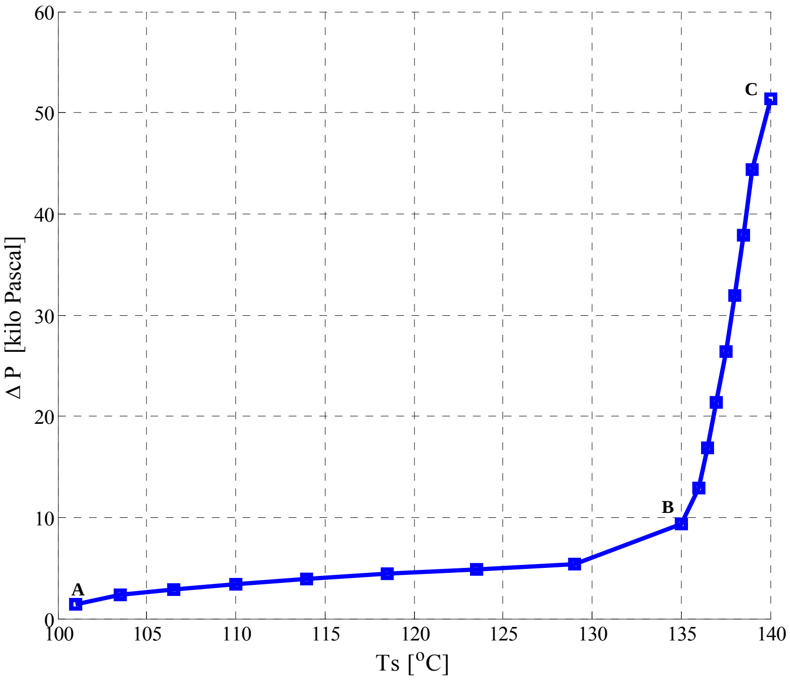

Figure 4.15. Pressure rise at bubble growth, rupture and delayed bubble rupture

In figure 4.15, point A to B indicates the rapid bubble growth and rupture period. There is small pressure increase about 8 kilo Pascal (kPa) over a temperature range (102-132 ^oC). Beyond point B, the pressure increases monotonically. Delayed bubble rupture is observed between point B and C. Pressure difference rise up-to 52 kPa is recorded. The unsteady pressure rise and delayed bubble rupture decreased the cooling effects in terms of heat flux as it is indicated in previous section in Figure 4.11.

Bubble generation increases heat transfer mechanism in spray cooling experiment, however, delay in the rupture of the bubbles mitigates the heat transfer process. The bubble size and growth depends on the amount of liquid fluid on the surface of the test substrate. The following section presents analytical results of liquid film thickness on heat flux in heat transfer applications.

4.4 Effects of Liquid Film Thickness on Heat Transfer Performance

The effect of liquid film thickness on heat transfer performance measured in terms of heat flux has been determined analytically. The thin liquid film evaporation approximation is used. In the present analysis, however, it is to be noted that the film thickness be not less than 0.25 mm. At liquid film thickness less that 0.25 mm, radiation heat transfer mode takes dominance and the approximation becomes invalid. Figure 4.16 shows the effect of liquid film thickness on the heat flux.

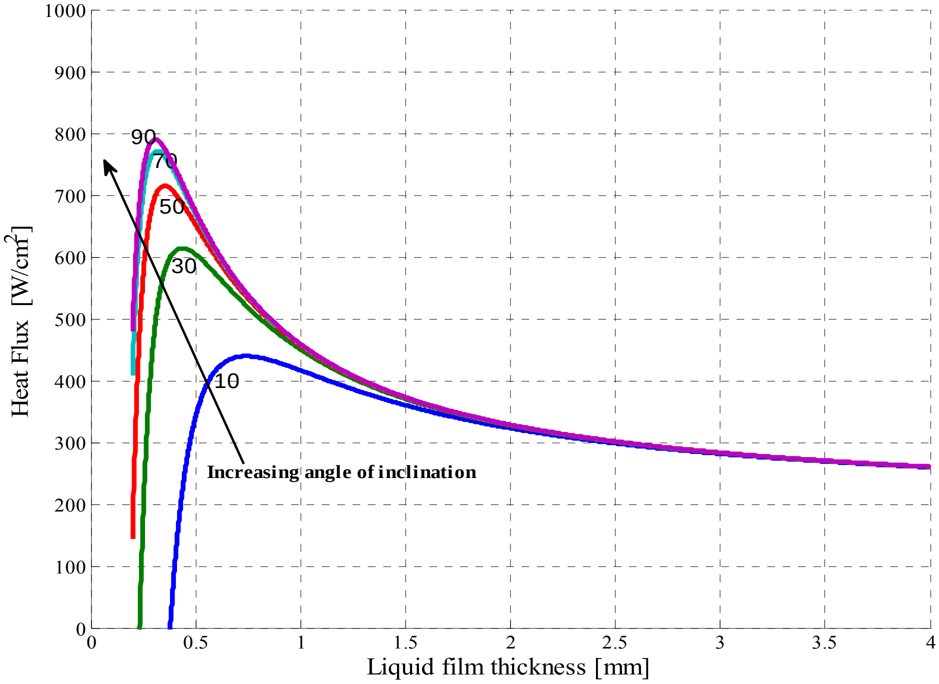

Figure 4.16. Heat flux versus liquid film thickness

Figure 4.16 shows that for all angles of inclination of the heated surfaces, the heat flux initially increases to a maximum with increasing liquid film thickness. When heat flux has reached maximum, increasing the liquid film thickness decreases the heat flux. The result shows that highest maximum heat flux is obtained for a vertically oriented flat plate with liquid film thickness of about 0.4 mm. The result also indicates that lower heat fluxes are obtained with decreasing angle of inclination. However, there is no effect of the liquid film thickness on heat flux for all angles of inclination at film thickness above 2 mm.

In addition, the result shows that for all angles of inclination, a critical film thickness is reached where maximum heat flux is obtained. With film thickness lower and/or higher than the critical film thickness, heat flux is mitigated. Thus for practical applications where maximum heat fluxes are to be obtained, an optimal film thickness be maintained on the heated surface.

The mean velocity of the flowing liquid film has also been determined and is presented as Figure 4.17. The result shows that the liquid film thickness increases with increasing mean velocity of the liquid for all angles of inclination. The result also shows that larger film thickness is associated with smaller angles of inclination of the test surface. Based on the film thickness versus heat flux result discussed above in Figure 4.16, for an inclined surface at an angle of inclination of 10^o, the critical film thickness is obtained at mean velocity of about 0.3 m/s. For vertical and other inclination angles above 10^o, maintaining mean velocity 0.3-0.5 m/s will ensure that optimal thin liquid film ensue on the heated surface to maximize the heat flux. The following section presents empirical correlations that have been derived for spray cooling heat transfer based on the data obtained in the present research work.

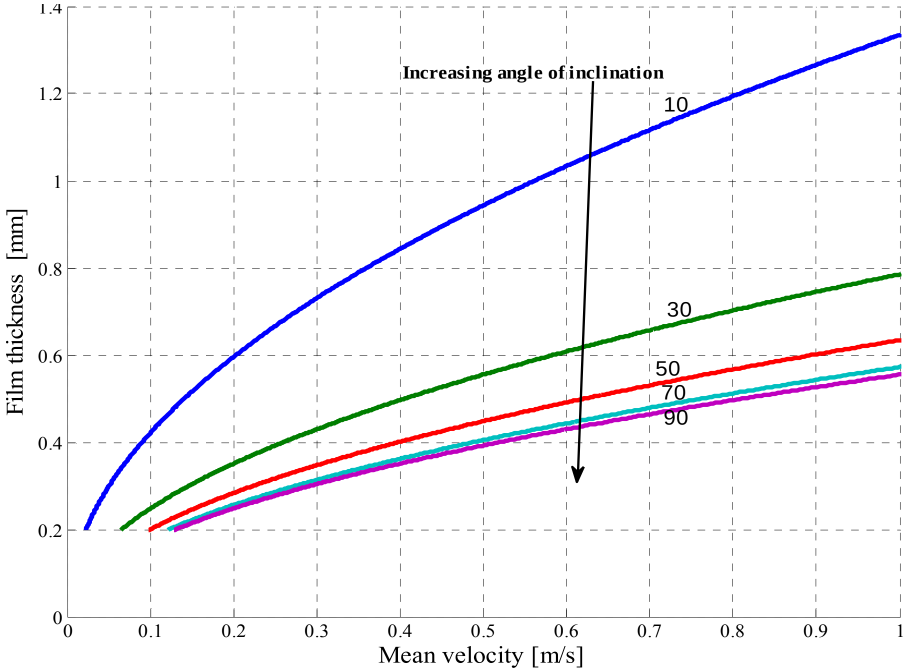

Figure 4.17. Mean velocity versus liquid film thickness

4.5 Empirical Correlations from Experimental Data

Empirical correlations have been developed from the present data for the various heat flux regimes in spray cooling experiments. Forced convection, active bubbles generation and bubble coalescence and single bubble rupture have been identified as the main heat flux regimes in spray cooling experiments. The various heat flux regimes and the heat transfer mechanisms associated with them have been presented in previous sections. The empirical correlations were developed by determining the best fit curve that describes the data in the heat flux regimes. Figure 4.18 below shows the heat flux regimes and the empirical correlations which have been determined with them.

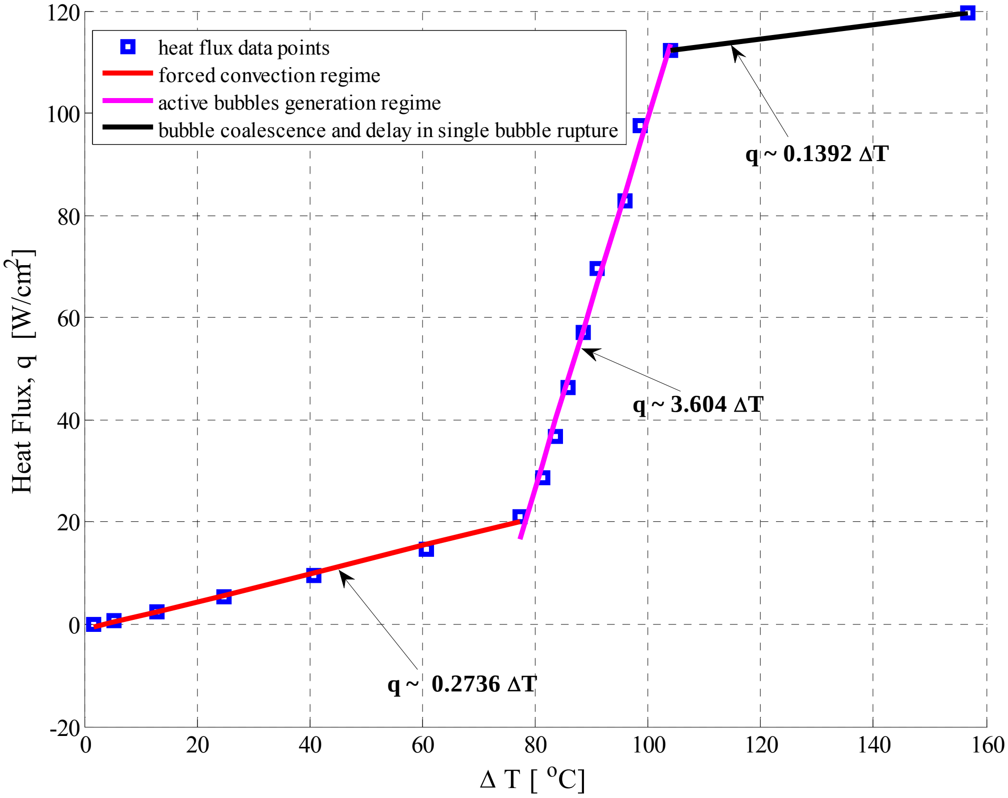

Figure 4.18. Empirical correlations for heat flux regimes is spray cooling

Figure 4.18 shows the empirical correlations in terms of heat flux (q) and the cooling temperature difference (ΔT) which have been obtained with water as the working fluid. The test substrate was ultra-conductive copper (Alloy 101) with smooth surface and area size of 11.40 cm^2. In all the heat flux regimes, the heat flux is significantly linear with the cooling temperature difference. Table 4.1 presents the correlation constants for heat flux versus cooling temperature difference for the various heat flux regimes that has been extracted from Figure 4.18.

Table 4.1. Correlation constants for heat flux regimes in spray cooling experiment

Heat Flux Regime	Correlation Constant
Forced Convection	0.2736
Active Bubble generation	3.6040
Bubble Coalescence and Single bubble rupture	0.1392

Table 4.1 indicates that the magnitude of the empirical correlation constant for the active bubble generation regime is in order of 10 times more than the forced convection and bubbles coalescence and single bubble rupture regimes. The correlation constant is analogous to heat transfer coefficient in cooling heat transfer. Therefore, based on the present data, the heat transfer performance measured in terms of heat transfer coefficient is ten times more in the active bubble generation regime than in the bubble coalescence and single bubble rupture regimes. For practical heat transfer applications where higher heat transfer coefficients are desired with spray cooling techniques, the active bubble generation regime is therefore of great importance.

The analysis has been extended to a modified surface and the result compared to that of smooth surface. In the experiments, water was used as the working fluid at flow rate of 1.26 grams per second. Figure 4.19 shows the empirical correlations which have been determined for the modified and smooth surfaces. The empirical correlation relates the heat flux (q) to the cooling temperature difference (ΔT). The test substrate was ultra-conductive copper material (Alloy 101) with surface area of 7.92 cm^2.

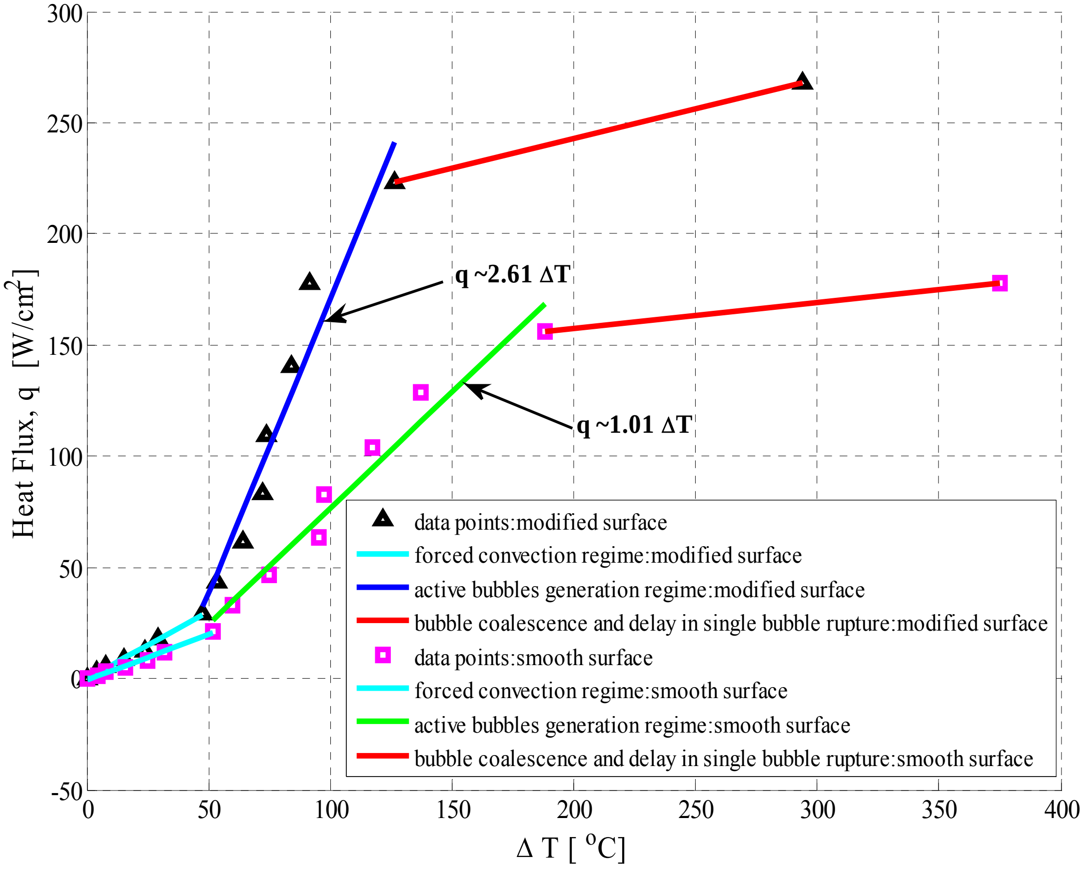

Figure 4.19. Empirical correlation for modified and smooth surfaces

Figure 4.19 shows the heat flux regimes and with specific emphasis on the empirical correlations for the modified and smooth surfaces in the active bubble generation regime. The modification of the test surface was in the form of grooves with size of 1270 µm by 1270 µm. The R-square values for the best fit lines for the modified and smooth surfaces are 0.942 and 0.951 respectively. The result shows that the empirical correlation constant for the modified surface is 2.6 times higher than the smooth surface in the active bubble generation regime. The correlation constant is analogous to heat transfer coefficient in cooling heat transfer. Modified surfaces can therefore be used to increase the heat transfer performance in spray cooling applications. Comprehensive conclusion and recommendations based on the experimental and analytical results obtained in the present research work are presented in Chapter 5.

CHAPTER 5

CONCLUSIONS AND RECOMMENDATIONS

In the present research work, cooling techniques have been developed to accomplish the specific objectives which were formulated based on the aforementioned knowledge gabs in spray cooling applications. Thermal management schemes for enhancing Heat Transfer Coefficient (HTC) and maximizing Critical Heat Flux (CHF) in spray cooling applications have been developed. The findings and conclusions of the research work are presented below.

1. The experimental results show that higher Critical Heat Fluxes (CHFs) are associated with smaller surface area sizes than larger area sizes. Critical heat fluxes of 254 W/cm^2, 170 W/cm^2 and 120 W/cm^2 were obtained for 5.07 cm^2, 7.92 cm^2 and 11.40 cm^2 surface area sizes respectively. However, it has been determined that the Incipience of Critical Heat Flux (ICFH) is independent of the test surface area size provided there is fluid coverage on the test surface. Proper fluid management is therefore crucial in spray cooling applications. In all experiments conducted, Incipience of Critical Heat Flux (ICHF) was determined to occur when the cooling temperature difference is 5-25^{o}C above the saturation temperature of the working fluid ($\Delta T = T_{sat} + (5\text{-}25)\ ^oC$).
2. Experiments were conducted on both modified and smooth surfaces to determine the effect of surface modifications on heat transfer performance. The heat transfer performance was measured in the form of Critical Heat Flux (CHF) and

Heat Transfer Coefficient. The results indicate that the modified surfaces enhance the Heat Transfer Coefficient and maximize the Critical Heat Flux over the smooth surfaces. The modified surface initiated a wicking phenomenon on the surface thereby enhancing the fluid spread and wettability on surface areas larger than the spray fluid impact area. In addition, wicking on the surface increased the convective heat transfer on the modified surface. Modification of the surface of the substrate is therefore of great practical use for large surfaces where higher convective heat transfer terms are desired. Heat Transfer Coefficient (HTC) enhancement of 8500 W/m^2-K has been achieved at colling temperature difference of about 100 ^{o}C for the modified surface over the smooth surface using water as the working fluid. Maximum heat flux gain of about 130% has also been obtained for the modified surface over the smooth surface at cooling temperature difference of about 90 ^{o}C.

3. The effect of liquid film thickness on Critical Heat Flux (CHF) has also been determined analytically. The result shows that an optimal liquid film thickness needs to be maintained on the test surface to maximize the heat flux. In addition, the result shows that higher heat fluxes are obtained for vertically oriented surfaces than inclined or horizontal surfaces for the same liquid film thickness and fluid upstream conditions. Maximum heat flux of 800 W/cm^2 was achieved for an optimal mean liquid film thickness of about 400 μm for a vertically oriented test surface. However, for liquid film thickness above 2000 μm, the results show that the heat flux is independent of the angle of inclination of the test surface.

4. A phenomenon has been observed at incipience of critical heat flux in spray cooling experiment akin to vapor film formation in nucleate pool boiling. Formation of single bubble covering the whole heated surface was observed. Thermal oscillation of the test substrate temperature was observed when there was delay in the rupture of the single bubble at incipience of critical heat flux. Increasing heater chamber vapor pressure was also observed
5. In addition, Novec 7000, a new working fluid, has been characterized as a prospect for cooling applications. Lower excess temperature differences were obtained when compared to water.
6. Empirical correlations were also developed for the various heat flux regimes. Empirical correlation constants akin to heat transfer coefficient have been determined. The result shows that the magnitude of the empirical correlation constant for the active bubble generation regime is in order of 10 times more than the forced convection and bubbles coalescence and single bubble rupture regimes. In addition, the result also indicates that the empirical correlation constant for a modified surface is 2.6 times higher than the smooth surface in the active bubble generation regime. The heat transfer performance of the modified surface is therefore higher than the smooth surface for the same operating and test conditions.

Based on the experiments conducted and the results obtained in the present research work, the following recommendations are suggested.

1. Fluid management has been identified to be very crucial in spray cooling thermal management schemes. Efficient cooling can be achieved when the test surface is completely covered with the working fluid. It is therefore recommended that in spray cooling applications, the system should be designed such that there is always a fluid coverage on the surface of the test substrate.
2. It has been determined that at the onset of critical heat flux in spray cooling, the system pressure increases sharply and becomes unsteady. This has been attributed to the increased vapor formation and expansion inside the heater chamber. It is therefore imperative that extra vapor by-pass installations be incorporated into spray cooling systems for safety precautions.

REFERENCES

Allen, S. J. (2003). Capillary-Driven Flow in Liquid Filaments Connecting Orthogonal Channels. *Computational Fuel Cell Dynamics Workshop, Banff International Research Station, Banff, Canada*.

Bhattacharya P, Samanta, A. N., & Chakraborty, S. (2009). Spray evaporative cooling to achieve ultra fast cooling in runout table. *International Journal of Thermal Sciences, 48*(9), 1741-1747.

Bostanci, H., Rini, D. P., Kizito, J. P., & Chow, L. C. (2009). Spray Cooling With Ammonia on Microstructured Surfaces: Performance Enhancement and Hysteresis Effect. *Journal of Heat Transfer-Transactions of the Asme, vol 131*(7-14).

Chen, J. C. (1966). A Correlation for Boiling Heat Transfer to Saturated Fluids in Convective Flow. *Ind.Eng.Chem: Process Des. Develop, 5*, 322-329.

Estes, K. A., & Mudawar, I. (1995). Correlation of Sauter Mean Diameter & Critical Heat Flux for Spray Cooling of small surfaces. *International Journal of Heat and Mass Transfer, 38(16)*, 2985-2996.

Gong S. J, Ma, W. M., & Dinh, T. N. (2010). Diagnostic techniques for the dynamics of a thin liquid film under forced flow and evaporating conditions. [Article]. *Microfluidics and Nanofluidics, 9*(6), 1077-1089.

Hall, D. D., & Mudawar, I. (1995). Experimental & Numerical Study of Quensching Complex-Shaped Metallic Alloys with Multiple, Overlapping Sprays. *International Journal of Heat and Mass Transfer, 38*, 1201-1216.

Horacek, B., Kiger, K., & Kim, J. (2005). Single Nozzle Spray Cooling Heat Transfer Mechanisms. *International Journal of Heat and Mass Transfer, 48(8)*, 1425-1438.

Kharangate, C. R., Mudawar, I., & Hasan, M. M. (2011). Experimental and theoretical study of critical heat flux in vertical upflow with inlet vapor void. *International Journal of Heat and Mass Transfer, 55*(1-3), 360-374.

Kim, J. (2007). Spray cooling heat transfer: The state of the art. *International Journal of Heat and Fluid Flow, 28*(4), 753-767.

Kizito, J. P., L, V. W. R., Gordon, B., & Tryggvason, G (2005). Spray Cooling Processes for Space Applications,. *National Center for Microgravity Research, NASA Glenn Research Center, 21000 Brookpark Rd,Cleveland, OH 44135*.

Kulenovic, R., Mertz, R., & Groll, M. (2002). High speed flow visualization of pool boiling from structured tubular heat transfer surfaces. *Experimental Thermal and Fluid Science, 25*(7), 547-555.

Lin, L., & Ponnappan, R. (2003). Heat transfer characteristics of spray cooling in a closed loop. *International Journal of Heat and Mass Transfer, 46*(20), 3737-3746.
Lin, L., Ponnappan, R., Yerkes, K., & Hager, B. (2004). Large area spray cooling. *In: Proceedings of the 42nd AIAA aerospace sciences meeting and exhibit, January 5-8, 1341*, 10838-10843.

Martinez-Galvan, E., Ramos J. C, & Anton R. (2011). Film Thickness and Heat Transfer Measurements in a Spray Cooling System With R134a. *Journal of Electronic Packaging, 133*(1) 98-106.

Mudawar, I., & Estes, K. A. (1996). Optimizing and predicting CHF in spray cooling of a square surface. *ASME Jounal Heat Transfer, 118*(672-9).

Pais, M., Chow, L., & Mahefkey, E (1992). Surface roughness and its effect on heat transfer mechanism of spray cooling. *ASME Jounal Heat Transfer, 114(1)*, 211-219.

Pais, M., Tilton, D., Chow, L., & Mahefkey, E. (1989). High heat flux, low superheat evaporative spray cooling. *Proceedings of the 27th AIAA Aerospace Sciences Meeting, Reno, NV, 100-107.*

Panão, M. R. O., & Moreira, A. L. N. (2009). Intermittent spray cooling: A new technology for controlling surface temperature. *International Journal of Heat and Fluid Flow, 30*(1), 117-130.

Pautsch, A. G., & Shedd, T. A. (2005). Spray impingement cooling with single- and multiple-nozzle arrays. Part I: Heat transfer data using FC-72. *International Journal of Heat and Mass Transfer, 48*(15), 3167-3175.

Pautsch, A. G., & Shedd, T. A. (2006). Adiabatic and diabatic measurements of the liquid film thickness during spray cooling with FC-72. *International Journal of Heat and Mass Transfer, 49*(15-16), 2610-2618.

Rini, D. P., Chen, R. H., & Chow, L. (2002). Bubble Behavior and Nucleate Boiling Heat Transfer in saturated FC-72 spray cooling. *ASME Jounal Heat Transfer, 124*, 63-72.

Rini, D. P., Chen, R. H., & Chow, L. C. (2002). Bubble Behavior and Nucleate Boiling Heat Transfer in saturated FC-72 Spray Cooling. *Journal of Heat Transfer, 124*, 63-72.

Rybicki, J. R., & Mudawar, I. (2006). Single-Phase and Two-Phase Cooling Charactersitcs of Upward-Facing and Downward-Facing Sprays. *International Journal of Heat and Mass Transfer, 49*, 5-16.

Schwartzkopf, J. D. (2005). A Numerical Study of Enhanced Flow Boiling Techniques for Multi-Phase Narrow Channel Flows using Liquid Atomization.

Schwartzkopf, J. D., Crowe, C. T., Dutta, P., & Li, B. Q. (2009). Atomized Non-Equilibrium Two-Phase Flow in Mesochannels: Momentum Analysis, *International Journal of Heat & Fluid Flow*, 30, 99-107.

Schwartzkopf, J. D., Sovar, G., Cader, T., Okamoto, K., Li, B. Q., & Ramaprian, B. (2004). Effect of spray angle in spray cooling thermal management of electronics. *ASME Heat Transfer/Fluids Engineering Summer Conference* (July 11-15), 20, 110-115.

Schwarzkopf, J. D., Crowe, C. T., Dutta, P., & Li, B. Q. (2009). Atomized non-equilibrium two-phase flow in mesochannels: Momentum analysis. *International Journal of Heat and Fluid Flow, 30*(1), 99-107.

Sehmbey, M., Chow, L. C., Pais, M., & Mahefkey, T. (1995). High Heat Flux Spray Cooling of Electronics. *In: 12th symposium om space nuclear power and propulsion, AIP conference proceedings, 324*(January 8-12, Albuquerque, NM), 903-909.

Selvam, R., Lin, L., & Ponnappan, R. (2006). Direct simulation of spray cooling: effect of vapor bubble growth and liquid droplet impact on heat transfer. *International Journal of Heat Mass Transfer, 49:4265–78.*

Selvam R. Paneer, Bhaskara, S., & Balda, J. C. (2005). Computer modeling of liquid droplet impact on heat transfer during spray cooling. *In: ASME summer heat transfer conference, HT2005-72569* (July 17-22).

Selvam R. Paneer, Lin, L., & Ponnappan, R. (2006). Direct simulation of spray cooling: Effect of vapor bubble growth and liquid droplet impact on heat transfer *International Journal of Heat and Mass Transfer, 49*, 4265-4278.

Selvam RP, Bhaskara S, Balda JC, Barlow F, & Elshabini, A. (2005). Computer modeling of liquid droplet impact on Heat transfer during spray cooling. *In: ASME summer heat transfer conference, July 17–22, San Francisco, CA;20,2-7.*

Selvam, R. P., Lin, L., & Ponnappan, R. (2005). Computational modeling of spray cooling: current status and future challenges. *In: Space technology and applications international forum (STAIF 2005), February 13–17, Albuquerque, NM;, 746. p. 56–63.*

Selvam, R. P., Sarkar, M., & Ponnappan, R. (2005). Modeling of spray cooling: Effect of droplet velocity and liquid to vapor density ratio on heat transfer. *In: TFAWS 2005: 16th Annual Thermal and Fluids Analysis Workshop*(August 8-12, Orlando, FL).

Selvam, R. P., Sarkar, M., & Ponnappan, R. (2006). Effect of thermal conductivity, latent heat of vaporization of liquid on heat transfer in spray cooling. *In: SAE2006 power systems conference, November 7-9, New Orleans, LA* (2006-01-3068).

Silk, A. E., Golliher, L. E., & Selvam, R. P. (2007). Spray Cooling Heat Transfer:Technology Overview & Assessment of Future Challenges for Microgravity Applications. *Thermal Managment Technology Group, NASA Goddard Space Flight Center*.

Silk, A. E., Kim, J., & Kiger, K. (2006). Enhanced surface spray cooling with embedded and compound extended surface structures. *10th Intersociety conference on thermal and thermomechanical phenomena in electronic systems, May 30- June 3, San Diego, CA, paper no. 927, 90-98.*

Silk, E. A., & Bracken, P. (2010). Spray Cooling Heat Flux Performance Using POCO HTC Foam. *Journal of Thermophysics and Heat Transfer, 24*(1), 157-164.

Silk, E. A., Golliher, E. L., & Paneer Selvam, R. (2008). Spray cooling heat transfer: Technology overview and assessment of future challenges for micro-gravity application. *Energy Conversion and Management, 49*(3), 453-468.

Sodtke, C., & Stephan, P. (2007). Spray cooling on micro structured surfaces. *International Journal of Heat and Mass Transfer, 50*(19-20), 4089-4097.

Stodke, C., & Stephan, P. (2005). Spray cooling heat transfer on microstrutured surfaces. *6th World Conference on Experimental Heat Transfer, Fluid Mechanics and Thermodynamics, Matsushima, Japan*, 26, 100-109

Toda, S. (1972). A study of mist cooling (1st report: investigation of mist cooling). *Trans Jpn Soc Mech Eng, 38:581–8.*

Toda, S. (1973). A study of mist cooling (2nd report: theory of mist cooling and its fundamental experiments). *Trans Jpn Soc Mech Eng, 39:2160–93.*

Visaria, M., & Mudawar, I. (2007). Application of Two-phase Spray Cooling for Thermal Managment of Electronic Devices. *International Journal of Heat and Mass Transfer, 51*(90-99)

Visaria, M., & Mudawar, I. (2008a). Effects of high subcooling on two-phase spray cooling and critical heat flux. *International Journal of Heat and Mass Transfer, 51*(21-22), 5269-5278.

Visaria, M., & Mudawar, I. (2008b). Theoretical and experimental study of the effects of spray inclination on two-phase spray cooling and critical heat flux. *International Journal of Heat and Mass Transfer, 51*(9-10), 2398-2410.

Wang, Y., Liu, M., Liu, D., Xu, K., & Chen, Y. (2010). Experimental study on the effects of spray inclination on water spray cooling performance in non-boiling regime. *Experimental Thermal and Fluid Science, 41(10-17).*

Yang J, Pais M, & Chow, L. (1993). Critical heat flux limits in secondary gas atomized liquid spray cooling. *Exp Heat Transfer, 6:55–67.*

Yang, J., Chow, L. C., & Pais, M. R. (1996). Nucleate Boiling Heat Transfer in Spray Cooling. *Journal of Heat Transfer, 118*, 668-671.

Yang, J., Pais, M., & Chow, L. (1993). Critical Heat Flux Limits in Secondary Gas Atomized Liquid Spray Cooling. *Exp Heat Transfer, 6*, 55-67.

Yen, T.-H., Shoji, M., Takemura, F., Suzuki, Y., & Kasagi, N. (2006). Visualization of convective boiling heat transfer in single microchannels with different shaped cross-sections. *International Journal of Heat and Mass Transfer, 49*(21-22), 3884-3894.

Zhang, F., Wu You Ting, & Geng Jiao. (2008). An investigation of falling liquid films on a vertical heated/cooled plate. *International Journal of Multiphase Flow, 34*(1), 13-28.